City Research Online

City, University of London Institutional Repository

This is the accepted version of the paper.

This version of the publication may differ from the final published version.

Permanent repository link: https://openaccess.city.ac.uk/id/eprint/25417/

Link to published version:

Numerical Modelling of In-Nozzle Flow Transient Effects and Fuel Atomization Characteristics of an Industrial Atomizer

**City
University of London**

MHPS

Thesis submitted for the requirement of fulfilment of the requirements for the Degree of Doctor of Philosophy

Yasir Hayat Nazeer

November, 2020

Mitsubishi Hitachi Power Systems Europe, Germany

New Products & Innovation

City University of London, UK

School of Aeronautical and Mechanical Engineering

I

Abstract

Internally mixing twin-fluid Y-jet atomizers are widely used in coal fired thermal power plants for start-up, oil-fired thermal power plants and industrial boilers. The present work is the first to numerically model the multiphase flow through twin-fluid Y-jet atomizer as function of the various operating conditions affecting it. Two different detailed studies have been carried out. In the first study, the flow through internally mixing Y-jet atomizers is numerically modeled using the compressible Navier-Stokes equations; Wall Modeled Large Eddy Simulations (WMLES) is used to resolve the turbulence with Large Eddy Simulations whereas the Prandtl Mixing Length Model is used for modeling the subgrid scale structures, which are affected by geometric and operational parameters. Moreover, the Volume-of-Fluid (VOF) method is used to capture the development and fragmentation of the liquid-gas interface within the Y-jet atomizer. The numerical results are compared with correlations available in open literature for the pressure drop; further results are presented for the multiphase flow regime maps available for vertical pipes. The results show that the mixing point pressure is strongly dependent on the mixing port diameter to airport diameter ratio; the mixing port length moderately affects the mixing point pressure while the angle between mixing and liquid ports is found not to have an appreciable effect. Moreover, it is found that the vertical pipe multiphase flow regime maps in the literature could be applied to the flow through the mixing port of the twin-fluid Y-jet atomizer. The main flow regimes found under the studied operational conditions are annular and wispy annular flow. In the second study, the atomization mechanism of the gas-liquid multiphase flow through internally mixing twin-fluid Y-jet atomizer has been studied by examining both the internal and external flow patterns. Super-heated steam and Light Fuel Oil (LFO) are used as working fluids. VOF-to-DPM transition mechanism is utilized along with dynamic solution-adaptive mesh refinement to predict the initial development and fragmentation of the gas-liquid interface through Volume-of-Fluid (VOF) formulations on a sufficiently fine mesh, while Discrete Phase Model (DPM) is used to predict the dispersed part of the spray on the coarser grid. Two operational parameters, namely gas-to-liquid mass flow rate ratio (GLR) and gas-to-liquid momentum ratio are compared; the latter is found to be an appropriate operational parameter to describe both the internal flow and atomization characteristics. It is confirmed that the variation in the flow patterns within the mixing-port of the atomizer coincides with the variation of the spatial distribution of the spray drops.

Acknowledgments

Research Highlights and Novelty

- The compressible Navier-Stokes equations are used for the first time to model the flow in internally mixing Twin-Fluid Y-Jet Atomizer. Hybrid RANS and LES technique i.e. WMLES (wall modeled large eddy simulations) is used to resolve the larger eddies with LES simulation and smaller eddies near the wall are modeled with Prandtl Length Model. VOF (volume of fluid) method is used to capture the development and fragmentation of the gas liquid-interface. The numerical results obtained are compared with empirical correlations of the pressure drop for twin-fluid Y-jet atomizer available in the open literature and are found in good agreement.

- Seven atomizers with different geometrical parameters are used for the study. A total of 11 simulations are run for each atomizer with different GLR (gas-to-liquid mass flow rate) ratios. A total of 77 simulations are run for the study. Working fluids are water and air. The results show that the mixing point pressure is strongly dependent on the mixing port diameter to airport diameter ratio, specifically for gas to liquid mass flow rate ratio (GLR) in the range $0.1 < GLR < 0.4$; the mixing port length moderately affects the mixing point pressure while the angle between mixing and liquid ports is found not to have an appreciable effect. Chocked conditions always occur at the exit of the gas-port, not downstream of this point. In mixing duct although the instantaneous Mach numbers could be higher than one, there is no evidence of flow choking in the mixing duct.

- It is found that the vertical pipe multiphase flow regime maps in the literature could be applied to the flow through the mixing port of the twin-fluid Y-jet atomizer. The main flow regimes found under the studied operational conditions are annular and wispy annular flow.

Furthermore,

- The atomization mechanism of the gas-liquid multiphase flow through internally mixing twin-fluid Y-jet atomizer has been studied by examining both the internal and external flow patterns. VOF-to-DPM transition mechanism is utilized along with dynamic solution-adaptive mesh refinement to predict the initial development and fragmentation of the gas-liquid interface through Volume-of-Fluid (VOF) formulations on a sufficiently fine mesh, while Discrete Phase Model (DPM) is used to predict the dispersed part of the spray on the coarser grid. The variation in the droplet Sauter Mean Diameter (SMD) distribution as the function of the liquid-to-gas

momentum ratio (φ) agrees well with the mean film thickness and drop size distribution reported previously in the open literature.

- It is confirmed that internally-mixing twin-fluid Y-jet atomizer exhibits poor performance with Heavy Fuel Oil (HFO) as a working fluid.

Table of Contents

List of Figures

Nomenclature

Acronyms

SMD	Sauter Mean Diameter
VOF	Volume of Fluid
WMLES	Wall Modeled Large Eddy Simulations
LES	Large Eddy Simulations
RANS	Reynolds-Averaged Navier-Stokes
GLR	Gas-to-Liquid Mass Flow Rate Ratio
SGS	Subgrid Scale
Eq.	Equation
Noz.	Nozzle
HPC	High Performance Computing
DPM	Discrete Phase Model
PUMA	Polyhedral Unstructured Mesh Adaption
MHPS	Mitsubishi Hitachi Power Systems

Subscripts

p	Phase p
q	Phase q
m	Mixing Point
M	Mixing Port
a	Air
g	Gas
l	Liquid
pz	Premix Zone
pr	Particle

r	relative
i, j, k	Direction Vector
1,2	Points Along the Length of Mixing-Port
max	Maximum
min	Minimum
mix	Mixture
w	Water
∞	Infinity
K	Turbulent Kinetic Energy
ω	Turbulence Frequency

Superscripts

T	Transpose
s	Sub-grid Scale

Symbols

α	Volume Fraction
ρ	Density, kg/m^3
V	Velocity, m/s
P	Pressure, Pa
μ	Viscosity, $kg/m.s$
g	Gravitational Acceleration, m/s^2
T_σ	Surface Tension Force, N
T	Temperature, K
k	Curvature, m^{-1}
σ	Surface Tension, N/m
E	Energy, J
K_{eff}	Effective Thermal Conductivity, $W/m.K$
Δ	Modified Length Scale, m

τ	Reynold Stress Tensor, N/m^2
ν_t	Eddy Viscosity, m^2/s
δ	Kronecker Delta
y^+	Dimensionless Wall Distance
Ω	Vorticity, s^{-1}
S	Strain Rate, s^{-1}
θ	Angle, °
l	Length, mm
d	Diameter, m
$\bar{\bar{\tau}}$	Viscous Stress Tensor, kg/ms^2
φ	Liquid-to-Gas Momentum Ratio
V_r	Relative Velocity, m/s
We	Weber Number
Pr	Prandtl Number
Z	Coordinate Along the Length of Mixing-Port
Y	Coordinate Axis
C	Heat Capacity, J/K
$\dot{m}$	Mass Flow Rate, kg/s
G	Mass Velocity, kg/m^2s
J	Superficial Velocity, m/s
Fr_{tp}	Two Phase Froude Number
Q	Volume Flow Rate, m^3
c	Speed of Sound, m/s
R	Radius, m
μ'_l	Ratio of Liquid Viscosity to Water Viscosity at Standard Conditions
ρ'_l	Ratio of Liquid Density to Water Density at Standard Conditions
σ'_l	Ratio of Liquid Surface Tension to Water Surface Tension at Standard Conditions
A	Parameter Defined in Eq. 5.2
C_w	Empirical Constant
h_{max}	Maximum Edge Length, m
h_{wn}	Grid Step in Wall Normal Direction, m

d_w	Distance from Wall, m
C_{smag}	Smagorinsky Constant
a_1	Constant defined in Eq. 4.24
a_2	Constant defined in Eq. 4.24
a_3	Constant defined in Eq. 4.24
C_D	Drag Coefficient
F_D	Drag Force Per Unit Mass, N/kg
Ar	Surface Area, m^2
h	Convective Heat Transfer Coefficient, W/Km^2
t	Time, s
K	Turbulent Kinetic Energy, m^2/s^2
ω	Turbulence Frequency, s^{-1}
G_K	Generation of Turbulent Kinetic Energy, kg/ms^3
G_ω	Generation of ω, kg/m^3s^2
Y_K	Dissipation of K, kg/ms^3
Y_ω	Dissipation of ω, kg/m^3s^2
f_{β^*}	Function Defined in Eq. 4.43
X_K	Variable Defined in Eq. 4.44
β^*	Variable Defined in Eq. 4.45
$F(M_t)$	Compressibility Function Defined in Eq. 4.46
M_t	Variable Defined in Eq. 4.47
a	Variable Defined in Eq. 4.48

Chapter 1: Introduction

1.1 Motivation

With a rapidly developing world and improving living standards, the demand for energy is increasing at a very fast pace. Cost-effective and secure transition to a lower Carbon society demands a fundamental transformation of the power systems (European-Comission, 2019a). The European Commission's Energy Union Strategy has recently proposed for the more ambitious targets for the energy transition in EU by 2030 (European-Comission, 2019b) and has set an ultimate goal of prosperous climate neutral economy by 2050 (European-Comission, 2018). In this scenario, increased share of renewable energies, synthetic fuels and flexibility of the power plants has to play a crucial role in the security of electricity in the transition period.

According to an estimate, there are one hundred forty-three thousand Medium Combustion Plants (MCP) in the whole of the European Union. Most of these are either thermal power plants or chemical plants. Many of these plants rely on liquid fuel combustion. Large combustion power plants are coal-fired power plants, where liquid fuel combustion is used during the startup only. Since the European Energy policy supports energy mix with a higher share of renewable energy, the cyclic operation of large combustion power plants is inevitable; with more increasing startups and shutdowns. Thus, the operation of auxiliary burners with oil firing becomes of increased importance. And also, the introduction of synthetic liquid fuels through Power-to-X technologies, such as Dimethyl Ether (Mahdi & Christian, 2017) and (Chehade, et al., 2020), predicts the increased combustion of liquid fuels in industrial plants. Furthermore, recently revamped European legislation (Large Combustion Plant and Medium Combustion Plant Directives) imposes stricter emission limits for industrial burners. All these aforementioned conditions set new challenges on the design and operation of the oil burners. Hence it

is of immense importance to study the industrial boiler's atomizer and predict its atomization characteristics to mitigate the emissions and comply by the increasing stringent EU's emission limits.
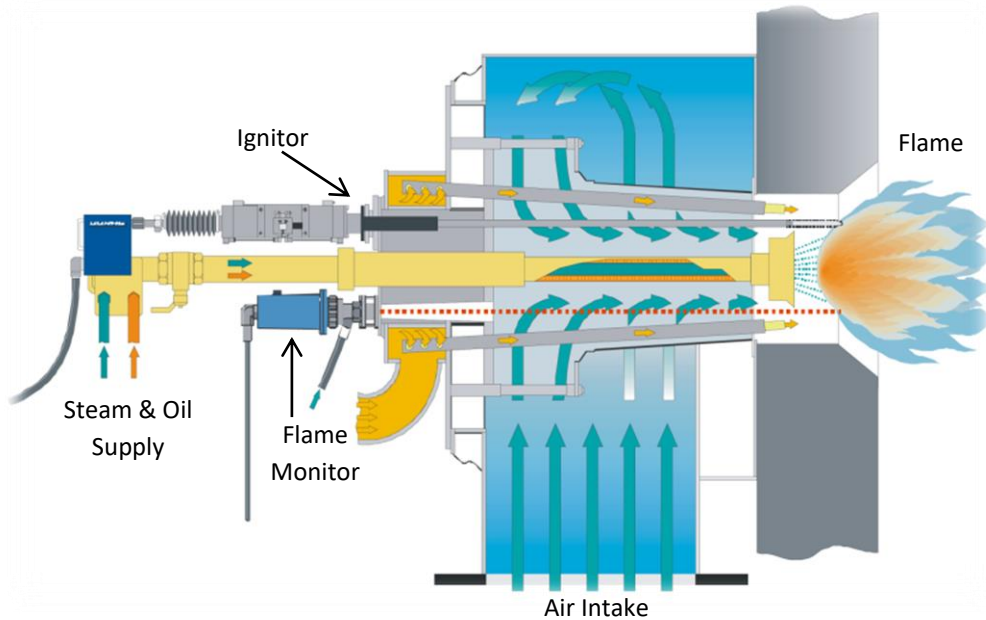
Figure 1.1 Schematic of industrial oil burner (courtesy MHPS)**.**

1.2 Industrial Relevance and Atomization

The transformation of the bulk liquid into sprays and other physical dispersions of small particles in the gaseous atmosphere are of importance in several industrial processes. These include combustion (spray combustion in industrial boilers, diesel engines, furnaces, gas turbines and rockets); process industries (spray drying, powdered metallurgy, evaporative cooling and spray painting); agriculture (crop spraying); and many other applications in medicine. Various devices to generate spray flows have been developed, and they are generally designated as nozzles or atomizers. Albeit atomization does not usually imply that the liquid particles are reduced to atomic sizes, the spray drops from atomization can be very small. In all aforementioned industrial applications, atomization and spray process is an integral part of a much larger practical flow system. For example in liquid fired industrial boilers, the heat produced during the combustion process in the combustor is transferred through radiation, conduction and convection by hot circulating gases, which has upstream compressors, pumps and fans while downstream a complex array of heat exchangers. Combustion provides energy to the system in the form of heat. An industrial

boiler combustor is a complex device within which there is a broad range of coupled, interacting physical and chemical phenomena, with atomization and spray being one of the most important processes. In the combustor, energy is added to the gas stream through combustion between the air and the liquid fuel, which is atomized first, forming a spray, before the gas-phase combustion occurs. Spray characteristics are of great importance to industrial boiler combustors. The liquid fuel, used as the energy source, must be atomized into smaller droplets in order to increase the surface area of fuel exposed to the hot gases and to facilitate rapid evaporation and mixing with the oxidant ambience, where the mixing always dominates the combustion process.

Atomization and spray process is a typical gas-liquid two-phase flow of great practical relevance in applications such as the fuel injection in industrial boiler combustors, gas-turbine combustors of aircraft engines and in internal combustion engines. The combustion performance and emissions are mainly affected by the atomization of the liquid fuel, the motion and evaporation of the fuel droplets and mixing of fuel with air. The dynamics of spray and its combustion characteristics are extremely important in determining, for instance, the flame stability behavior at widely varying loads, the safe and efficient utilization of energy, as well as the mechanisms of pollutants formation and destruction (Rink & Lefebvre, 1986). Understanding and controlling atomization and spray combustion is becoming an essential part of the industrial applications, which have been driven by increasingly urgent demands to improve fuel and energy efficiencies, and to drastically reduce the emission of the pollutants.

Generally speaking, liquid fuel emanates through the nozzle into the combustion chamber and is atomized to form a spray of droplets before gas-phase combustion takes place in vaporized fuel. Figure 2 depicts the simplified schematic of the liquid spray plume structure. In primary atomization region, the liquid dominates the flow and the liquid fuel blobs disintegrate into droplets and ligaments. The secondary atomization region has lower but still significant liquid volume fraction and includes further disintegration of the ligaments and droplets as well as droplet-droplet interaction, such as collisions and coalescence. In dilute spray region, spherical droplets are well formed and have a strong interaction with the turbulent airflow. In general, the spray characteristics depend upon the type of the atomizer, fuel injection pressure, fuel viscosity and fuel density. In case of twin-fluid atomizers, spray characteristics also depends on the pressure and properties of the auxiliary gas.

3
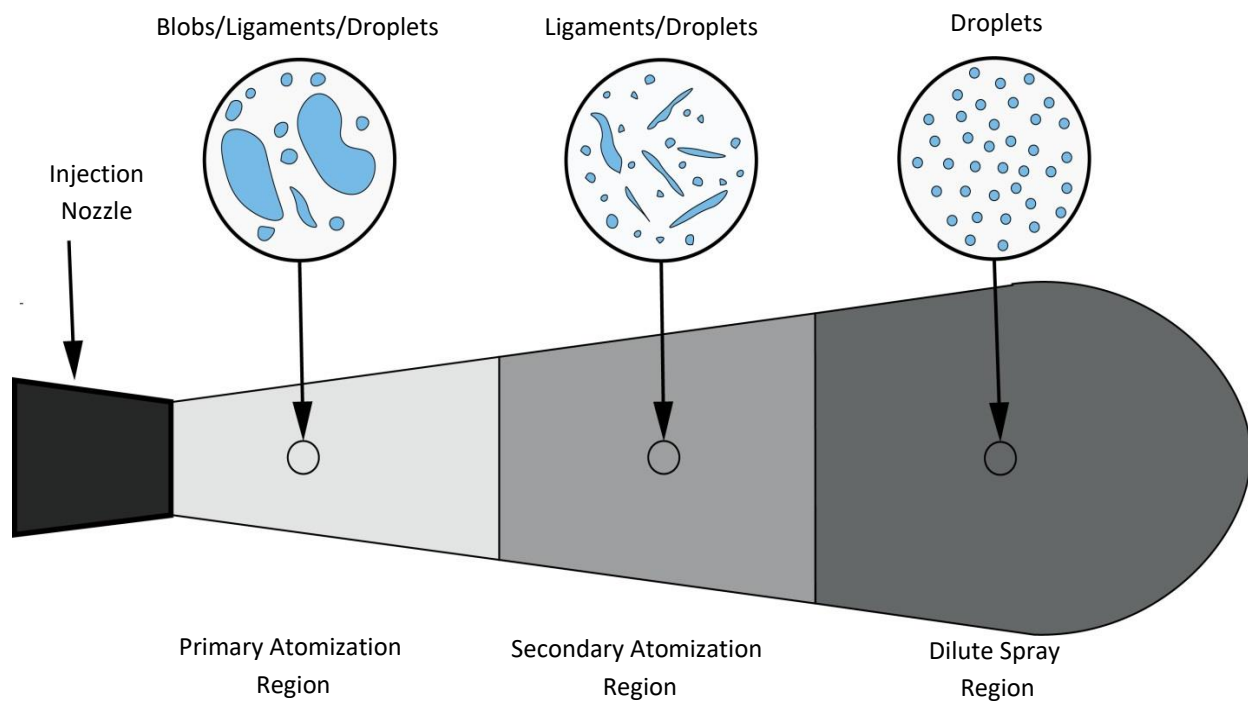
Figure 1.2 A schematic of a liquid spray.

1.3 Why CFD?

The rapid and steady advancements in the speed of computers and available memory storage size since the 1950s has led to the advent of computational fluid dynamics (CFD) in 1960s and the development of the advanced CFD approaches such as large-eddy simulations (LES) and direct numerical simulations (DNS) in a later stage. Modern CFD is a useful tool to obtain the flow characteristics that could be effectively utilized to comprehend physics of the flow, to interpret the available experimental data and to guide the experimental work, as well as to execute the preliminary calculations for altered operating conditions.

In CFD, the physical aspects of any fluid flow are governed by three fundamental principles: conservation of mass, conservation of energy and Newton's second law. These fundamental principles are represented by mathematical equations, which in general form can be expressed by partial differential equations, namely the Navier-Stokes equations. CFD determines the numerical solution to these equations of fluid flow, whilst iterating to obtain the solution through space and/or time to acquire a numerical description of the complete flow field of interest.

CFD supplements experimental and theoretical fluid dynamics by providing an alternative cost-effective means of simulating real flows, including gas-liquid multiphase flow such as atomization and spray phenomena. Furthermore, it also provides the means of testing the theoretical advancements for the conditions unavailable or very difficult to capture in experiments, hence providing further insight into the complex processes such as atomization and sprays. The role of CFD in engineering has become so prominent that now it is considered as the third dimension of fluid dynamics, the other two being the experimental and theoretical fluid dynamics (Anderson, 1995).

As an emerged science, CFD is well integrated into the industry for engineering, design, research and development purposes. Today traditional Reynolds-averaged Navier-Stokes (RANS) modeling of CFD framework is predominantly followed in the industry, where the time- or assemble-averaged equations for fluid mechanics are solved. Due to the averaging, the RANS approach does not provide enough insight into the dynamic and unsteady feature of the flow. For the atomization and spray processes, the unsteadiness is the dominant feature of the fluid dynamics, which can be often poorly predicted by RANS. The advanced modeling and simulation techniques like Large Eddy Simulations (LES) and Direct Numerical Simulations (DNS) can provide insight into such complex unsteady dynamics of the flow. DNS and LES simulation techniques are too expensive in terms of computational time and resources to be implemented in the industries. However, hybrid LES techniques such as Wall Modeled Large Eddy Simulations (WMLES), is beginning to emerge as a viable alternative to time-averaged or ensemble-averaged Navier-Stokes (RANS) turbulence modeling in industrial flows; it is able to capture flow structures larger than the grid size, while smaller scales are modeled with subgrid-scale models (SGS).

Chapter 2: Twin-Fluid Atomizers

2.1 Introduction

Atomizers are used in industry in order to produce sprays consisting of fine droplets. Fundamentally, the high relative velocity between the liquid to be atomized and the surrounding air or gas is required to atomize the injected liquid. Some atomizers achieve this by emanating the liquid at high velocity through the orifice into a relatively slow-moving stream of air. Noteworthy examples include different kinds of pressure atomizers (Elkotb, 1982) (Adler & Lyn, 1969) and also rotary atomizers (Hinze & Milborn, 1950) (Willauer, et al., 2006), which eject the liquid at high velocity from the periphery of rotating disk or cup. Others need atomizing medium such as air or steam to augment the atomization process and produce the sprays. These types of atomizers are referred to as twin-fluid atomizers. Figure 2.1 shows various types of twin-fluid atomizers. Based on the velocity of auxiliary gas, twin-fluid atomizers could be further classified into air-assist, air-blast and effervescent atomizers.

Twin-fluid atomizers have been used in numerous industrial applications over the years such as gas turbines (Lefebvre, 1988), internal combustion engines (Wade, et al., 1999), spray drying (Mujumdar, et al., 2010), spray coating (Esfarjani & Dolatabadi, 2009), scramjet engines (Gadgil & Raghunandan, 2011), fire suppression (Huang, et al., 2011), process industries (Loebker & Empie, 1997) and power plants (Zhou, et al., 2010). They have been studied extensively over the years. Most of the studies are focused on prefilming air-blast atomizers or effervescent atomizers due to their extensive commercial use. The earlier are used extensively in aircraft, marine and industrial gas turbines and the latter are used in various applications where low injection pressures and low gas flow rates are available. There exist considerable studies on internally mixing twin-fluid air-assist Y-jet atomizers. However, the understanding of such a nozzle is not very clear owing to complex aerodynamic and fluid dynamic flow pattern due to the mixing of gas and liquid within the mixing chamber.

In this chapter twin-fluid atomizers, namely air-assist, airblast and effervescent atomizers, are discussed briefly, while internally-mixing Y-jet atomizer, which is a type of air-assist atomizer, is a subject of investigation in this thesis, is discussed in detail.
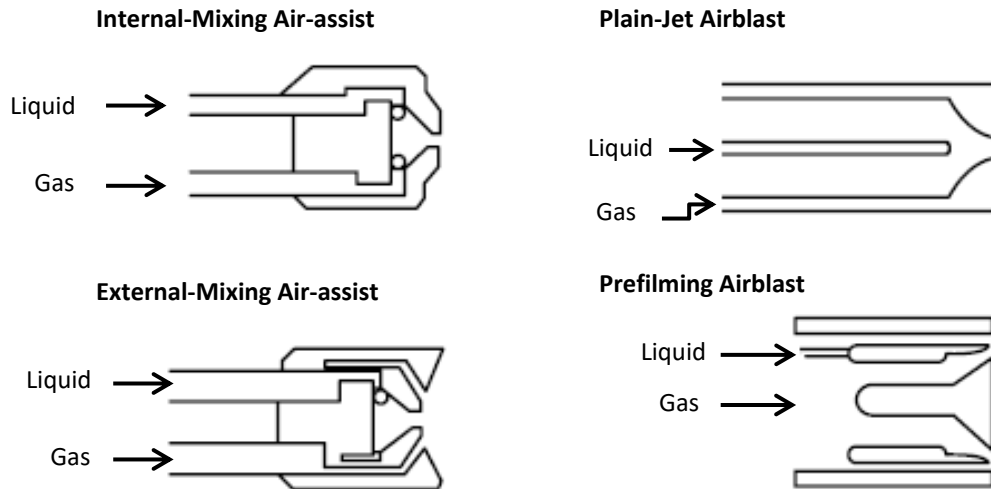
Figure 2.1 Various types of twin fluid atomizers (adopted from (Lefebvre & McDonell, 2017).

2.2 Atomizer Requirements

Following characteristics must be possessed by an ideal atomizer:

- Good atomization over a wide range of liquid flow rates.
- Rapid response to the variation in liquid mass flow rate.
- No flow instabilities.
- Lower power requirement.
- Design flexibility, capable of scaling.
- Low cost, light weight; ease of maintenance and servicing.

In addition to the above mentioned features, continuous flow fuel nozzles must possess the following features also:

- Even circumferential and radial fuel distribution.
- Less prone to gum formation by heat soakage.
- Low susceptibility to carbon deposition on the nozzle face and blockage by contaminants.

2.3 Air-assist Atomizers

Air-assist atomizers employ high-velocity steam or air to impinge on the liquid jet to augment the atomization process. Gas and liquid could be brought into contact either within the nozzle or outside of it, the earlier is termed as internally mixing twin-fluid air-assist atomizer, and the latter is termed as externally mixing twin-fluid air-assist atomizer. In externally mixing atomizers, high-velocity gas or steam impinges on the liquid just outside the discharge orifice, while in internally-mixing ones, the gas or steam mixes with the liquid inside the nozzle before being injected. In the internal mixing type, the spray cone angle is minimum for maximum gas flow while the spray widens as gas flow reduces. This type of atomizer is well suited for high viscous liquids as good atomization could be obtained at low liquid flow rates (Barreras, et al., 2008). It is far more efficient than the externally mixing concept as lower gas flow rates are needed to achieve the same degree of atomization (Tanasawa, et al., 1978). However, external mixing atomizers have the advantage of producing sprays with constant spray angle at all liquid flow rates independently of the backpressure, as there is no communication between the flowing media internally.

Twin-fluid air-assist atomizers can generate small droplets even when operating at low liquid mass flow rates. They are available in various designs. Some employ pressure principle, where liquid fuel is supplied from pressurized source; others use the gravity principle, where gravity is used to supply the liquid to the atomizer. Siphon principle is also utilized in some of the atomizers, where the liquid source is self-aspirating. These atomizers can produce different spray patterns, including full cone, flat fan and hollow cone sprays. Spray angles typically range between 20° and 60°. The liquid distribution of the spray in full cone pattern tends to be uneven whereas flat fan sprays are available in both even and uneven patterns.

2.3.1 Internally-Mixing Twin-Fluid Y-Jet Atomizer

Undoubtedly, there are various ways to generate the atomized sprays using various types of nozzles, including for example rotary cups (Nguyen & Rhodes, 1998), twin-fluids (Lefebvre, 1988), (Wade, et al., 1999), and (Zhou, et al., 2010), pressure swirl (Radclife, 1955), and (Arcoumanis & Gavaises, 1999), fan (Dombrowski, et al., 1960), ultrasonic (Lang, 1962), electrostatic (Maski & Durairaj, 2010), diesel

injectors (Arcoumanis, et al., 1999) and (Mitroglou & Gavaises, 2011) and effervescent atomizers (Sovani, et al., 2001) and (Saleh, et al., 2018); solid or hollow cone sprays may form depending on the type of atomizer and operating conditions. However, in thermal power plants or oil-fired large industrial boilers, operating with high flow rates of viscous fuel, mostly Y-jet or internal mixing chamber twin-fluid atomizers are used (Barreras, et al., 2006). The former is used with light and medium fuel oil while the latter is used with heavy fuel oil (Li, et al., 2012), with steam as auxiliary fluid. An obvious advantage of using the steam is that any heat transfer from the steam to the fuel in the mixing port will enhance atomization by reducing the fuel's viscosity and surface tension. In contrast, the comparative test carried by (Bryce, et al., 1978) showed that compressed air produced much finer spray than steam. (Barreras, et al., 2006) demonstrated that for the same liquid mass flow rate, the internal mixing chamber twin-fluid atomizer requires a lower atomizing fluid mass flow rate than an equivalent Y-jet one, simultaneously yielding droplets with smaller Sauter Mean Diameter. The characteristic of the Y-jet atomizer is that liquid and gas (steam or air) is mixed before injected out. It generally consists of a number of jets from a minimum of 2 to a maximum of 20 (see Figure 2.2), arranged in an annular manner to provide hollow conical spray. The advantage of such an atomizer is that it could be operated by keeping constant gas-to-liquid mass flow rate ratio; and the requirement of the atomizing fluid is low. Y-jet atomizers are reported to maintain moderate emission rate while attaining relatively high atomization efficiency (Pacifico & Yanagihara, 2014). This kind of atomizers create high relative velocity by injecting gas at high velocity, which induces disturbances in the liquid jet and leads to the creation of smaller liquid ligaments; subsequently, smaller droplets are formed due to ligament's breakup due to aerodynamically-induced surface waves (Dombrowski & Johns, 1963). The high relative velocity of the gas helps the dispersion of the liquid and prevents droplets coalescence (Pacifico & Yanagihara, 2014).

A drawback of internally-mixing Y-jet atomizer when operating particularly with heavy fuel oil or crude oil is that in order to produce fine sprays, relatively larger steam mass flow rate at high velocity is needed. The intense interaction with turbulence field produces higher strain rates in the flame front that may lead to local flame extension and also possibly the flame elongation that usually ends in the contact with boiler walls. As a consequence, the reaction zone is cooled down, and hence, also contributes to the flame extinction. Moreover, the large amount of steam introduced into the reaction zone lowers the flame temperature, preventing the reignition of the mixture. These phenomena are particularly prominent in rich or lean mixture zones where temperatures are relatively lower. In these cases, reaction times become longer than the mixing time; consequently, polycyclic aromatic

hydrocarbon (PAH) are produced that lead to soot formation. Albeit, the reduced flame temperature can decrease thermal nitric oxides formation, however, heavy fuel oil and crude oil contains large Sulfur, Sodium and Vanadium contents, that may lead to the formation of alkali sulfates and vanadium salts that cause high-temperature corrosion, and sulfuric acid that can corrode the boiler low-temperature heat-transfer surfaces.
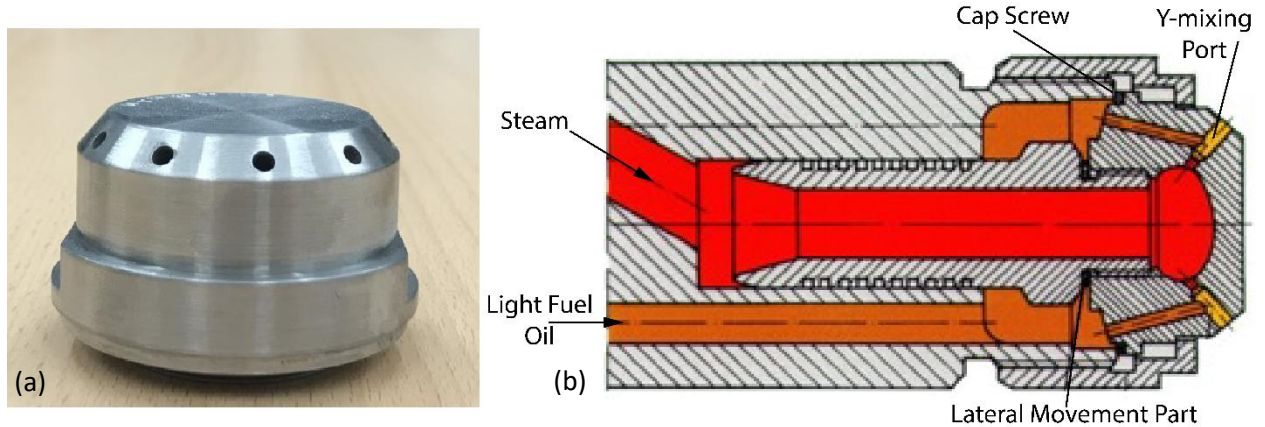
Figure 2.2 (a) nozzle head of twin-fluid Y-jet atomizer (b) Schematic of internally mixing twin-fluid Y-jet atomizer (courtesy MHPS).

Mullinger and Chigier (Mullinger & Chigier, 1974) were the first to study the performance of internally-mixing Y-jet atomizer systematically. Figure 2.3 depicts the atomization in a Y-jet atomizer proposed by Mullinger and Chigier. According to them, and as shown pictorially by Song & Lee (Song & Lee, 1996), some atomization occurs within the mixing chamber, but most of the liquid emanates from the atomizer in the form of liquid that is then shattered into droplets by the atomizing fluid. Song & Lee (Song & Lee, 1996) compared two dimensionless parameters namely gas to liquid mass flow rate ratio (GLR)

$$\text{GLR} = \frac{\dot{m}_g}{\dot{m}_l}$$

(2.1)

and liquid-to-gas momentum ratio (φ)

$$\varphi = \frac{G_l^2 d_l^2 \rho_{a,m} Sin\theta}{G_{g,m}^2 d_m^2 \rho_w}$$

(2.2)

Where G_l is the liquid mass velocity, $G_{g,m}$ is the gas mass velocity based on mixing port cross-sectional area, $\rho_{a,m}$ is the gas density at the mixing point.

They concluded that liquid-to-gas momentum ratio is a better parameter to describe the internal flow and spray characteristics as compared to GLR ratio. (Mullinger & Chigier, 1974) and (Prasad, 1982) reported an extensive parametric study and proposed design criteria for the twin-fluid Y-jet nozzles. In fact, the results of Mullinger and Chigier showed good agreement with the empirical dimensionless correlation of mass median diameter for air-blast atomizer proposed by Wigg (Wigg, 1959). It is pertinent to mention here that the choice to name an atomizer as air-assist or airblast atomizer is arbitrary. Usually, air-assist atomizers employ very high velocities that usually necessitate an external supply of high pressure steam/air, while the lower gas requirement of air-blast atomizers can usually be met by utilizing the pressure differential across the combustion liner.

Andressui et al (Andreussi, et al., 1992) reported that the length to diameter ratio of the mixing port influences the pressure drop, spray structure and droplet size distribution based on a semi-empirical model of the flow inside twin-fluid Y-jet atomizer. Song and Lee (Song & Lee, 1994) studied the effect of the mixing port length and the injection pressure on the flowrates of the gas and liquid and droplet size distribution. Andreussi et al (Andreussi, et al., 1994) explained the internal flow conditions and the liquid film thickness inside the mixing duct and postulated their effect on external spray characteristics. Song and Lee (Song & Lee, 1996) made a pictorial study of the internal flow pattern of Y-jet atomizer and described the internal flow as annular/annular mist flow (Chin & Lefebvre, 1993); they proposed the main mechanism involved in fuel atomization and linked the internal flow pattern to the droplet size distribution in the spray. Mlkvik et al (Mlkvik, et al., 2015) compared the performance of four different internally mixing twin-fluid atomizers for the range of different operating conditions and liquid properties. They found that the internally mixing Y-jet atomizer to produce most stable spray regardless of pressure differential and gas to liquid ratio (GLR). The internal flow pattern for the Y-jet atomizer showed strong agreement with the results of Song & Lee (Song & Lee, 1996) and Nazeer et al. (Nazeer, et al., 2018).

The effect of geometric and operational parameters on the pressure distribution in the internally-mixing Y-jet atomizers was studied experimentally by Pacifico and Yanagihara (Pacifico & Yanagihara, 2014). They used water and air at atmospheric conditions as working fluid, and proposed the empirical correlations for the pressure distribution in the mixing-duct of Y-jet atomizers. Following are the correlations for the pressure drop proposed by them based on gas-to-liquid mass flowrate ratio:

$$\frac{P_m}{P_a} = 0.169 + 0.81 exp\left[-0.675\theta^{-0.22}\left(\frac{l_m}{d_m}\right)^{-0.38}\left(\frac{d_m}{d_g}\right)^{4} GLR^{0.87}\right] \quad (2.3)$$

$$\frac{P_w}{P_a} = 0.161 + 1.06 exp\left[-1.08\theta^{-0.11}\left(\frac{l_m}{d_m}\right)^{-0.25}\left(\frac{d_m}{d_g}\right)^{3} GLR^{0.82}\right] \quad (2.4)$$

Here P_m is the mixing point pressure, P_a is the air inlet pressure, P_w is the water inlet pressure, l_m is the mixing port length, d_m is the mixing port diameter and d_g is the gas port diameter. These correlations, shown in Equations 2.3 and 2.4, are valid for the range $0 \leq GLR \leq 1$; $3.5 \leq l_m/d_m \leq 10$; $1.67 \leq d_m/d_g \leq 2$; and $45° < \theta < 70°$. In these correlations, θ must be in radians ($\pi/4 < \theta < 7\pi/18$).

Following is the correlation proposed by them for the pressure drop along the length of the mixing duct based on gas-to-liquid mass flowrate ratio (GLR).

$$\frac{P(z)}{P_a} = 0.172 + 0.732 exp\left[-0.371\theta^{-0.203}\left(\frac{l_m}{d_m}\right)^{-0.422}\left(\frac{d_m}{d_g}\right)^{5.152} GLR^{0.988} - 1.286\left(\frac{z}{l_m}\right)^{1.251}\right] \quad (2.5)$$

Another parameter used for the analysis of internally mixing twin-fluid Y-jet atomizer is the 'Liquid-to-Gas Momentum

Ratio' (φ, Equation 2.2); this is the ratio of the momentum of the liquid jet going into the mixing port and momentum of the auxiliary fluid (air or steam). This ratio was first used by (Michhele, et al., 1991) for the analysis of twin-fluid Y-jet atomizers. It is used in previous studies by (Song & Lee, 1996), (Andreussi, et al., 1992), (Mlkvik, et al., 2015) and (Nazeer, et al., 2018).

Flowing is the correlation based on liquid-to-gas momentum ratio for the pressure drop along the length of the mixing chamber ($P(z)/P_a$) proposed by pacific & Yanagihara:

$$\frac{P(z)}{P_a} = 0.172 + 0.764 exp\left[-0.048\theta^{0.072}\left(\frac{l_m}{d_m}\right)^{-0.309}\left(\frac{d_m}{d_a}\right)^{4.536} \varphi^{-0.371} - 1.286\left(\frac{z}{l_m}\right)^{1.251}\right] \quad (2.6)$$
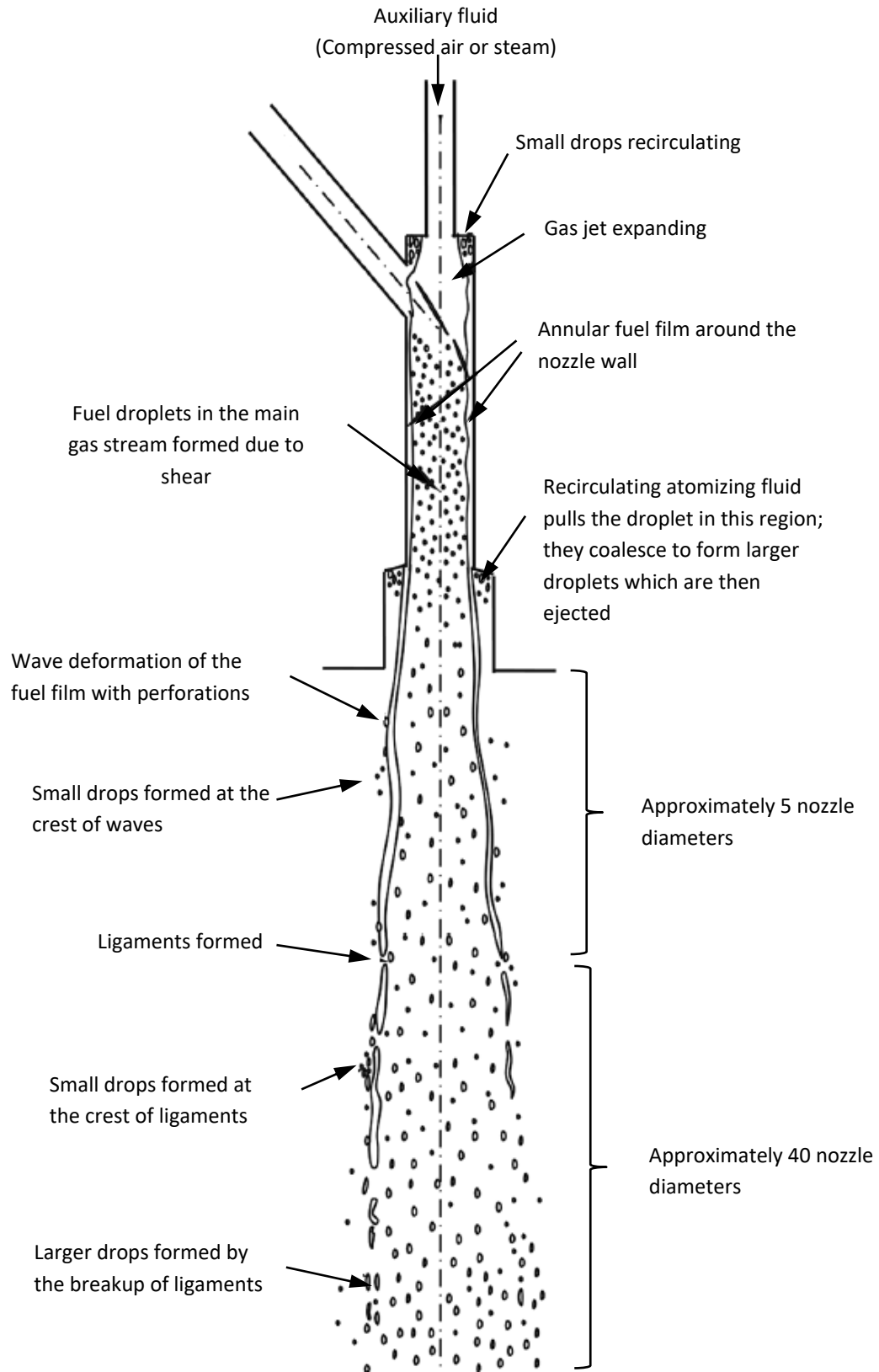
Figure 2.3 Liquid atomization in Y-jet atomizer. Figure adopted from (Mullinger & Chigier, 1974).

The following labels appear in the figure:

Auxiliary fluid (Compressed air or steam)

Small drops recirculating

Gas jet expanding

Annular fuel film around the nozzle wall

Fuel droplets in the main gas stream formed due to shear

Recirculating atomizing fluid pulls the droplet in this region; they coalesce to form larger droplets which are then ejected

Wave deformation of the fuel film with perforations

Small drops formed at the crest of waves

Approximately 5 nozzle diameters

Ligaments formed

Small drops formed at the crest of ligaments

Approximately 40 nozzle diameters

Larger drops formed by the breakup of ligaments

Ferreira et al (Ferreria, et al., 2009) demonstrated that under certain experimental conditions, the atomizing fluid flow is choked in internally mixing chamber twin-fluid atomizer. Sonic conditions are achieved at different mass flow rates as a function both of the air/gas channel diameter and liquid mass flow rate. They found that under chocked conditions, there is a certain channel diameter that produced the smallest Sauter Mean Diameters (SMD).

2.4 Airblast Atomizers

Principally, airblast atomizers function exactly in the same manner as air-assist atomizers, both utilize the kinetic energy of the gas stream to shatter the liquid sheet or jet into the ligaments and subsequently into drops. The main difference lies in the quantity and velocity of the auxiliary fluid used for the atomization. Air-assist atomizers use small quantities of air or steam flow at very high velocities (usually sonic), whereas airblast atomizers employ a large quantity of gas flowing at much lower velocities ($< 100 \ m/s$) (Lefebvre, 1980). Airblast atomizers are thus ideally suited for atomizing liquid fuels in continuous-flow combustion systems such as in the combustors of air-craft, marine and industrial gas turbines (Heng, et al., 1996), where air velocity of the required magnitude is readily available. Most of the atomizers in service now are prefilming type (Roudini & Wozniak, 2018) and (Inamura, et al., 2019), where the liquid is first spread out in thin continuous sheets and then subjected to atomization action of high-velocity air.

Due to inherent simplicity, a variety of design configurations are available. However, the basic objective of all the designs is the same, namely to utilize the available air in the most effective manner to achieve the best possible level of atomization. Hybrid airblast atomizer (Levy, et al., 2005) and (Li, et al., 2018), which is essentially a prefilming airblast atomizer with the addition of simplex nozzle, is used in high-performance aircraft engines. The advantage of hybrid airblast atomizer over pure airblast atomizer is that good atomization even at low air velocities associated with lower cranking speed could be achieved. Another type of airblast atomizer, which finds application specifically in industrial gasturbine application, is plane-jet airblast atomizer. (Jasuja & Rosfjord, 1979). In it, fuel is injected into the high-velocity circulating air stream in the form of one or more discrete jets.

2.5 Effervescent Atomizer

The effervescent atomization technique was developed in the late 1980s by Lefebvre and co-workers (Lefebvre, et al., 1988a), (Lefebvre, 1988b), (Roesler & Lefebvre, 1989) and (Wang, et al., 1989). They termed it aerated-liquid atomization. Though the term 'effervescent atomization' was used colloquially right from its inception, it did not appear in any publication until the work of Buckner (Buckner, et al., 1990a) and (Buckner, et al., 1990b).

In all the twin-fluid atomizers described earlier, steam or air is used to augment the atomization or is used as a primary driving force for the atomization, have one thing in common: the bulk liquid to be atomized is first transformed into a jet or sheet before being exposed to high-velocity air. In contrast, in effervescent atomizers, the atomizing gas is injected into the bulk liquid at low velocity to form a bubbly two-phase mixture upstream of the discharge orifice. Due to its relatively low density, the atomizing gas occupies the significant proportion of the total cross-sectional flow area. This improves atomization by reducing the characteristic liquid dimensions in the discharge orifice. Moreover, the atomization process is further improved by the abrupt expansion of bubbles at the nozzle exit that shatters the emanating liquid stream into ligaments and droplets (Sovani, et al., 2001). Figure 2.4 depicts the schematic of the effervescent atomization mechanism.
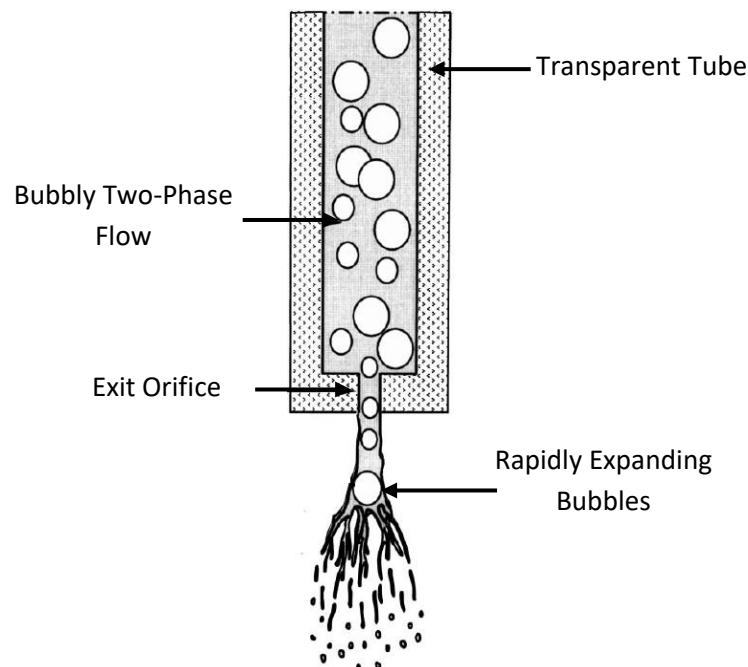
Figure 2.4 Schematic of the atomization observed by Roesler and Lefebvre (Roesler & Lefebvre, 1988).

15

Chapter 3: Atomization

3.1 Introduction

Gas-liquid multiphase flows widely occur in nature and environment, as an example falling of raindrops and various spray processes. An important type of gas-liquid multiphase flows, in practical application, is a jet flow with initial momentum driving the breakup of the liquid into small droplets. The conversion of the bulk liquid into sprays containing small droplets in the gaseous atmosphere is essential for a broad range of practical applications. Sprays are encountered in various environmental, medical, engineering and biomedical applications.

The atomization process primarily involves the conversion of the bulk liquid into small droplets. Although it does not usually imply that the liquid particles are reduced to atomic sizes, spray drops from atomization can be very small. It could be thought of as disruption of the consolidating effect of surface tension by the action of the internal and external forces. These forces could be due to surface displacements, pressure or velocity fluctuations, in the supply system or on the jet surfaces, as well as fluctuation in the liquid properties such as temperature, viscosity or surface tension coefficient. When such disruptive forces are not present, surface tension tends to pull the liquid into the form of a sphere, since this configuration has minimum surface energy. Liquid viscosity opposes any change in liquid geometry by exerting stabilizing influence. Contrarily, aerodynamic forces acting on the liquid surface may promote the disturbances/instabilities. Eventually, the breakup of the liquid jet occurs when the disruptive forces overcome the consolidating effect of the surface tension.

Droplets and ligaments produced in the initial disintegration process are unstable and further undergo disintegration process into smaller drops. Hence, the final range of drop size produced not only depends on the primary atomization but also on the extent to which these drops are further disintegrated in secondary atomization.

In this chapter primary, secondary and prompt atomization are precisely discussed. The mechanism of atomization in Y-jet atomizer and multiphase flow regimes within the mixing chamber of the nozzle are discussed in detail.

3.2 Primary Atomization

The process of the liquid jet breakup has been studied both experimentally and theoretically over a period of more than 100 years. A detailed review of jet flow was made by Krzywoblocki (Krzywoblocki, 1957), and other reviews relevant to jet flows are also available (Lin & Reitz, 1998; Lin & Kang, 1987; Yoon & Heister, 2003; Birouk & Lekic, 2009; Sirignano & Mehring, 2000). When a liquid jet emanates from the nozzle in the form of a continuous cylindrical body, the imbalance between the cohesive and disruptive forces on the surface of the jet give rise to the oscillations and perturbations. These oscillations are amplified under favorable conditions, leading to the disintegration of the jets into droplets. This phenomenon is referred as 'Primary Atomization.' It is an example of complex gas-liquid multiphase flow: near the nozzle, the liquid, initially injected as a continuous jet, disintegrates into ligaments and droplets of varied size by interacting with the gas. If the drops and ligaments produced during Primary Atomization are larger than the critical size, they further disintegrate into smaller droplets. This phenomenon of further disintegration is referred as 'Secondary Atomization.'

From a general point of view, two major factors drive the atomization phenomena, namely, the initial disturbances on the gas-liquid interface and a mechanism that allows some of these disturbances to grow, leading to the breakup of the liquid jet. The characteristics of the resulting spray depend on both factors.

The first experimental study concerning liquid jet flow instability has been conducted by Bidone (Bidone, 1829) and Savart (Savart, 1833) in the first half of the nineteen century. Plateau (Plateau, 1945) was first ever to make a theoretical investigation into jet instability. He revealed that a cylindrical column of the liquid jet is unstable if its length exceeds its parameter. Rayleigh (Rayleigh, 1878) used the method of small disturbances to study the conditions necessary for the breakup of the slow-moving liquid jet. It could be concluded from Rayleigh's analysis that under laminar flow conditions of non-viscous jets, all disturbances on a jet with wavelengths greater than its circumferences will grow. Moreover, his results imply that one class of disturbance will develop fastest and finally lead to the breakup. Albeit, in reality,

liquid jets are turbulent, viscous and are subjected to the influence of surrounding air, Rayleigh's theory of jet breakup is considered as a valid first approximation.

Later, Tyler (Tyler, 1933) carried experiments to measure the droplet formation frequencies as liquid jet disintegrated; and related it to the wavelength of disturbances. His experimental results have a strong agreement with Rayleigh's mathematical analysis of liquid jet disintegration. He concluded that maximum instability in the liquid jet consequently leads to the breakup of the jet, as predicted by Rayleigh's theory.

Weber (Weber, 1931), extended the Rayleigh's analysis to include the effect of viscosity and provided a more general theory of liquid jet disintegration at low velocities. He argued that the surface forces would dampen out the disturbance if the wavelength of the initial disturbance is less than λ_{min}, on the other hand, if the wavelength is greater than λ_{min}, the surfaces forces tend to increase the disturbance, that will finally lead to the disintegration of the liquid jet. However, there is one specific wavelength, λ_{opt}, that is most suitable for the drop formation.

3.3 Secondary Atomization

When an initially spherical droplet is encountered by ambient flow field moving at a relative velocity to it, aerodynamic force may cause it to deform and eventually collapse into smaller droplets. This process of further fragmentation is referred to as secondary atomization. It is in contrast to the primary atomization, where the bulk liquid in the form of the liquid jet is initially disintegrated into ligaments and droplets. In spray formation, primary atomization occurs at or near the nozzle orifice. This may be followed by secondary atomization, which typically occurs downstream.

Secondary atomization is encountered in vast variety of applications, such as mass spectrometry (Hassell, et al., 1991), internal combustion engines (Boggavarapu & Ravikrishna, 2013), industrial boilers (Broukal & Hajek, 2011), aero engines (Rachner, et al., 2001), coating (Andrade, et al., 2012), painting (Li, et al., 2019) and material processing (Lagutkin, et al., 2004) etc. The aim in almost all of the applications is to control the final droplet size. It is the main reason from the scientific and industrial point of view to study the secondary atomization to determine the conditions that lead to appropriate droplet sizes. In combustion application, for instance, it is desirable to produce small droplets in order to increase the

surfaces area of the fuel and hence consequently increase the evaporation and mixing rates. Interestingly, as pointed by Tryggvason (Tryggvason, 1997), the highest ambient velocity does not always produce the smallest droplet diameters. Hence, a clear understanding of the secondary breakup is necessary to identify the flow conditions that would produce the desired size of droplets.

Due to the acceleration of the ambient fluid around the droplet, the unequal pressure distribution is established on the droplet surface, leading to the deformation of initial spherical shape. The interfacial tension and viscous force resist this deformation. Nevertheless, if the aerodynamic forces are large enough, the drop will eventually go through further fragmentation (Hinze, 1955). The mode of drop disintegration depends on whether the drop is subjected to steady acceleration or is suddenly exposed to high gas velocity stream. This is proved experimentally by Lane (Lane, 1951) and confirmed theoretically by Hinze (Hinze, 1955). Under steady acceleration, the drop becomes increasingly flattened, and at a critical relative velocity, it is blown out into the form of the hollow bag attached to a roughly circular rim. The bag produces a shower of very fine droplets on disintegration, while the rim, which contains most of the mass of the droplet, is broken into larger droplets. In contrast, a droplet exposed suddenly to a fast air/gas stream disintegrates in an entirely different manner. The drop is deformed in the opposite direction; a convex surface is formed to the flow of air. The edges of the saucer shape are drawn out into a thin sheet and then into fine filaments, which break into drops.

3.4 Prompt Atomization

Keeping in view the theories of all the above mentioned models of the liquid jet breakup, it is postulated that liquid sheet or jet breakup occurs via classical wavy sheet/jet mechanism. As per this mechanism, liquid surfaces take on some form of instability that grows as waves. The most rapidly growing wave become detached from the leading edge of the liquid surface to form a ligament, that is subsequently fragmented into droplets. The size of the droplets is dependent on the diameter of the ligaments from which they are formed. These ligament diameters, in turn, are dependent on the liquid jet or sheet thickness. Hence the mean droplet size in a spray is dependent on the initial jet diameter or sheet thickness as postulated theoretically by Dombrowski et al. (Fraser, et al., 1985) and demonstrated experimentally by Rizk and Lefebvre (Rizk & Lefebvre, 1953). An important prerequisite for the wavy structure formation on the surface of the liquid jet is sufficient time for the waves to develop. In many

cases, enough time is available, because the air and the liquid are co-flowing, and there is no significant component of air velocity in a direction that could promote repaid disintegration of the liquid sheet/jet. Nevertheless, if, the atomizing air is arranged such that to impinge on the liquid sheet at an appreciable angle, as shown in Figure 3.1, it now has a sufficient transverse component of velocity. As a consequence, the liquid sheet emanating from the nozzle has no time to develop wavy structure but rather is shattered into small fragments by the vigorous interaction created between the liquid and impinging air jet. Lefebvre termed this mechanism 'Prompt Atomization' (Lefenvre, 1992). Under this mechanism of atomization, the maximum critical size of the fragments produced depends primarily on the magnitude of the air velocity component normal to the liquid sheet, the surface tension and gas to liquid mass flow rate ratio. An important feature of this mode of atomization is that the violent and sudden fragmentation of the liquid sheet into drops ensures that the ensuing droplet sizes are much less dependent on the initial sheet thickness.
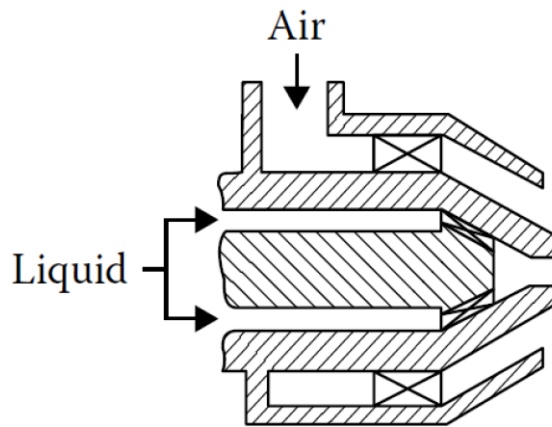
Figure 3.1 External mixing air-assist atomizer.

3.5 Atomization by Internally-Mixing Twin-Fluid Y-Jet Atomizer

Unlike other twin-fluid atomizers, the atomization mechanism of internally-mixing twin-fluid Y-jet atomizer is relatively poorly understood. Primarily owing to its limited commercial use, namely in industrial boilers operating with light fuel oil and in powder production. The spraying performance (mean droplet size) is reported to be affected by properties of gas and liquid, injection pressure, and also by the geometric configurations such as the mixing-port size and the intersecting angle between the

liquid and gas port. Mullinger and Chigier (Mullinger & Chigier, 1974) and Prasad (Prasad, 1982) studied the effect of geometric parameters on the mean drop size and suggested the design criteria to generate the fine drops. Song and Lee (Song & Lee, 1994) conducted the experimental examination, with water and air as test fluids, to study the effect of mixing port length on the Y-jet atomizer's spray performance. They concluded that the mean droplet size decreases and becomes spatially even as the mixing port length is reduced.
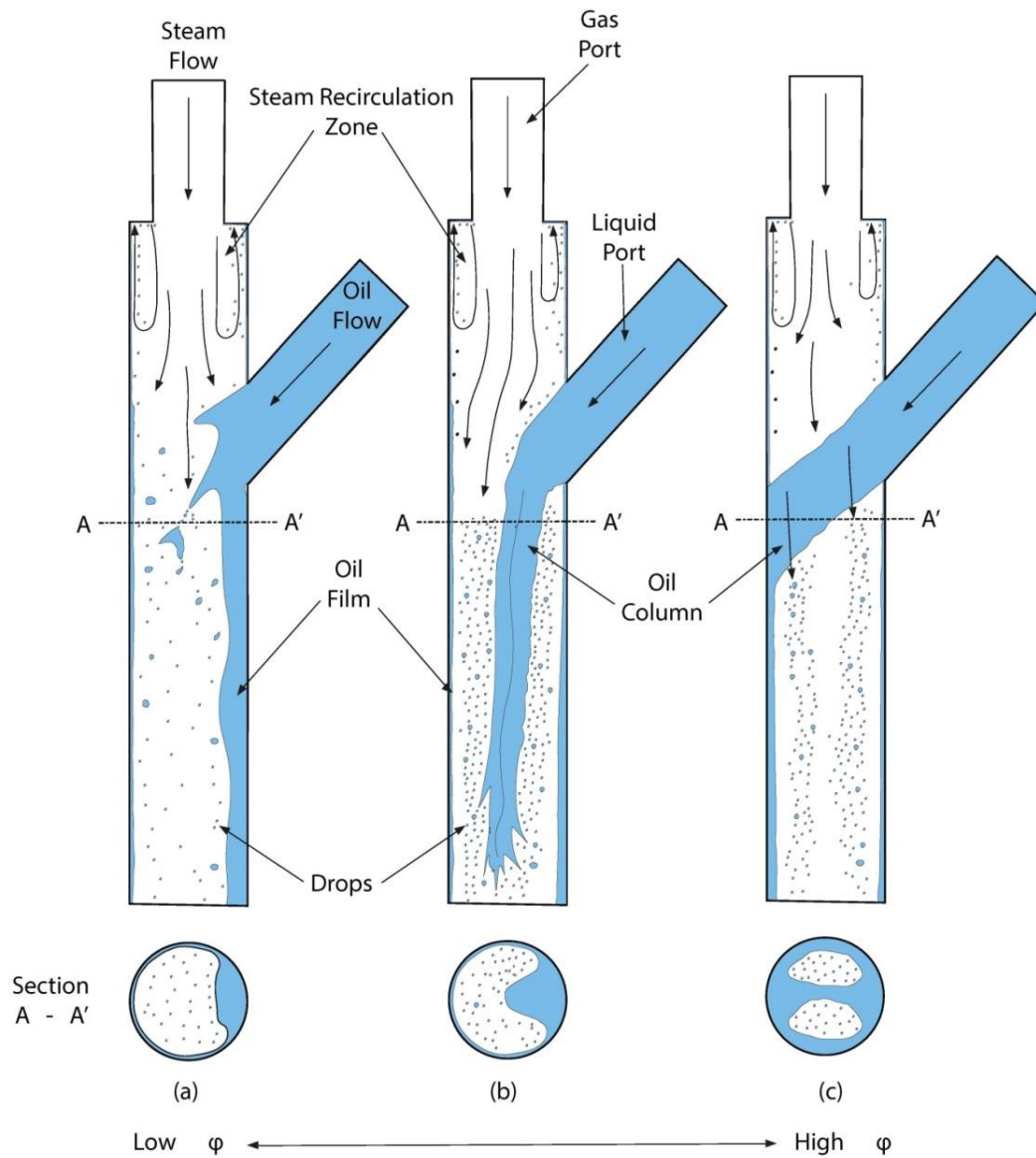
Figure 3.2 Schematic illustration of the flow pattern in internally-mixing twin-fluid Y-jet.

In a classical study, with water and air as working fluids, Song and Lee (Song & Lee, 1996) studied the atomization mechanism of the gas-liquid mixture flowing through internally mixing twin-fluid Y-jet atomizer by examining both the internal and external nozzle flow patterns. They compared two operational parameters, namely, gas-to-liquid mass flow rate ratio (GLR) and liquid-to-gas momentum ratio to describe the internal and external flow patterns. The latter was considered to be an appropriate parameter to describe both the internal flow and spray characteristics. Figure 3.2 shows the schematic illustration of the flow pattern in internally-mixing twin-fluid Y-jet atomizer. As the high-speed gas stream impinges on the liquid jet emanating from the liquid port, the instabilities in the liquid jet are amplified and initial breakup occurs within the nozzle. A part of the gas stream expanding from the gas-port into the mixing-port recirculates; leading to the reverse flow of the liquid film on the nozzle wall (Figures 3.2). When the liquid-to-gas momentum ratio is low (Figure 3.2a), the momentum of the gas stream dominates, the flow is annular flow with the thicker film formation on the liquid-port-side-wall of the nozzle and the core of the gas has entrained droplets. As the liquid-to-gas momentum ratio increases, main part of the liquid stream penetrates into the center of the mixing-port. In this case, the main gas stream is very much diverted towards the opposite side wall. Thus a sizeable amount of liquid at the opposite wall is entrained into the gas core by the highly deflected gas stream. When the liquid-to-gas momentum ratio increases further (Figure 3.2c), liquid jet momentum dominates and a part of the liquid column touches the opposite side of the wall. With this condition, the gas stream has to flow around the liquid column as shown in Figure 3.2c.

The atomization model within in Y-jet atomizer proposed by Mullinger and Chigier (Mullinger & Chigier, 1974); see Figure 2.3 for the details, Song and Lee (Song & Lee, 1996) and Andreussi et al. (Andreussi, et al., 1992) is almost the same. Figure 3.3 shows the schematic illustration of the atomization mechanism of the Y-jet atomizer proposed by Song and Lee. The main difference is that the internal atomization mechanism proposed by Song and Lee is subdivided into three parts based on flow visualization. The first one is the "direct collision," denoted by region A in Figure 3.3, which is characterized by the direct impingement of the gas stream upon the liquid column and generation of the drops near the exit of the liquid port. The next mode (B in Figure 3.3) is the "entrainment/deposition," which exhibits nonuniform circumferential film thickness in the widest range of the liquid-to-gas momentum ratio. Drops here are generated by the sharing action of the high-speed gas flow and the annular liquid film. At the same time, within this region, some of the drops produced in direct collision mode coalesce and deposit on the

liquid film. The third mode is the "liquid film disintegration," denoted by region C in Figure 3.3. Here the liquid film disintegrates into ligaments and then into large droplets outside the atomizer.

Wigg (Wigg, 1959) analysis on the atomization mechanism of the airblast atomization indicated the kinetic energy difference between the inlet gas and the emerging spray as a dominant factor affecting the mean drop size in the spray. In a latter work (Wigg, 1964), Wigg utilized the spray data of Clare and Radcliffe (Clare & Radcliffe, 1954) and Wood (Wood, 1954) on the airblast atomizer, to derive the dimensionless expression for the mass median diameter. It is interesting to note that Mullinger and Chigier (Mullinger & Chigier, 1974) found good agreement between their experimental data for the mass median diameter produced by internally mixing twin-fluid Y-jet atomizer and the dimensionless expression for the mass median diameter provided by Wigg for airblast atomizer.
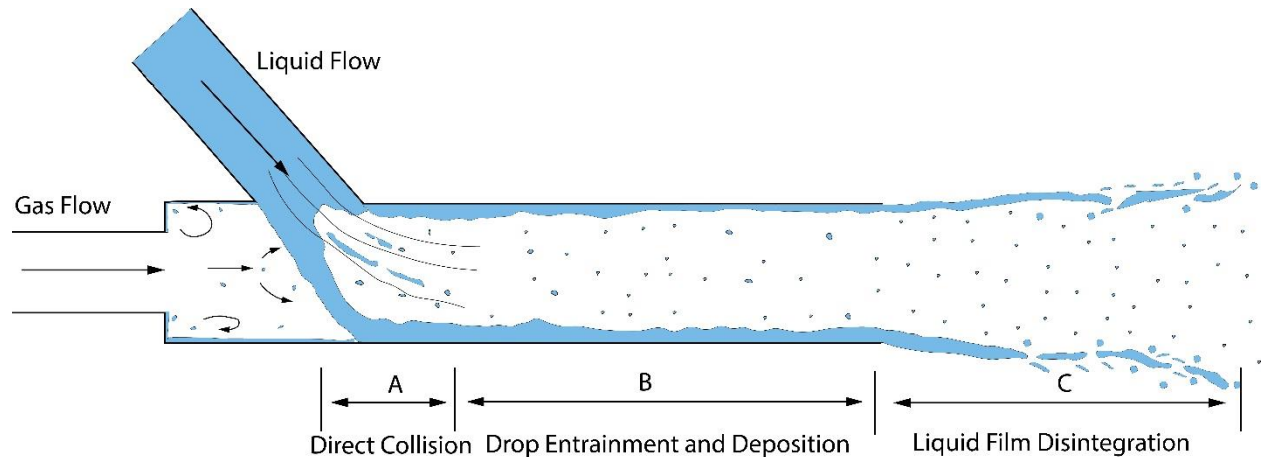
Figure 3.3 Schematic of atomization mechanism in Y-jet atomizer proposed by Song & Lee (Song & Lee, 1996).

Inamura and Nagai (Inamura & Nagai, 1985) used the geometry similar to internally mixing twin-fluid Y-jet atomizer to flow air at uniform velocity; the main difference is that instead of liquid port a thin annular slot was used to inject the liquid along the inside wall of the nozzle. Ethanol, water and glycerin were used as working fluids alongside air to investigate the effect of liquid properties on the atomization. For the low liquid flow rates and air velocities, they observed that disturbances of large wavelengths in the liquid flowing along the nozzle wall were responsible for the liquid film breakup into the drops through the formation of the unstable ligaments at the end of the wall. They termed this process as "atomization by ligament formation." Increase in the velocity of the air and liquid flowrate caused the wavelengths of the disturbance to vanish so that the liquid emerged at the end of the nozzle as a

23

continuous liquid film. They called the resulting atomization of this film by high-velocity air as "atomization by film formation." Figure 3.4a shows the effects on Sauter Mean Diameter (SMD) by the variations in the air velocity and gas to liquid mass flow rate ratio. The curves drawn in the figure exhibit the change in the slope, which is attributed by Inamura and Nagai to the transition from one mode of atomization to the other. It is of interest to note that the value of the gas-to-liquid mass flow rate ratio at which the transition occurs increases with the increase in the gas velocity.

Figure 3.4b depicts the effect of viscosity on the Sauter Mean Diameter (SMD) of the droplets. Like all other types of twin fluid atomizer, the data plotted confirms that this type of atomizer produces larger Sauter Mean Diameters (SMD) with increasing liquid viscosity, regardless of air velocity.
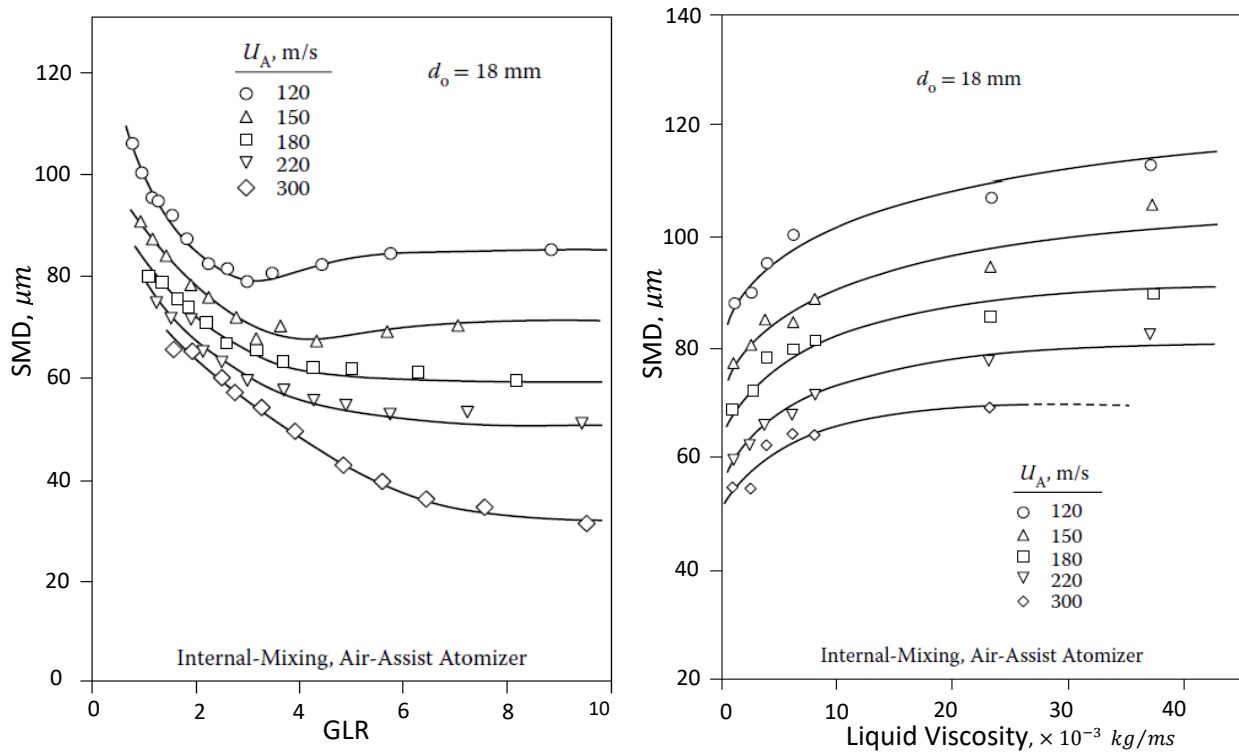
Figure 3.4 Variation in the mean drop size (a) with the gas velocity and gas to liquid mass flow rate ratio (GLR) (b) with liquid viscosity (Inamura & Nagai, 1985).

3.6 Flow Regimes in Internally Mixing Twin-Fluid Atomizers

Different flow patterns within the internally mixing twin-fluid atomizers lead to different mechanisms for the atomization process and also influences the spray characteristics. For example, when a bubbly flow regime dominates in the mixing chamber of the nozzle, liquid breakup relies on the bubble rupture mechanism. If a dispersed flow regime exists within the mixing chamber, then the resulting ejecting multiphase flow through the discharge orifice is to disintegrate the larger droplets and ligaments by the process of the secondary atomization. At certain operating conditions, especially at higher gas-to-liquid mass flow rate ratios (GLR), the division between the primary atomization inside the nozzle and secondary atomization outside is extremely important (Chin & Lefebvre, 1993).

The complexity of two-phase flow arises from the wide variety of flow patterns that can exist. It is evident from Figures 3.5 and 3.6 that gas-liquid multiphase flow can distribute itself in a variety of ways. Chin and Lefebvre (Chin & Lefebvre, 1992) examined the flow regimes available in the literature for horizontal two-phase flows for their relevance to effervescent atomization. Latter in another study (Chin & Lefebvre, 1993), they extended the scope of their previous study to include various types of internally mixing twin-fluid atomizers and other flow configurations, including vertically downwards multiphase flow. To my knowledge, no reliable theoretical model has been developed that can predict the type of flow pattern that will occur under any given set of operating conditions. Nevertheless, flow patterns have been reported in the literature and correlated empirically using parameters based on various combinations of flow rates and flow properties (Oshinowo, 1974) (Baker, 1954) and (Spedding & Nguyen, 1980). The transition between one flow pattern to another takes place slowly and is open to subjective interpretation; hence the boundaries between the different flow regimes cannot be precisely defined. Similarly, the description, identification and naming of the various flow patterns have lacked consistency between different investigators.

Following are the flow regimes that could arise in vertical flows:

Bubbly

The gas phase is distributed more or less uniformly in the form of discrete bubbles in a continuous liquid phase.

Coring bubbly

This is also a bubbly flow, but the bubbles move towards the axis of the tube to form a core of dispersed bubbles.

Falling film

The liquid flows in the form of a thin film.

Falling bubbly film

This is similar to falling film, but the liquid film is thicker and contains small dispersed bubbles.

Annular

The liquid flow as a thin wavy film along the wall of the pipe/duct and the gas flows as a core. The gas core may contain entrained droplets that have been stripped off the wavy film.

| Bubble | Slug | Churn | Annular |
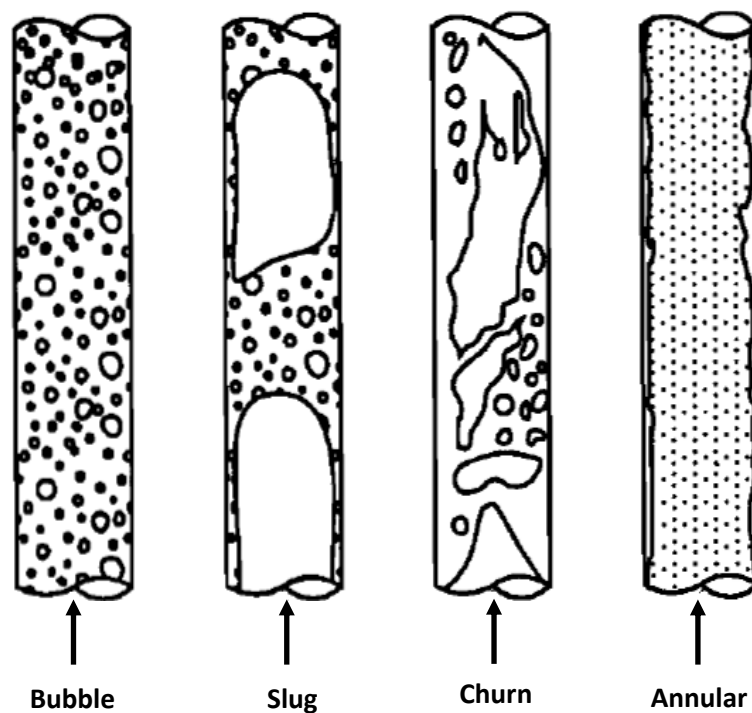
Figure 3.5 Flow pattern in vertical flow (Oshinowo, 1974).

Slug

The gas and liquid redistribute themselves axially so that at any cross-section the flow rates of the gas and liquid vary with the time. The gas flows mainly in the form of large bubbles, which occupy most of the duct's cross-sectional area and can vary in length up to several times the diameter.

Churn

Churn flow is mostly observed during the transition from the bubbly to annular flow. It is similar to slug flow but is characterized by a more chaotic and alternating motion of the liquid.

Stratified Smooth

Stratified Wavy

Stratified

Elongated Bubble

Slug

Intermittent

Annular / Annular-Mist

Wavy Annular

Annular

Dispersed

Dispersed
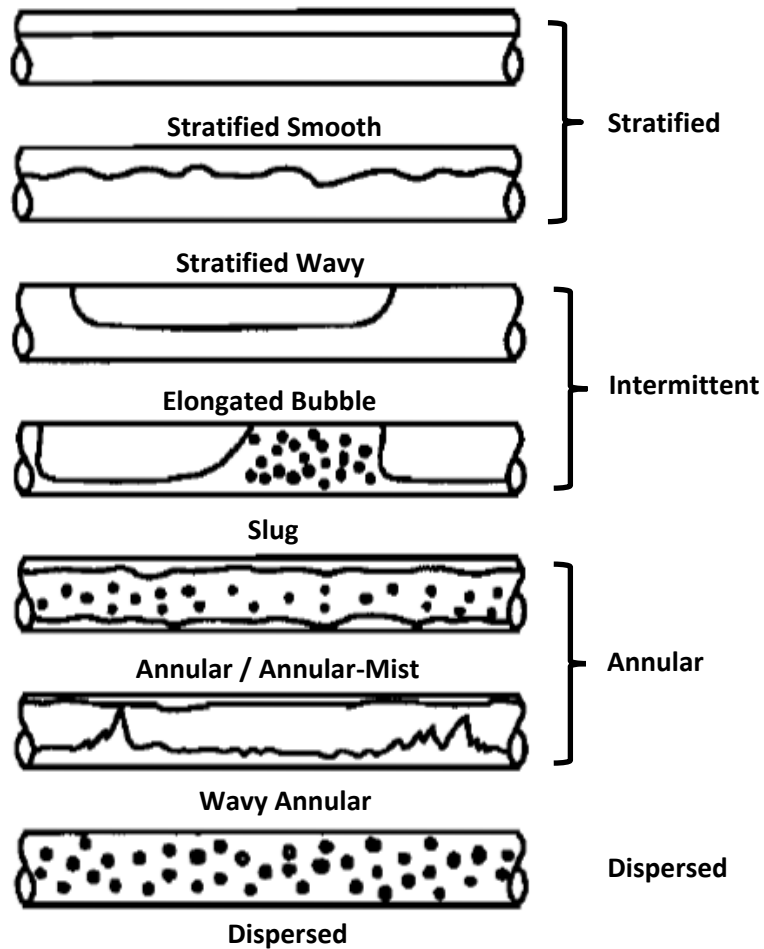
Figure 3.6 Flow patterns in horizontal flow (Baker, 1954).

Froth

The bubbles disintegrate and combine with the liquid to form a frothy mixture. A forth is essentially a two-phase system with a three-dimensional structure of thin liquid films acing as individual compartments for the gas.

Dispersed

This corresponds to atomization. All the liquid is entrained by the gas in the form of droplets.

The key flow regimes for vertical multiphase flow are illustrated in Figure 3.6. Likewise in vertical multiphase flow, the bubble, forth, slug, annular and dispersed flow patterns, as described above, are also found in horizontal two-phase flow. In addition, the following flow patterns are sometimes observed in horizontal flows, as illustrated in Figure 3.7.

Stratified

In this type of flow pattern, both phases are continuous in the flow direction. Liquid flows along the bottom of the duct while the gas at the top.

Wavy

This flow pattern is similar to the stratified flow, but the only difference is that the gas-liquid interface has waves traveling in the direction of the flow.

Chapter 4: Numerical Methods

4.1 Introduction

CFD is the most common and popular numerical modelling technique. It has become quite popular over the last couple of decades with increasing power of the computers. It is based on the principles of fluid mechanics; utilizing numerical methods and algorithms to solve problems that involve fluid flows. In this chapter, approaches that can be used to model multiphase flows and associated turbulence are briefly discussed. The Volume of Fluid (VOF), Discrete Phase Model (DPM) and Mixture multiphase models, along with, Wall Modeled Large Eddy Simulations (WMLES) and $K\omega$ turbulence models are discussed in detail.

4.2 Multiphase Flow Modeling

There are two different ways in which two-phase flow are commonly represented in CFD, namely the "Eulerian" method, where the flow is considered as continuous across the whole flow domain and the "Lagrangian" method, where the paths taken by the particles/droplets are tracked through the domain (Jang, et al., 2010). In the Langrangian particle tracking approach, the gas phase is still represented using an Eulerian approach by solving the governing equations of the flow, but the liquid spray is represented by a number of discrete "computational particles," which are tracked by solving the particle's equation of the motion. The fundamental assumption made in this approach is that the dispersed secondary phase occupies a low volume fraction (typically bellow 10%) (El-Batsh, et al., 2012). Therefore, this approach is not appropriate to model the multiphase flow within the nozzle where the volumetric effect of the secondary phase cannot be neglected. Eulerian methods could be further classified into single-fluid, such as relevant mixture and VOF models, and multi-fluid approaches like Eulerian multiphase and multi-fluid VOF models (Crowe, 2006) and (Loth, 2009). The latter approach treats each phase as a single

independent phase but intermixed continua while the earlier treats the flow as a single-phase flow by solving a single set of conservation equations considering the mixture properties. The single-fluid approach assumes that the continuous and the dispersed phases are in local kinetic and thermal equilibrium, i.e. the relative velocities and temperatures between the two phases are small in comparison to predicted variations of the overall flow field (Lakhehal, et al., 2002). The multi-fluid approach requires a separate conservation equation for each phase, making it extremely computationally expensive and complex; hence, this rules out the possibility of utilizing it for extensive parametric studies. On the other hand, the mixture model solves a smaller number of equations as compared to the aforementioned models; however, it is not possible to track the interface between the phases. This is a major drawback for the studies aiming to identify the relevant flow regimes and track the development and fragmentation of the gas-liquid interface. The Eulerian surface tracking technique i.e. the VOF method can track with relatively good accuracy the interface between the phases; this makes it feasible to study the in-nozzle flow and primary breakup of the jets (Gopala & Berend, 2008).

Due to complexities involved in atomization and spray processes, a broad range of time and length scales are involved; approximation and modeling become inevitable in CFD of such multiphase flow phenomena. The numerical simulation of the liquid spray generation often aims in predicting drop size distribution, spray penetration length and spray cone angle. Since the liquid spends most of its residence time in the form of droplets, simulation methodologies for the dispersed multiphase flow are usually utilized. However, this method leads to spurious results for the flow within the nozzle or in the dense part of the spray. Hence hybrid Lagrangian-Eulerian methods are utilized to simulate the complete in nozzle flow and spray generation.

4.3 Volume of Fluid (VOF)

The Eulerian multiphase approach, such as volume of fluid (VOF) method, describes the dispersed phase by the same means as the continuous phase, i.e. a set of Navier-Stokes equations for the continuity and momentum transport, potentially along with transport equations for energy and other conserved quantities are solved. In the VOF method, the gas-liquid interface can be tracked by explicit discretization schemes, such as geometric reconstruction. It requires much smaller time steps and much higher mesh resolutions. The phase boundary around every droplet must be resolved by the mesh which

is significantly smaller than the smallest droplet. This allows for the relatively accurate prediction of the primary breakup. The volume displacement is inherently accounted for, which can be important for the dense part of the spray. However, this method is prohibitive in terms of computational expenses and requires large HPC resources.

The VOF formulations rely on the fact that two or more phases are not interpenetrating. The concept of the volume fraction of the phases is introduced. In each control volume, the volume fraction of all the phases sums to unity. The fields for all the variables and properties are shared by the phases and represent volume-averaged values. Thus the variables and properties in any given cell are either purely representative one of the phases, or representative of a mixture of the phases, depending on the volume fraction values. In other words, if the qth fluid's volume fraction in the cell is denoted as α_q, then the following three conditions are possible:

- $\alpha_q = 0$: The cell is empty of the qth fluid.
- $\alpha_q = 1$: The cell is full of the qth fluid.
- $0 < \alpha_q < 1$: The cell contains the interface between the qth fluid and one or more other fluids.

4.4 Mixture Model

The mixture model is a simplified multiphase model that could be used to model the flow where phases move at different velocities but assume a local equilibrium over short spatial length scales. It solves the mixture momentum equation and prescribes relative velocities to describe the dispersed phase (Kallio & Akademi, 1996).

The mixture model, like the VOF model, uses a single-fluid approach. It differs from the VOF model in two respects:

- The mixture model allows the phases to be interpenetrating. The volume fraction α_q and α_p for a control volume can therefore be equal to any value between 0 and 1, depending on the space occupied by phase q and phase p.
- The mixture model allows the phases to move at different velocities, using the concept of slip velocities.

4.5 Discrete Particle Method (DPM)

In Eulerian-Lagrangian multiphase approaches (Jiang, et al., 2010), referred to as Discrete Particle Methods (DPM), the gas/carrier phase is still represented by solving the governing equation of the flow, but the liquid phase is represented by a number of discrete computational particles, which are tracked through the domain by solving the particle's equation of motion. Particle tracker uses physical properties of individual droplets in order to account for the exchange of mass, momentum and energy etc. with the continuous phase. This approach is relatively inexpensive since it allows the mesh to be coarser than the size of the droplets. However, the gas volume displacement is usually ignored; this may affect the solution's accuracy, hence these so-called dense models have been developed (Tonini, et al., 2008). Furthermore, in the regions where spray does not consist of discrete spherical droplets, special models must be employed to predict the primary breakup of the initial contiguous jet.

4.6 VOF-to-DPM

ANSYS Fluent provides the capability to combine the above-mentioned approaches namely VOF and DPM through VOF-to-DPM transition mechanism. The initial jet and its primary breakup are predicted using VOF formulations on a sufficiently fine mesh, while the resulting dispersed part of the spray is predicted by the DPM. The ElSA model (Vallet, et al., 2001) and (Nykteri, et al., 2020) is another alternative approach that provides a dynamic transition between a Eulerian and a Lagrangian framework in the primary and secondary liquid sprays atomization regions, respectively. However, ELSA model is not integrated into ANSYS Fluent. The hybrid VOF-to-DPM model automatically finds the liquid lumps detached from the liquid core in the VOF solution. It then checks for their eligibility for the VOF-to-DPM model transition against the user-specified criteria of the lump size and asphericity. If a liquid lump satisfies the criteria, the liquid lump is removed from VOF solver and converted to a point mass in the Lagrangian formulations. Converting liquid lumps to Lagrangian formulation does not impose volume displacement on the continuous phase VOF flow simulations. In order to circumvent spurious momentum sources, a volume of a gas with the same volume as the liquid lump is created in the VOF simulation to maintain the volume conservation. The hybrid VOF-to-DPM model is validated against the experimental studies to determine the Sauter mean diameter (SMD) drop size distribution for a liquid jet in air cross-flow (Schtze, et al., 2018) and (Sami, et al., 2019) and also the reverse transition mechanism

i.e. DPM-to-VOF is reported to agree well with the experimental studies to determine the film formation from the drops (Kumar, et al., 2018).
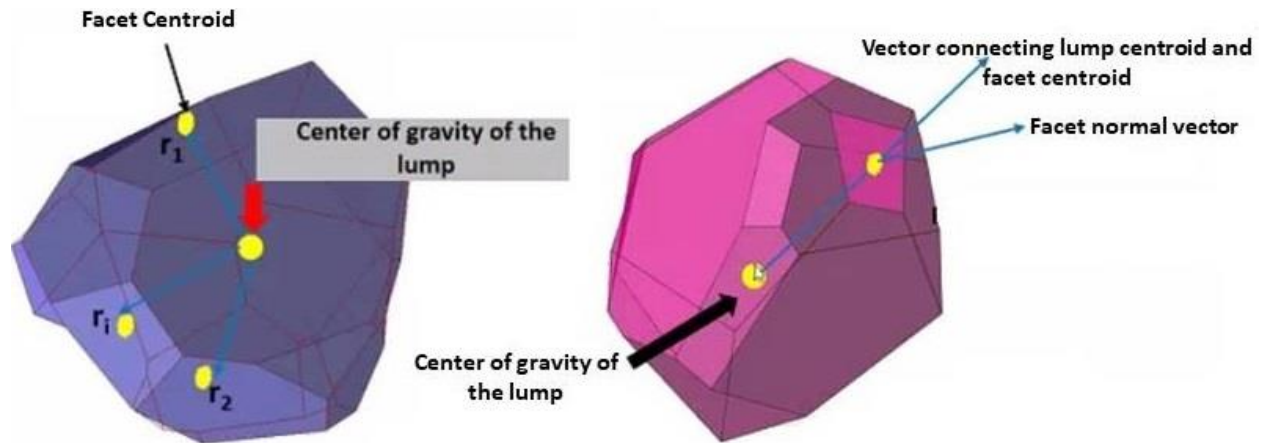
Figure 4.1 Asphericity calculation methods: (a) Normalized radius standard deviation (b) Average radius-surface orthogonality (Courtesy ANSYS Germany).

4.6.1 Transition

Asphericity is the shape base criterion used by VOF-to-DPM model to identify the liquid lumps which can be converted from the resolved liquid using the VOF model to particles tracked with the DPM model. Its value is zero for a perfect sphere. Asphericity values of the liquid lumps are determined in two ways (see Figure 4.1), namely calculated from normalized radius standard deviation and radius-surface orthogonality. In the first method, for every facet of the liquid lump surface, the distance between the facet center and the lump center of gravity is calculated and then normalized by the average radius. In the second method, for every facet of the liquid lump surface, a vector from the lump's center of gravity to the center of the lump boundary facet is computed and then used in a dot product with the facet unit normal vector. Only lumps for which the asphericity values calculated from both methods are below the user-specified maximum asphericity values are selected for the transition from VOF liquid to DPM particles.

4.7 Turbulence Modeling

There are three simulation approaches to simulate the turbulence, namely: Direct Numerical Simulations (DNS), Large Eddy Simulations (LES) and Reynolds-average Navier-Stokes (RANS) (Argyropoulos & Markatos, 2015). Turbulent flows are characterized by eddies having a wide range of time and length scales. Typically the largest length scales are comparable in size to the characteristic length of the mean flow, while the smallest length scales are responsible for the dissipation of the turbulent kinetic energy. Though the whole spectrum of the turbulent scales could be resolved by direct numerical simulation (DNS) approach by solving the Navier-Stokes equation to determine the velocity field, however, the DNS is not feasible for the practical engineering problems involving high Reynold numbers flows. Since the computational cost required to resolve the entire range of scales in DNS is directly proportional to the cube of the Reynold numbers, the computational cost is extremely prohibitive (Alfonsi, 2011). This approach is restricted to the flows with low to moderate Reynolds numbers. In LES, equations are solved for the filtered velocity field, which is representative of large-scale turbulent motions. The equations solved include a model for the influence of the smaller-scale motions which are not directly represented. In a RANS approach, the solution of the Reynolds equations is used to determine the mean velocity field and Reynolds stresses are obtained from the turbulent-viscosity model. The turbulent viscosity could be obtained from an algebraic relationship such as in the mixing-length model or it can be obtained from turbulence quantities such as k and ω for which modelled transport equation are solved.

4.7.1 Scale Resolved Simulations

Scale resolving technique i.e. Large Eddy Simulations (LES) can simulate turbulent flows since the 1960s. It has made significant progress over the last two decades, specifically due to a surge in computing power. Tough most of the simulations today are based on RANS models; it is becoming increasingly clear that certain classes of the flow are better covered by the models where at least part of the truculence spectrum is resolved. Such methods are termed Scale Resolving Simulations (SRS) (Menter, et al., 2011).

In Large Eddy Simulations, large eddies are resolved directly, while smaller eddies are modeled with Subgrid Scale (SGS) models. Hence LES falls between DNS and RANS in terms of the fraction of resolved

scale. The rationale behind the LES is that since the larger eddies possess most of the energy and are anisotropic in nature, they are difficult to model, while smaller eddies are isotropic in nature, and hence are easy to model. Thus, resolving only larger eddies allows the use of much coarser mesh and larger time steps in LES than in DNS. However, LES still requires considerably fine mesh and smaller time steps than those typically used for RANS calculations. In addition, LES has to be run for sufficiently long flow time to obtain stable statistics of the flow being modeled. As a consequence, the computational cost involved with LES is orders of magnitudes higher than steady RANS calculations.

4.7.2 Wall Modeled Large Eddy Simulations

The Wall modeled Large Eddy Simulations (WMLES), a hybrid LES technique, is beginning to emerge as a viable alternative to time-averaged or ensemble-averaged Navier-Stokes (RANS) turbulence modeling in industrial flows; it is able to capture flow structures larger than the grid size, while smaller scales are modeled with subgrid-scale models (SGS). The spectrum of resolved scales in LES is directly dependent on the grid resolution. This makes it extremely expensive for industrial-scale simulations, which are usually highly turbulent, wall-bounded, viscous and three-dimensional flows. Nevertheless, Wall Modeled LES (WMLES) is a substitute to classical LES and it reduces the stringent and Reynold number dependent grid resolution requirements of classical wall-resolved LES. Turbulence length scales in near-wall regions are directly proportional to wall distance, resulting in smaller and smaller eddies as the wall is approached (Naseri, et al., 2018). This effect is limited by molecular viscosity, which damps out eddies inside the viscous sublayer. Smaller eddies appear as the Reynold number increases since the viscous sublayer becomes thinner. In order to circumvent the resolution of these small near-wall scales, RANS and LES models are combined such that the RANS model covers the very near-wall layer, in which the wall distance is much smaller than boundary layer thickness but is still potentially very large in wall units (Piomelli & Balaras, 2002) and (Nikitin, et al., 2000). It then switches over to the LES formulation once the grid spacing becomes sufficient to resolve the local scales (Wen & Piomelli, 2016). This approach is similar to detached eddy simulations (Spalart, et al., 1997), delayed detached eddy simulations (Spalart, et al., 2006) and (Koukouvinis, et al., 2016) and Scale Adaptive Simulations (SAS) (Menter & Egorov, 2010). A general approach of these two approaches is that the whole or major part of the boundary layer is modeled by RANS while LES is applied only to separated flow regions. In contrast, as aforementioned, in WMLES, RANS is used only in very thinner near-wall region (Koukouvinis, et al.,

2016).

4.8 RANS

In turbulence models for Reynolds-Averaged Navier-Stokes (RANS) equations, the focus is placed on the mean flow and the effect of the flow on mean properties. Starting point is the Reynolds decomposition of the flow variables into mean and fluctuating parts, where the insertion of the Reynolds-decomposed variables into the Navier-Stokes equations, followed by an averaging of the equations, give rise to Reynolds stress tensor, an unknown term that has to be modeled in order for the RANS equation to be solved (Alfonsi, 2009). RANS turbulence models could be classified in following four types:

- Zero equation models such as Mixing Length model
- One equation models such as Spalart-Almars model (Spalart & Allmaras, 1992)
- Two equation models such as $K\varepsilon$ (Shih, et al., 1995)and $K\omega$ models (Menter, 1994)
- Seven equation models such as the Reynolds stress model (Gibson & Launder, 1978), (Launder, 1989) and (Launder, et al., 1975)

Chapter 5: Results: The Influence of Geometrical and Operational Parameters on Internal Flow Characteristics of Internally Mixing Twin-Fluid Y-Jet Atomizers

5.1 Introduction

Twin-fluid atomizers has been studied extensively over the years. Most of the studies are focused on pre-filming air blast atomizers or effervescent atomizers due to their extensive commercial use. The earlier are used extensively in aircraft, marine and industrial gas turbines and the latter are used in various applications where low injection pressures and low gas flow rates are available. There exist considerable studies on internally mixing twin-fluid Y-jet atomizers. However, the understanding of such nozzle is not very clear owing to complex aerodynamic and fluid dynamic flow pattern due to the mixing of gas and liquid within the mixing chamber.

There is a dearth of numerical studies on internally mixing twin-fluid Y-jet atomizers, probably owing to complexity involved in modeling the complex multi-phase flow pattern due to variations in length and time scales. However, there exists few numerical studies such as (Tanner, et al., 2016) focusing on the atomization and droplet break up in annular gas-liquid co-flow for internally mixing twin-fluid Y-jet atomizer, (Tapia & Chavez, 2002) focusing on the internal flow pattern. In all studies except (Song & Lee, 1996), (Andreussi, et al., 1994), (Mlkvik, et al., 2015), (Pacifico & Yanagihara, 2014) and (Tapia & Chavez, 2002), the parameters such as injection conditions and atomizer geometry were taken as input while the spray dispersion was the reported output. But the intermediate process between the input and output of the nozzle has not been investigated in detail. This study is the first to numerically model the

multiphase flow through twin-fluid Y-jet atomizer as function of the various operating conditions affecting it.

5.2 Test Case Simulated

Seven different Y-jet atomizers are used for the parametric analysis. The geometries are constructed in ANSYS Design Modeler according to the design criteria of Mullinger & Chigier (Mullinger & Chigier, 1974); the same design criteria were also adopted by Pacifico & Yanagihara (Pacifico & Yanagihara, 2014) for the experimental study on pressure drop within internally mixing twin-fluid Y-jet atomizers. The geometries are meshed in ANSYS Meshing tool. The grids are polyhedral with the number of elements ranging between 15 to 17.3 million. The Y^+ values are in the range of 0.72 - 0.94. Air and water are used as working fluids at atmospheric conditions. The schematic of the nozzle studied is shown in Figure 5.1. Table 5.1 shows the geometrical parameters of all the seven atomizers. All the pressure points as shown in the Figure 5.1 i.e. P_a, P_w, P_m, P_1 and P_2 are obtained from the numerical solutions, where P_m is the mixing point pressure, P_a is the gas (air) inlet pressure, P_w is the liquid (water) inlet pressure, P_1 is the pressure at the middle point along the length of mixing port and P_2 is the pressure near the exit of the mixing port. Mass flow boundary conditions are employed at the gas port and liquid port inlets while pressure outlet boundary condition is employed at the exit of the mixing duct.
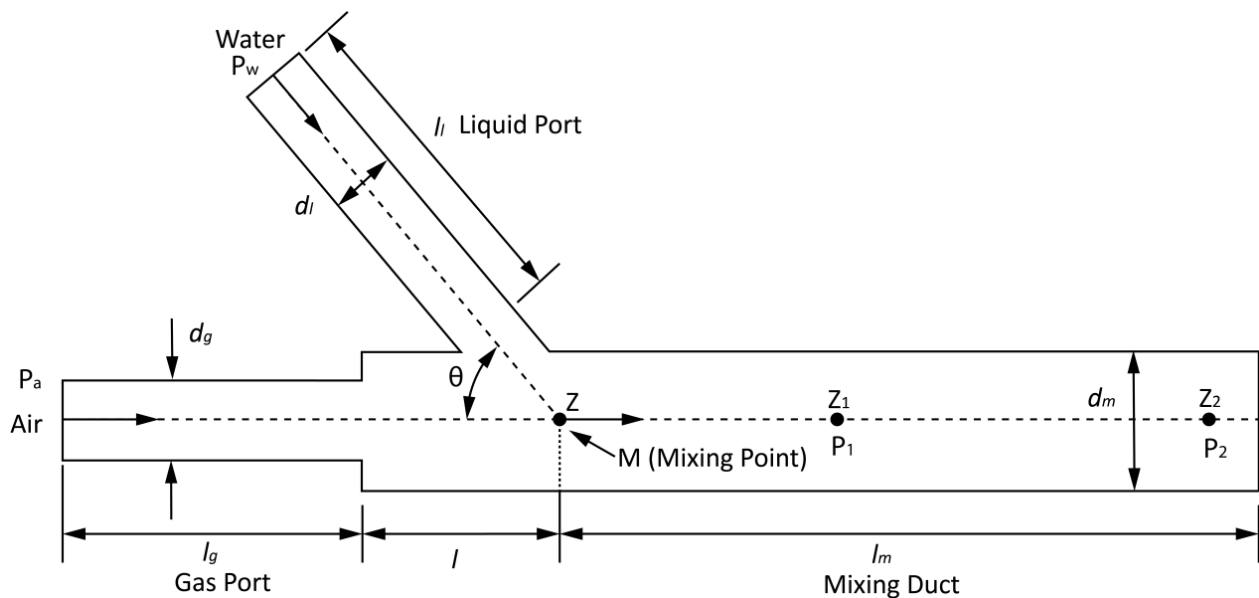
Figure 5.1 Schematic of the nozzle used for the parametric study.

In order to keep geometrical and operational similarity with the work of Pacifico & Yanagihara (Pacifico & Yanagihara, 2014), non dimensionless number i.e. Weber numbers are calculated for the flow in the mixing duct. Weber numbers used by Pacifico & Yanagihara (Pacifico & Yanagihara, 2014) are in the range of 500 – 42500, while the Weber numbers used in this work are also nearly in the same range i.e. between 600 – 45000. Weber numbers are calculated with the following formula:

$$We = \frac{\rho_{a,m} V_r^2 d_m}{\sigma}$$
(5.1)

Where $\rho_{a,m}$ is the density of the air at the mixing point, V_r is the relative velocity between the air and water, d_m is the mixing port diameter. The mass flow rate of air and water were also applied almost in the same range as stated in the literature. The mass flow rate of the air was in the range 0.008 kg/s to 0.091 kg/s while mass flow rate of the water was in the range 0.075 kg/s to 0.78 kg/s.

For each of the seven nozzles a total of 11 simulations were performed. Gas to liquid mass flow rate ratio (GLR) was varied from 0.01 to 0.9. The main geometrical parameters studied includes: the angle (θ) between liquid port and the mixing port; mixing port length to diameter ratio (l_m/d_m) and mixing port diameter to gas port diameter ratio (d_m/d_g). The values used for the aforementioned geometrical parameters are in the range: $\pi/4 \leq \theta \leq 7\pi/18$ ($45° - 70°$) ; $3.5 \leq l_m/d_m \leq 10$ and $1.67 \leq d_m/d_g \leq 2$. The following sets of atomizers were used for each of the parametric study: nozzles B, D and E are used for the parametric study of θ; B, F and G for l_m/d_m and A, B and C for d_m/d_g. These values are shown in the Table 5.1 for each nozzle.

Table 5.1 Geometric values for the parameters shown in Figure.5.1.

Nozzle	l_g (mm)	l (mm)	l_m (mm)	d_g (mm)	d_m (mm)	θ	l_m/d_m	d_m/d_g	z_1 (mm)	z_2 (mm)
A	50	14.4	50	5.5	10	57°	5.00	1.82	25	42.5
B	50	14.4	50	6.0	10	57°	5.00	1.67	25	42.5
C	50	14.4	50	6.0	12	57°	4.17	2.00	25	42.5
D	50	16.2	50	6.0	10	45°	5.00	1.67	25	42.5
E	50	13.0	50	6.0	10	70°	5.00	1.67	25	42.5
F	50	14.4	35	6.0	10	57°	3.50	1.67	17.5	27.5
G	50	14.4	100	6.0	10	57°	10.00	1.67	50	92.5

5.3 Grid Independent Study

A grid independence study was conducted to check whether flow regimes changes with the grid. Figure 5.2a shows the grid used in the parametric study for nozzle D and Figure 5.2b shows the coarser grid. Grid 'a' has about 17 million elements and grid 'b' has around 13 million elements. The total number of elements around the circumference of the mixing duct for the grid 'a' are 390 while for grid 'b' are 280. The Y$^+$ value for the grid 'a' is 0.72 while for grid 'b' is 0.92.
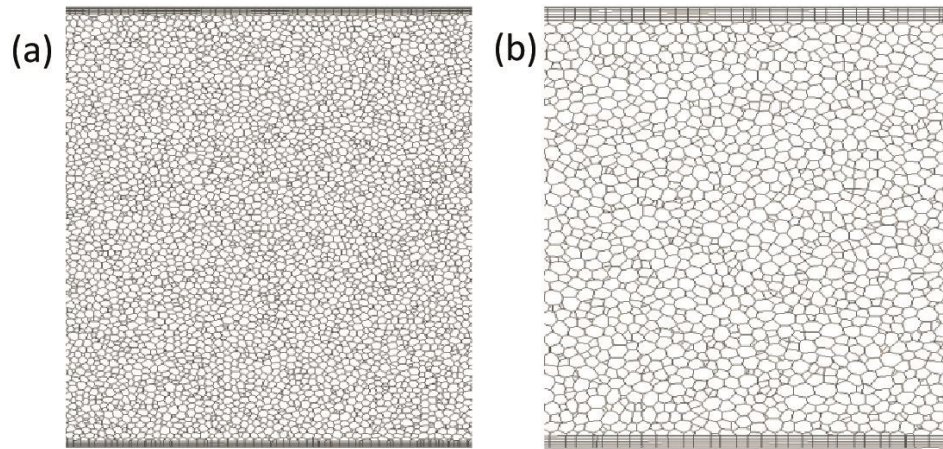
Figure 5.2 (a) grid used in the parametric study, (b) coarser grid.

Figure 5.3 shows contours of average volume fraction of water over one hundred thousand time steps. The time step size is $1 \times 10^{-8}s$. Figure 5.3 a & b depicts the average volume fraction for froth/churn-turbulent flow regime (GLR=0.01), Figure 5.3 c & d depicts the average volume fraction foe wispy-annular flow regime (GLR=0.1) and Figure 5.3 e & f depicts the average volume fraction of annular flow regime (GLR=0.3). The average volume fraction of all the three flow regimes is almost the same for coarser and dense grid.

Average Volume Fraction of Water

0.0　　　　　　0.3　　　　　　0.6　　　　　　1.0

(a) Average volume fraction for grid 'b' with GLR=0.01

(b) Average volume fraction for grid 'a' with GLR=0.01

(c) Average volume fraction for Grid 'b' with GLR= 0.1

(d) Average volume fraction for grid 'a' with GLR=0.1

(e) Average volume fraction for grid 'b' with GLR=0.3

(F) Average volume fraction for grid 'a' with GLR=0.3

Figure 5.3 Average volume fraction of water over one hundred thousand time steps (a & b) average volume fraction for froth/churn-turbulent flow regime, (c & d) average volume fraction for wispy-annular flow regime and (e & f) average volume fraction for annular flow.

41

5.4 Results and Discussion

Figure 5.4a shows contours of the volume fraction of air and water. At first it could be seen that the gas-liquid flow is annular, with the liquid film formed on the inner wall of the mixing duct. As the high speed gas jet impinges on the liquid jet, it creates disturbance on the surface of the liquid column; leading to creation of wavy structure in the liquid column/film. This may lead to inception of the primary breakup of the liquid jet within the nozzle. Figure 5.4b shows the contour of the velocity. Air jet accelerates as it expands from the gas port in to the mixing duct. It further accelerates as it bypasses the relatively slow moving liquid jet emanating from the liquid port. It then slightly decelerates while aligning with the liquid film before it rapidly accelerates towards the exit of the nozzle. Figure 5.4c is the contour of the pressure. The higher pressure around the area of air impingement on the liquid column is due to the increase in static pressure because of dynamic pressure of the air jet. The liquid film formed just downstream of the gas port (Figure 5.4a) in the mixing duct is because of the recirculation of the air due to its expansion from the gas port into the mixing duct. The expansion of the air is limited by the higher pressure of the liquid jet (Figure 5.4c). This leads to recirculation of the air in the pre-mixing zone of the mixing duct. Figure 5.5a shows the recirculating velocity vectors in the recirculating zone. Figure 5.5b is the schematic illustration of the reverse flow and liquid film formation in the premixed zone. A portion of the water stream is flowed backward in the form of film towards the upstream by the recirculating air flow. When the reverse film flow meets the main air stream at the exit of the gas port, it disintegrates into droplets and flows downstream along the core, as illustrated in Figure 5.5b .Figure 5.4d shows the contour of the Mach number of the forming multi-phase flow. The speed of the sound is mu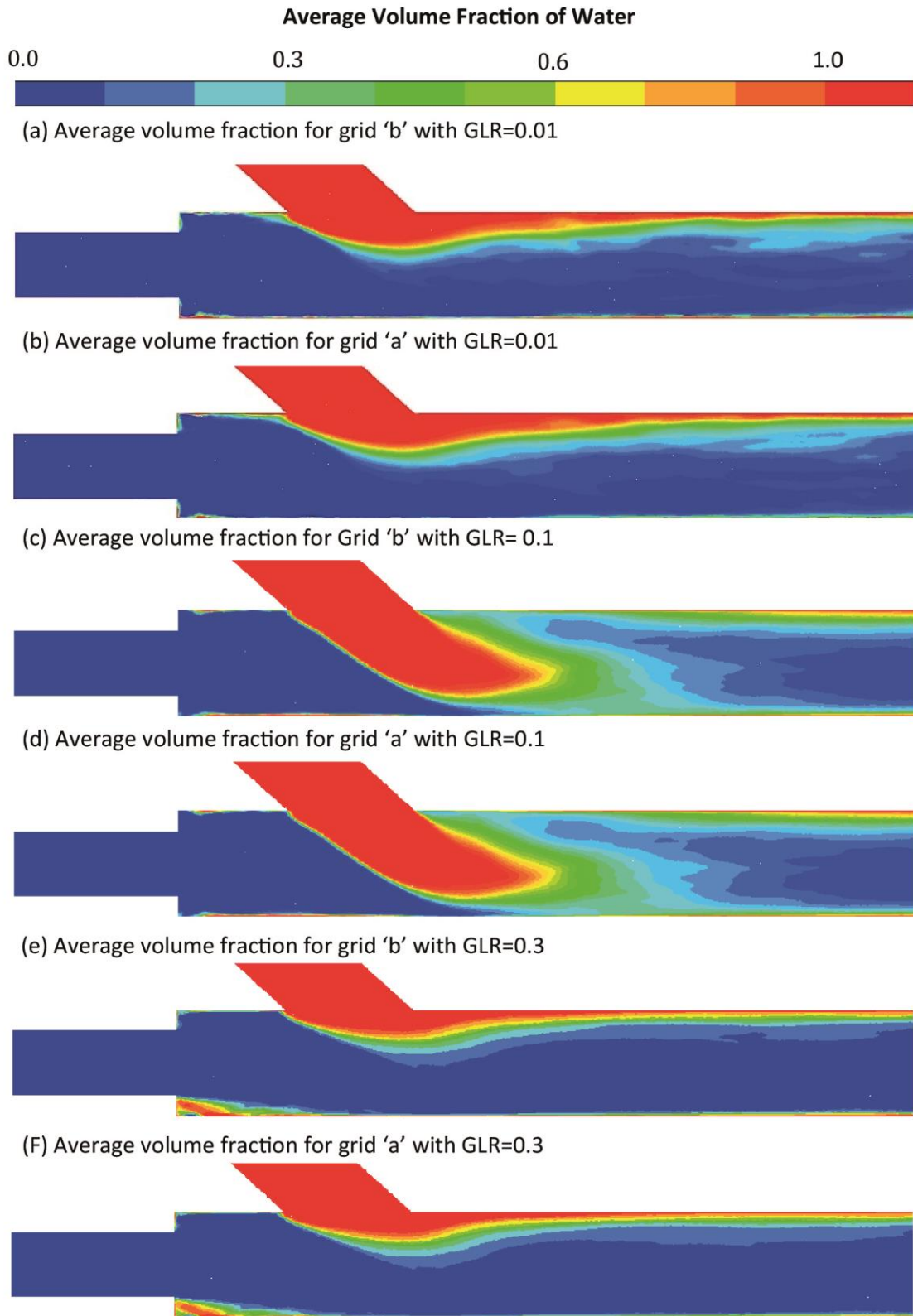ch lower in the gas-liquid mixture than in either pure liquid or gas component. For example, it is 1480 m/s in water and 340 m/s in air, but in air-water mixture it can fall to 20 m/s (McWilliam & Duggins, 1969). This process occurs because the two-phase system has the effective density of the liquid but the compressibility of the gas (Kieffer, 1977) (refer to appendix B for further details). In Figure 5.4d it can be seen that in the mixing duct, Mach numbers are higher at the gas liquid interface and around the exit of the nozzle. Although the instantaneous Mach numbers could be higher than one, there is no evidence of flow choking in the mixing duct. Pacifico & Yanagihara (Pacifico & Yanagihara, 2014) also reached to the same conclusion about gas-liquid multiphase flow in the mixing duct of Y-Jet atomizer.
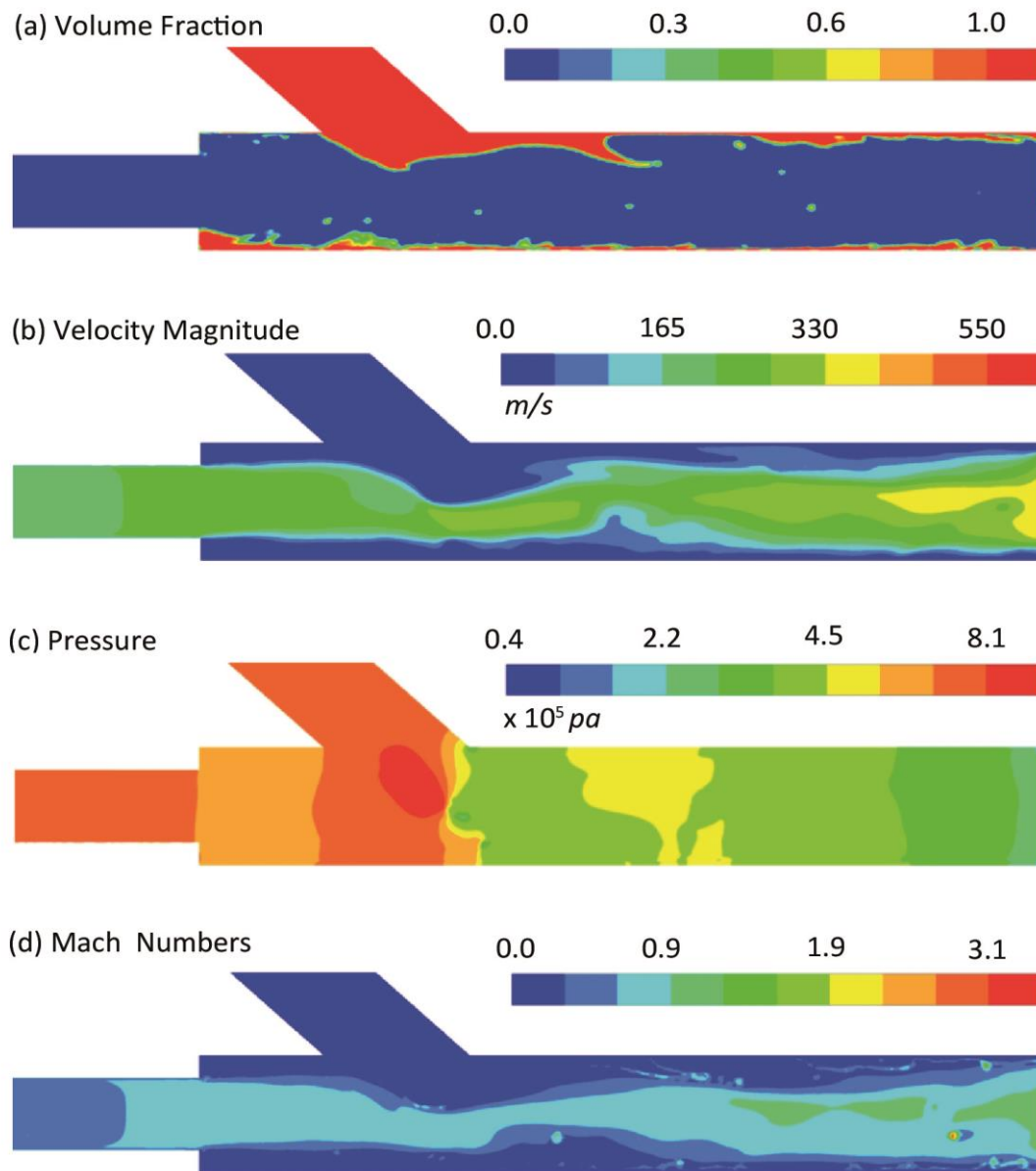
Figure 5.4 Flow field for the nozzle D with GLR =0.29 (a) volume fraction contours, (b) velocity contour, (c) pressure contour and (d) Mach number contour.

Figure 5.6 and Figure 5.7 depicts the plots of the ratios of mixing point pressure to air inlet pressure (P_m/P_a) and water inlet pressure to air inlet pressure (P_w/P_a) against the GLR ratios respectively. At first, in qualitative terms the results of all the nozzles are similar i.e. with increasing GLR both ratios decrease. Increase in GLR is attributed to either increase in air mass flow rate or decrease in water mass flow rate. This, in turn, induces the air flow momentum to have larger influence on the mixing process and particularly on mixing point pressure. On the other hand, water flow determines the back pressure for

the air jet expanding from the gas port into the mixing port. This behavior is inherent to any compressible flow expansion. It could be seen that rate of decrease of P_w/P_a ratio is higher than that of P_m/P_a ratio. This is because the water mass flow rate limits the expansion of the gas stream and hence leads to the conclusion that P_m among the others are controlled by the water inlet pressure.
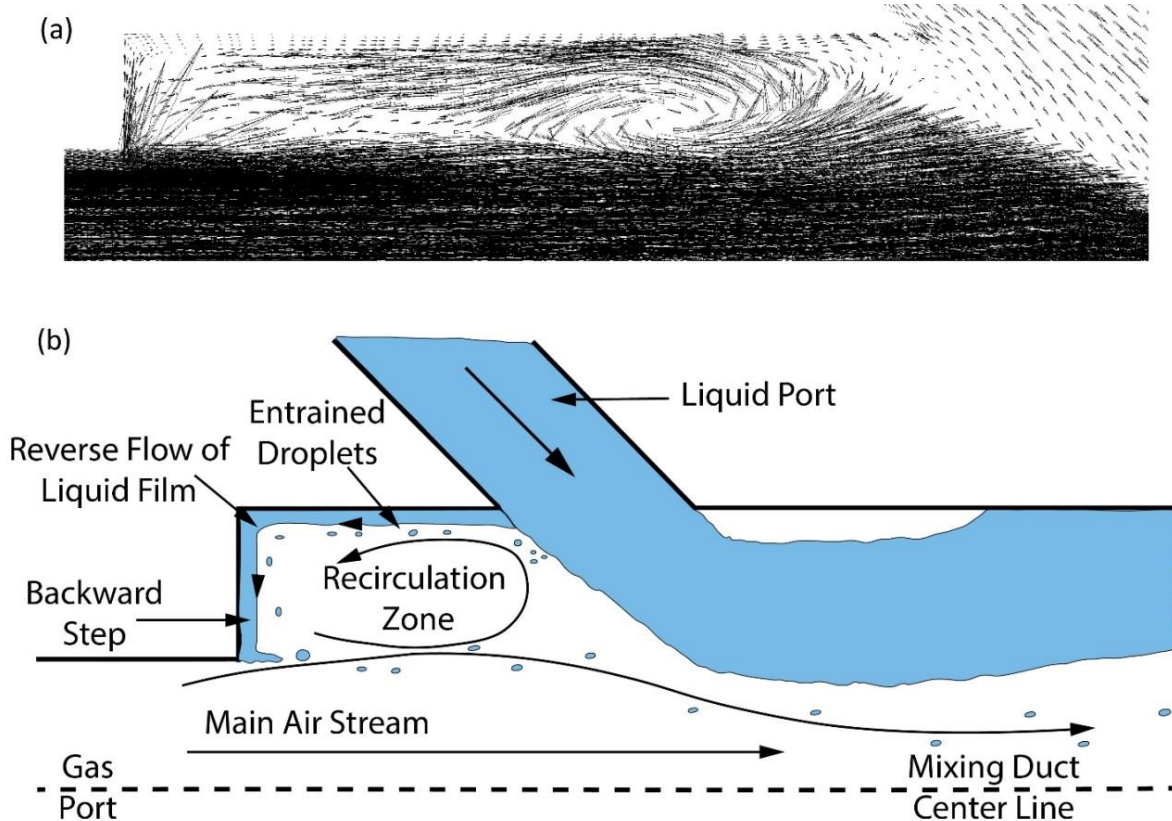
Figure 5.5 (a) recirculating velocity vectors in recirculation zone, (b) schematic illustration of recirculating air flow and reverse film formation.

It could be seen from the plots that except for GLR =0 .2, there is virtually no difference among the results obtained for the angle between the mixing port and the liquid port as the function of GLR (nozzle B, D and E). This concludes that the angle doesn't have significant effect on the mixing point pressure. Ferreira et al (Ferreria, et al., 2009) reached to the same conclusion for the effect of angle on the Sauter Mean Diameter (SMD) of the droplets produced by twin-fluid atomizer with the mixing chamber. This leads to the hypothesis that the mixing point pressure does plays a role in the performance of internally mixing twin-fluid atomizer. Regarding the influence of l_m/d_m ratio on the mixing point pressure (Nozzles B, F and G), it could be noticed that the mixing point pressure increases with the increasing

l_m/d_m ratio. It should be noted that d_m is constant for all the three nozzles; hence the mixing point pressure increases with increasing mixing port length. This behavior is explained due to the smoother drop of the pressure for the large values of l_m. Since the outlet pressure is the same for all the nozzles (i.e. atmospheric pressure), the nozzle with higher value of of l_m has higher P_m. Mullinger & Chigier (Mullinger & Chigier, 1974) reported that droplet size decreases for the nozzle with longer mixing port while in contrast Song and Lee (Song & Lee, 1994) reported that droplet size decreases with shorter mixing port length. This contradiction was latter clarified by Song and Lee (Song & Lee, 1996). They reported that for relatively small liquid mass flow rate and high gas flow rate, the droplets generated by the nozzle with shorter mixing port are generally smaller than the droplets generated by the nozzle with longer mixing port; whereas for relatively large liquid mass flow rate and smaller gas flow rate, the droplets produced by the nozzle with longer mixing port are comparable or even slightly smaller than the drops produced by nozzle with smaller mixing port length. This discrepancy could be explained with the work of Lefebrve (Lefebrve, 1992). At low liquid mass flow rate and high gas mass flow rate, for the nozzle with shorter mixing port, there is not enough time for the wavy structure to be formed in liquid core/film; thus the liquid and gas do not align while co-flowing. Hence, gas impinges at an angle on the liquid sheets outside the nozzle, leading to vigorous break up of liquid sheets into small fragments; this process was termed as Prompt Atomization. If one observe carefully the data points for nozzles F and G in the Figure 5.6, it can be seen that for the small values of GLR (say GLR<0.3) there is not much difference between P_m/P_a ratio for the nozzle with long mixing port (nozzle G) and the nozzle with short mixing port (nozzle F). For the values of GLR ≥ 0.3 this difference increases. Smaller values of GLR mean lower gas mass flow rate or relatively higher liquid flow rate and large value of GLR means vice versa. This difference in pressure drop coincides with the performance of the nozzles as observed by Song and Lee (Song & Lee, 1996). Finally, comparing the data points of the nozzle A, B and C, it is evident from the plot in Figure 5.6 that d_m/d_g ratio has the most significant effect on the mixing point pressure among all the geometrical parameters studied. The higher the value of d_m/d_g ratio, the higher is the value of the pressure reduction between the gas inlet pressure and mixing point pressure (nozzle C). Particularly in the range 0.01 < ALR < 0.4, the influence of d_m/d_g is more significant, indicating that the gas pressure drop in this range is more when the d_m/d_g ratio is incremented. Similarly, P_w/P_a has the same behavior as function of GLR as that of P_m/P_a for the geometrical parameters studied (Figure 5.7).
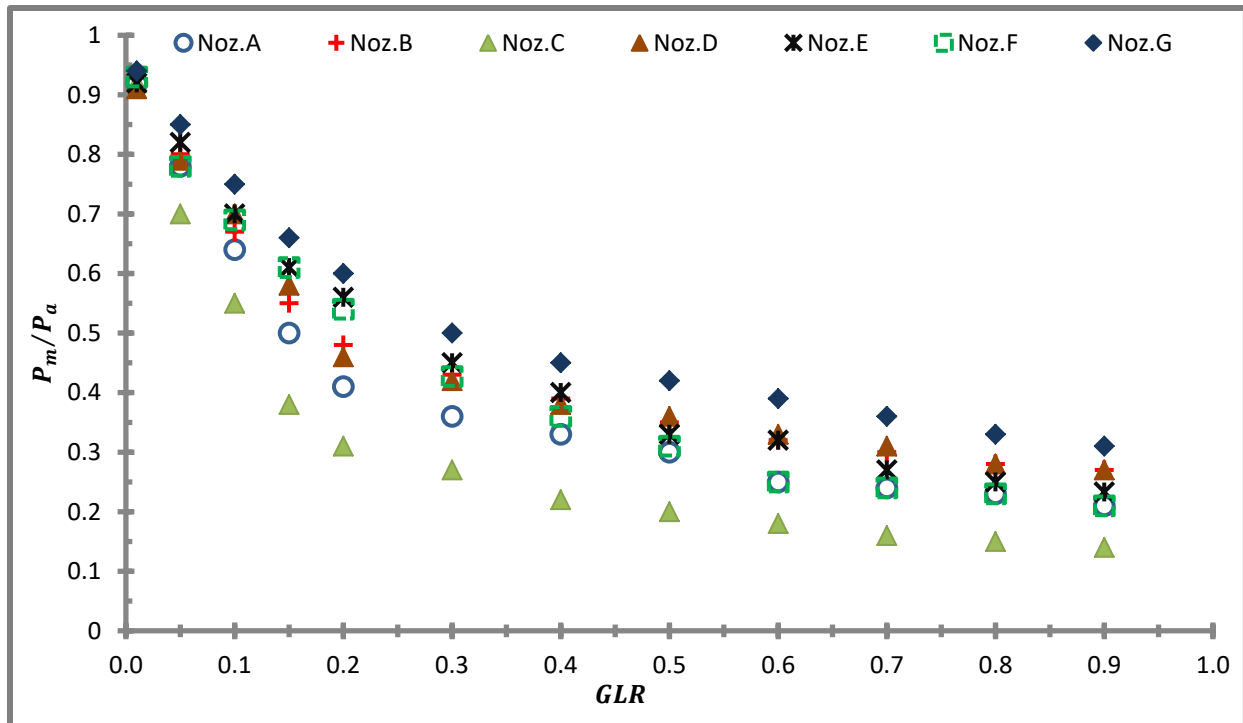
Figure 5.6 Plot of mixing point pressure to air inlet pressure ratio against gas to liquid mass flow rate ratio.
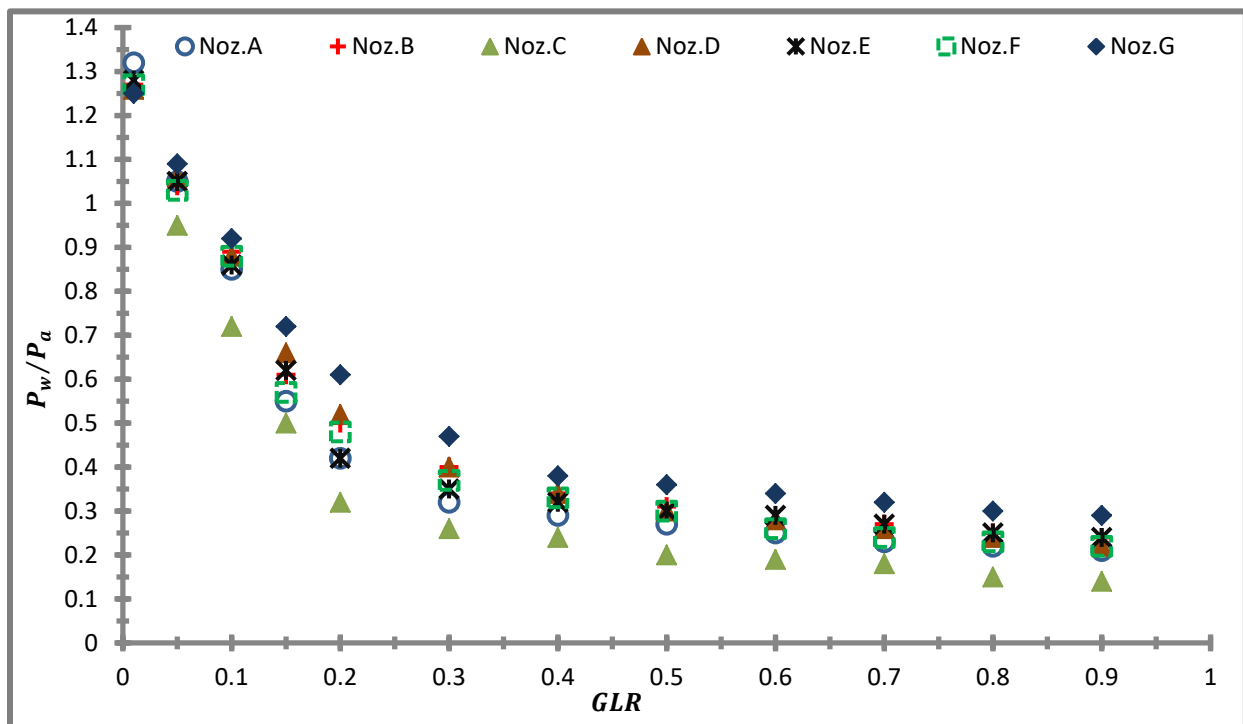
Figure 5.7 Plot of water inlet pressure to air inlet pressure ratio against gas to liquid mass flow rate ratio.
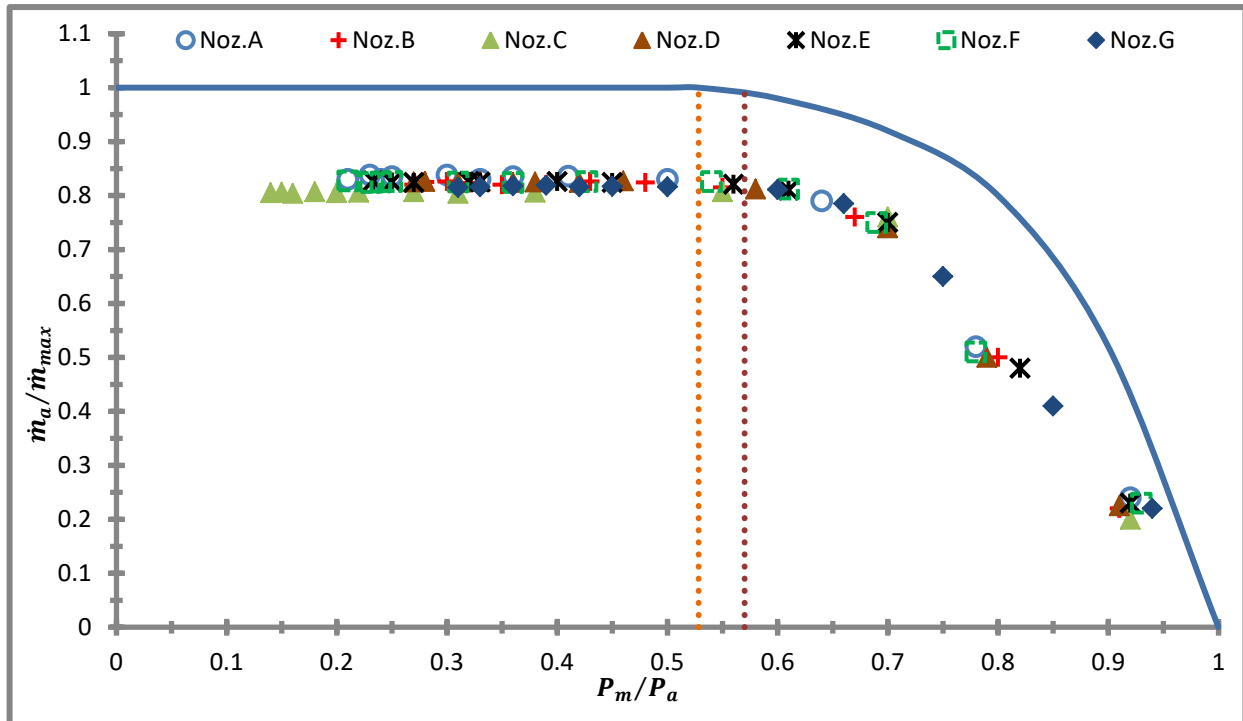
Figure 5.8 Plot of the ratio of air mass flow rate to maximum air mass flow rate through gas port against pressure ratio. The continuous blue line is the curve for isentropic flow through converging-diverging nozzle.

Figure 5.8 depicts the ratio of air mass flow rate to the maximum air mass flow rate (for Ma=1 at the throat between gas port and mixing port) as a function of pressure ratio (P_m/P_a). In the same figure, the curve for isentropic flow through converging–diverging nozzle is also plotted (continuous line). The flow in Y-jet atomizers from gas port to the mixing port is similar to the flow through converging diverging nozzle where d_g act as a nozzle throat and P_m (mixing point pressure) as the back pressure. The deviation of the data points from the isentropic prediction line is due to the irreversibility of the sudden expansion of the air and the presence of liquid around the mixing point. This behavior is also observed by Ferreira et al (Ferreria, et al., 2009) . The orange dashed line shows the pressure ratio ($P_m/P_a = 0.5283$) at which isentropic compressible flow through a converging-diverging nozzle is chocked. The red dashed line ($P_m/P_a = 0.565$) shows the deviation of the shocked region from the isentropic compressible flow. Ferreira et al (Ferreria, et al., 2009) explained that presence of the water in the mixing port restricts the air flow; the liquid mass flow rate changes the value of gas mass flow rate at which flow is chocked for the same geometric expansion (d_m/d_g). However, the chocked condition always occurs at the exit of the gas-port not down stream of this point (Pacifico & Yanagihara, 2014) & (Ferreria, et al., 2009). Farreira et al (Ferreria, et al., 2009) observed that smallest SMD (Sauter Mean

Diameter) are produced at chocked conditions. This is an important operational parameter for internally mixing twin-fluid atomizers. However, in the case of thermal power plants, when operating at chocked conditions, large amount of steam flow at high velocity is supplied to the combustion chamber. The intense interaction with the turbulence field induces high strain rates in the flame front leading to local flame extinction; this elongation of the flame might end up in a contact with boiler wall. In these cases, the reaction times become larger than the mixing time, leading to formation of soot (Warnatz, et al., 2001). Secondly, large amount of water introduced into the flame cools down the reaction zone leading to decrease in local temperature that might lead to flame extinction and prevent re-ignition of the mixture.

In order to compare all the parameters analyzed in Figure 5.6 and Figure 5.7 with the empirical correlations for P_m/P_a and P_w/P_a proposed by Pacifico & Yanagihara (Pacifico & Yanagihara, 2014), data points of all the nozzles A-G and the correlations of P_m/P_a and P_w/P_a are plotted in Figure 5.9 and Figure 5.10 respectively. These correlations are expressed in Eq. 2.3 and Eq. 2.4 in Chapter 2. They are valid for the range $0 \leq GLR \leq 1$; $3.5 \leq l_m/d_m \leq 10$; $1.67 \leq d_m/d_g \leq 2$; and 45°< θ <70°. In these correlations, θ must be in radians ($\pi/4 < \theta < 7\pi/18$). It can be seen in the Figures 5.9 & 5.10 that there is a good agreement between the proposed correlations and the current simulation results. An important operational parameter is the condition of critical gas flow. For the present numerical study it is P_m/P_a <0.565; this is obtained when $-0.675\theta^{-0.22}(l_m/d_m)^{-0.38}(d_m/d_g)^4 GLR^{0.87} > 1.05$.

Figure 5.11 shows the plot of the data points obtained from the simulations and the plot of the correlation ($P(z)/P_a$), Eq. 2.5, Chapter 2 proposed by Pacifico & Yanagihara (Pacifico & Yanagihara, 2014) for the pressure drop along the length of the mixing chamber. Numerical results agree well with the proposed correlation.

Another parameter used for the analysis of internally mixing twin-fluid Y-jet atomizer is the 'Liquid-to-Gas Momentum Ratio' (φ), Eq. 2.2, Chapter 2; this is the ratio of the momentum of the liquid jet going into the mixing port and momentum of the auxiliary fluid (air or steam). The correlation based on liquid-to-gas momentum ratio for the pressure drop along the length of the mixing chamber ($P(z)/P_a$), expressed in Eq. 2.6, Chapter 2, proposed by pacific & Yanagihara is plotted in Figure 5.12. Numerical data points are also plotted on the same figure. Again the results agree well with the proposed correlation.
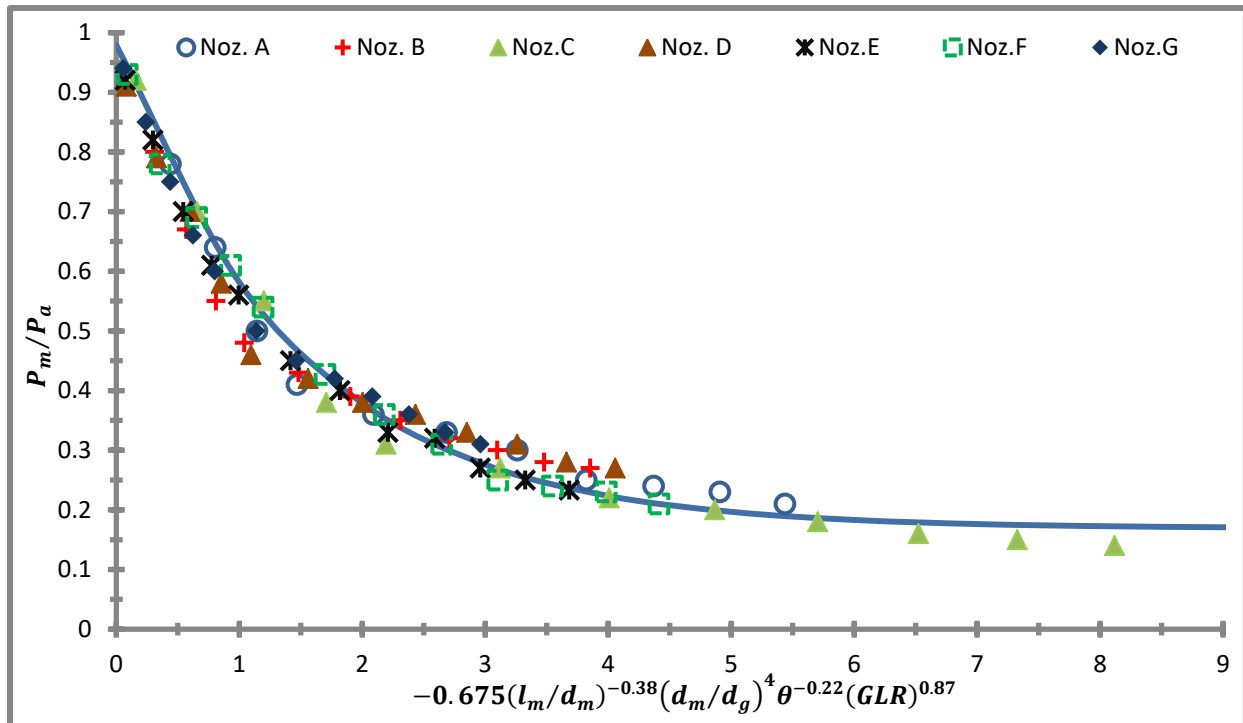
Figure 5.9 Comparison of numerical data points against empirical correlation (Eq. 2.3) for the mixing point pressure to the air inlet pressure ratio proposed by Pacifico & Yanagihara (Pacifico & Yanagihara, 2014).
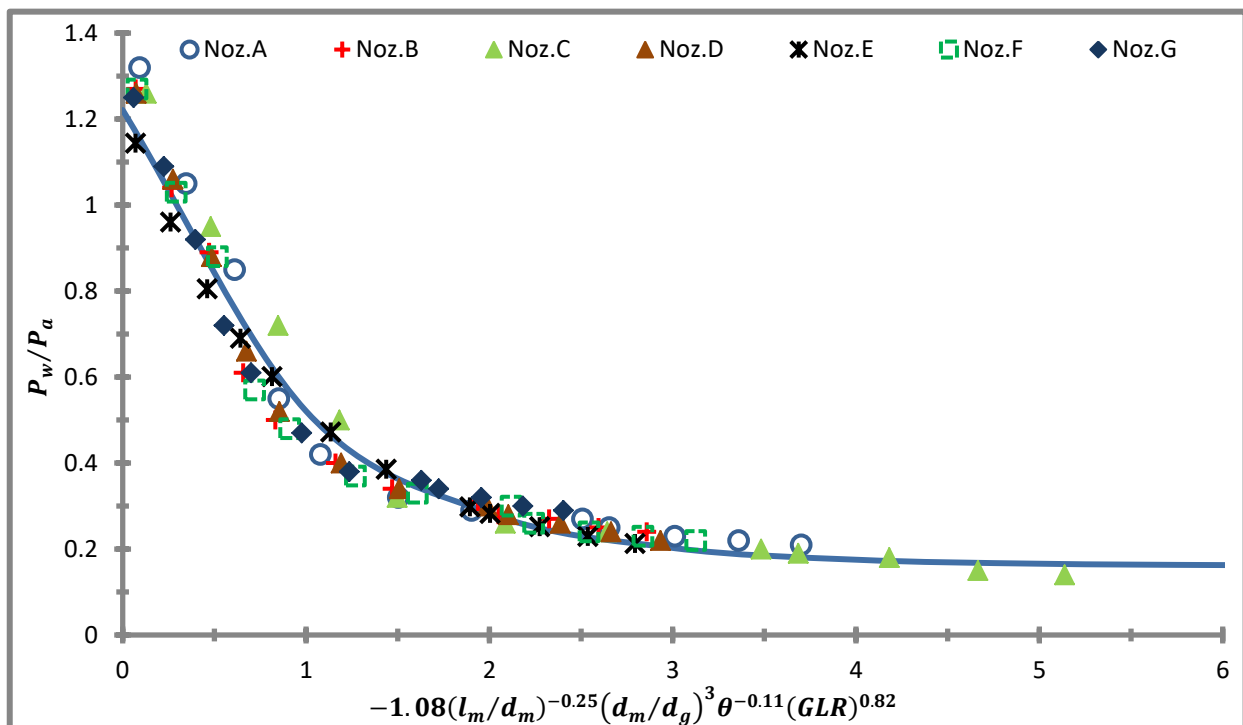
Figure 5.10 Comparison of numerical data points against empirical correlation (eq. 2.4) for the water inlet pressure to the air inlet pressure ratio proposed by Pacifico & Yanagihara (Pacifico & Yanagihara, 2014).
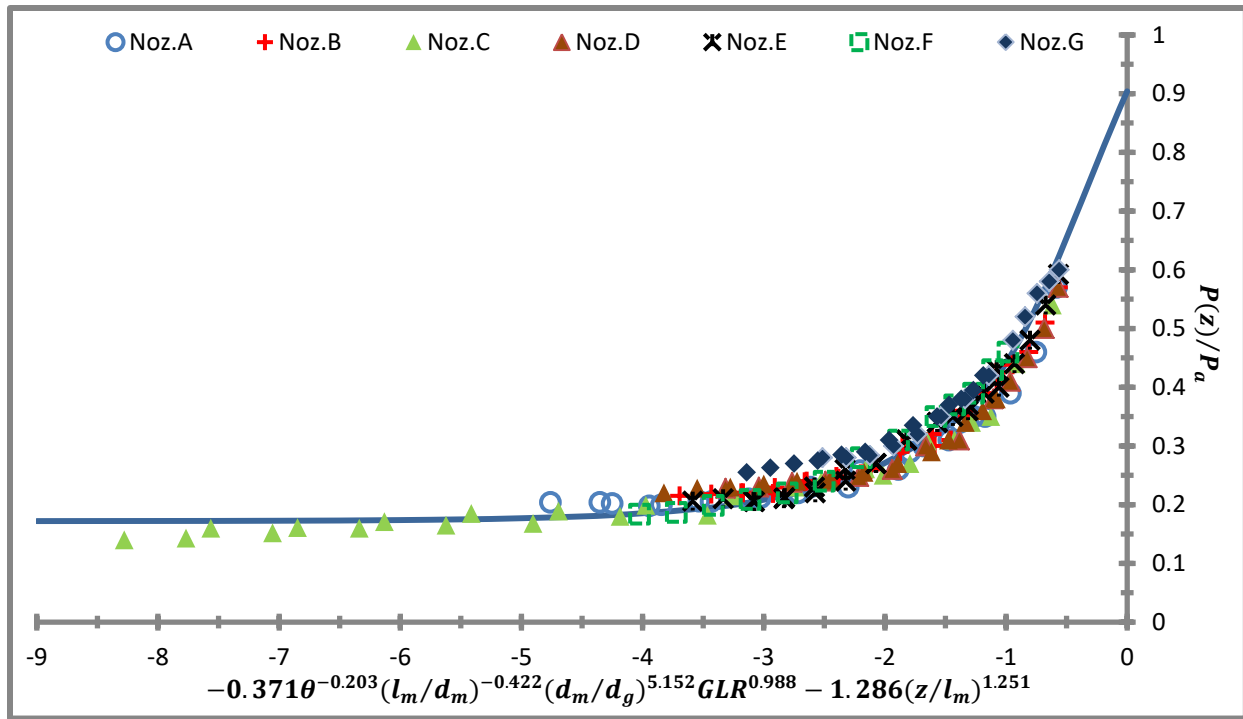
Figure 5.11 Comparison of numerical data points against the empirical correlation (Eq. 2.5) based on GLR for the pressure drop along the length of the mixing port proposed by Pacifico & Yanagihara (Pacifico & Yanagihara, 2014).

The x-axis is labeled:
$$-0.371\theta^{-0.203}(l_m/d_m)^{-0.422}(d_m/d_g)^{5.152}GLR^{0.988} - 1.286(z/l_m)^{1.251}$$
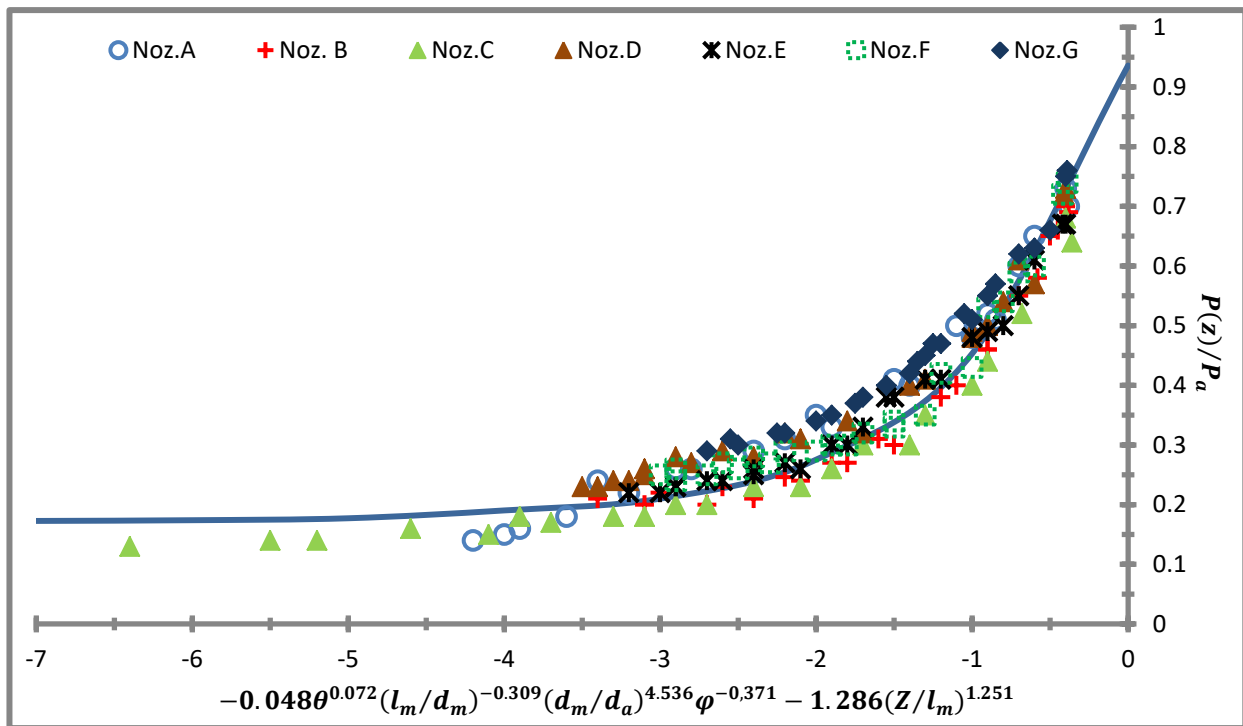
Figure 5.12 Comparison of numerical data points against the empirical correlation (Eq. 2.6) based on momentum ratio (φ) for the pressure drop along the length of the mixing port proposed by Pacifico & Yanagihara (Pacifico & Yanagihara, 2014).

The x-axis is labeled:
$$-0.048\theta^{0.072}(l_m/d_m)^{-0.309}(d_m/d_a)^{4.536}\varphi^{-0,371} - 1.286(Z/l_m)^{1.251}$$

Figure 5.13 shows the contours of the volume fraction for nozzle 'D,' for the three different GLR ratios. When the GLR ratio is low (0.01; Figure 5.13a), the flow seems to be somewhat transitional between froth/churn-turbulent flow and annular-wispy flow. As the GLR increases (0.1, Figure 5.13b) the flow is clearly in the wispy-annular regime with an annular liquid film surrounding the gas core comprising of dispersed droplets and ligaments. As the GLR increases further (0.3, Figure 5.13c), the flow is clearly in the annular flow regime, with a wavy annular film around and gaseous core. These changes in the flow patterns occurring upstream of the discharge orifice greatly affect the atomization and spray formation downstream of the nozzle exit. For instance, when the flow within the nozzle is churn-turbulent flow, the spray formed is not stable; whilst, if the flow pattern is annular, the nozzle operates as plain-jet air-blast atomizer, comprising a central core of high velocity gas surrounded by annular film of liquid. The relative velocity between the gas and liquid ensure good atomization.
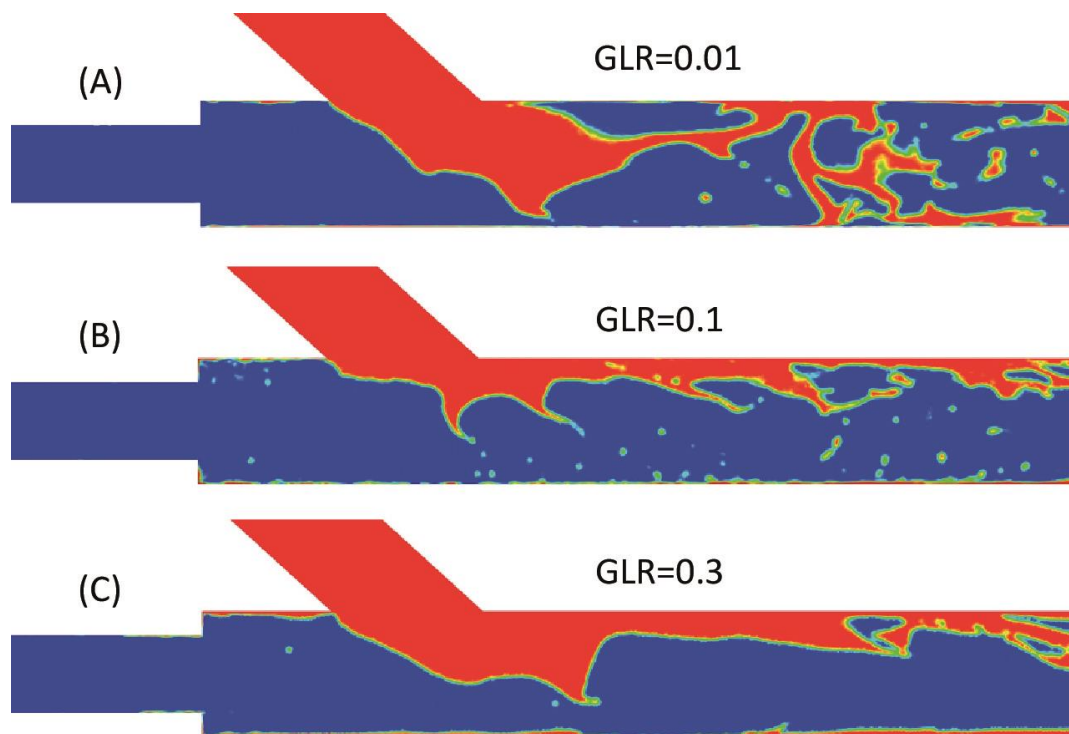
Figure 5.13 Contour of volume fraction of air-water multiphase flow at three different GLRs.

Figure 5.14 shows the Hewitt and Robert's multiphase flow map (Hewitt & Roberts, 1969). This map has been found to fit a reasonably large range of fluids and is of particular interest in the high mass flux region (Hawkes, et al., 2000). The coordinates represent the momentum fluxes; the ordinate represents

the air momentum flux while abscissa represents water momentum flux. J_w and J_a are superficial velocities of water and air respectively. The data points for all seven nozzles are also plotted on this map. It can be seen that the main flow patterns are annular and wispy annular. GLR ratio decreases with increase in water momentum flux; then according to this map, for small values of GLR, the wispy annular is the main flow pattern while for larger values of GLR, the annular flow is the main flow pattern. This result matches with the flow pattern observed within the nozzle (Figure 5.13b & 5.13c). However, there is small discrepancy between the results, at the lowest value of GLR in the study (0.01) flow seems to be transitional between the froth/churn turbulent flow and the wispy annular flow (Figure 5.13a), while, according to the map, it should be wispy-annular flow. Nevertheless, in industrial boilers the GLR ratio is usually between $0.1 < GLR < 0.3$. Flow is wispy annular at the lower end of this range and annular at the higher end of the range.
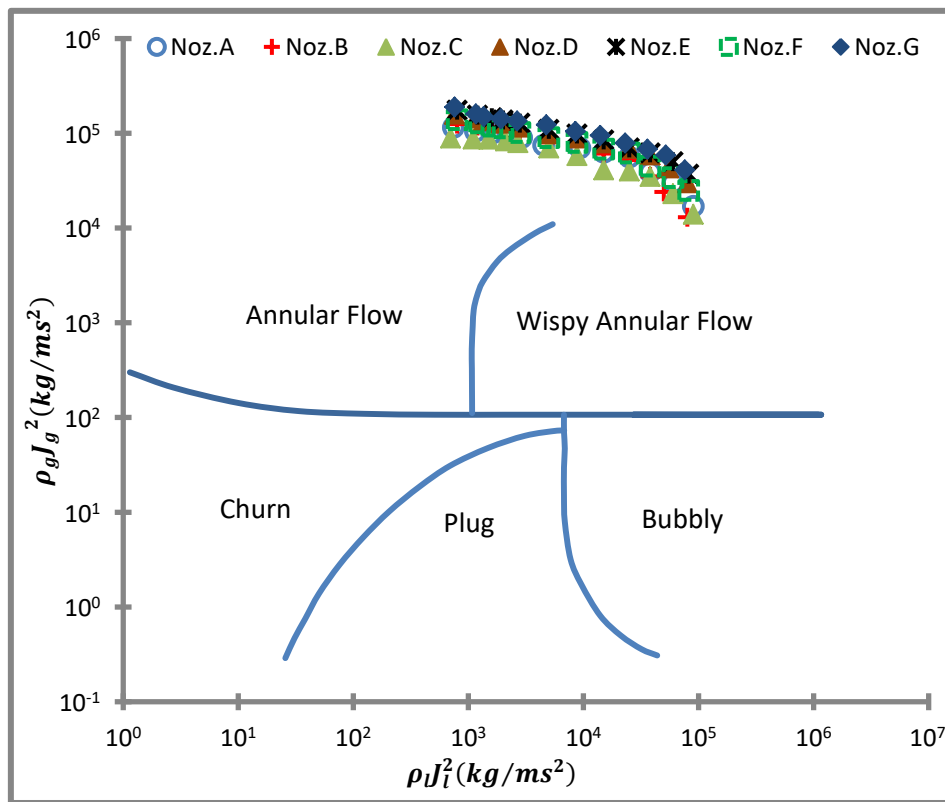
Figure 5.14 Data points plotted on vertical multiphase pipe flow regime map of Hewitt & Roberts (Hewitt & Roberts, 1969).

Figure 5.15 shows the flow pattern map provided by (Oshinnowo & Charles, 1974) for the vertical downward flow. In this figure, the ordinate is the square root of the air-liquid volumetric flow rate ratio, while the abscissa is the ratio of the two-phase Froude Number, Fr_{tp}, to the square root of A where,

$$Fr_{tp} = \frac{U_s^2}{g d_m} \qquad (5.1)$$

$$A = \frac{\mu_l'}{\left(\rho_l' \sigma'^3\right)^{0.25}} \qquad (5.2)$$

and J, the superficial velocity of the two phase flow is obtained as

$$J = \frac{Q_a + Q_l}{(\pi/4)d_m^2} \qquad (5.3)$$

It can be clearly seen that the results lie outside the flow regime established by the map. Nevertheless, one could easily speculate from the map that for the very low GLRs used in the study, the flow has to be froth or transition between froth and annular flow, while for higher values of GLR, the flow has to be annular; this result matches with the contours displayed in the Figure 5.13.
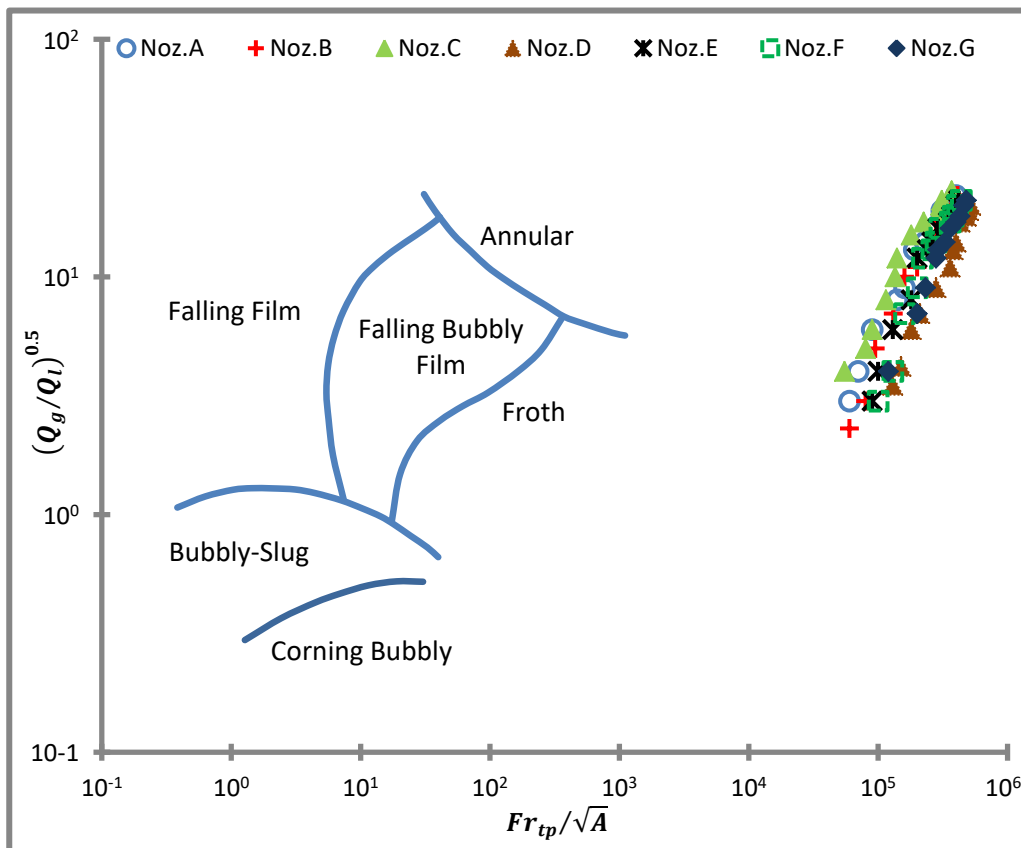
Figure 5.15 Data points plotted on vertical multiphase pipe flow regime map of Oshinnowo & Charles (Oshinnowo & Charles, 1974).

Chapter 6: Atomization Mechanism of Internally Mixing Twin-Fluid Y-Jet Atomizer

6.1 Introduction

In large oil-fired industrial boilers or thermal power plants internally mixing twin-fluid Y-jet atomizers are used to atomize the fuel. In this chapter the results of atomization mechanism of the gas-liquid multiphase flow through MHPS' internally mixing twin-fluid Y-jet atomizer are discussed. The multiphase flow through the internally mixing twin-fluid Y-jet atomizer is numerically modelled to determine the internal flow behavior and the subsequent atomization mechanism. It is the first numerical study to report the atomization mechanism of the internally mixing twin-fluid Y-jet atomizer. The influence of two dimensionless operating parameters, namely gas-to-liquid mass flow rate ratio and liquid-to-gas momentum ratio are compared; the latter is found to be more appropriate dimensionless parameter to describe the internal flow behavior and the atomization characteristics, as it defines to a large extend the liquid and gas distribution inside the atomizer, which then affects the near-nozzle atomization and the distribution of the formed ligaments and droplets. Based on flow visualization a detailed model of atomization mechanism of twin-fluid Y-jet atomizer is proposed. It is confirmed that the variation in the flow patterns within the mixing-port of the atomizer coincides with the variation of the spatial distribution of the spray drops. VOF-to-DPM transition mechanism is utilized along with dynamic solution-adaptive mesh refinement to predict the initial development and fragmentation of the gas-liquid interface through Volume-of-Fluid (VOF) formulations on a sufficiently fine mesh, while Discrete Phase Model (DPM) is used to predict the dispersed part of the spray on the coarser grid. It should be also mentioned that although more sophisticated atomization models exist in the literature for the

fragmentation of liquids, the applied model has been validated by our research group for other flow conditions, like for example the secondary break-up of liquid droplets (Stefanitsis, et al., 2019a), (Stefanitsis, et al., 2019b), (Strotos, et al., 2018), (Strotos, et al., 2016a), (Strotos, et al., 2016b) and (Strotos, et al., 2011). For the specific conditions simulated here, the complexity of the flow within the atomizer, it is unfortunate that quantitative experimental data for the atomizing spray that would be needed for quantitative validation of the applied computational models do not exist.

6.2 Test Case Simulated

Figure 6.1 depicts the geometry used in the simulations. The figure is not drawn according to scale. The working fluids are superheated steam and light fuel oil. The liquid port has diameter (d_l) 2.1 mm and length (l_l) 30 mm. The gas port has diameter (d_g) $1.6\ mm$ and length (l_g) $4\ mm$. Both the mixing port and the premixed zone has diameter $2.6\ mm$ and lengths $12.4\ mm$ and $5.6\ mm$ respectively. The angle between the fuel port and the mixing port is $42.5°$. Mass flow boundary conditions are employed at the inlets and pressure outlet boundary condition is applied at the outlet. The pressure and temperature conditions at the inlet of the fuel port are $20°C$ and 19 bars, and at the inlet of steam port are $210\ °C$ and 11 bars respectively. The density and kinematic viscosity of the light fuel oil are $0.93\ kg/m^3$ and $4,1\ mm^2/s$ respectively, while steam is modeled as ideal gas. The condition at the outlet of simulation zone is air at 1 bar and room temperature. The Sauter mean diameters (SMD) of the droplets are measured on each 3 mm slot on the plane A along the Y axis as shown in Figure 6.1. Plane A is located at the distance of 32 mm from the nozzle orifice. This distance is chosen on the basis of computational affordability. The geometry is meshed in ANSYS Meshing with polyhedral grid. Dynamic solution-adaptive mesh refinement in ANSYS Fluent is used to dynamically adapt the mesh at the gas-liquid interface in the VOF simulations through polyhedral unstructured mesh adaption (PUMA) method. This adaptation travels with the gas-liquid interface and the number of cells changes with the flow, once liquid lumps are converted into the DPM particles; coarser grid is used to track the particles. This method significantly reduces the mesh count. Three levels of dynamic mesh refinement are used while the minimum cell volume is set to the order of $10^{-16}\ m^3$. The minimum cell volume is chosen based on the droplet size distribution to avoid over-refinement of the grid in order to run the simulations more efficiently. Figure 6.2 shows an instantaneous picture of numerical grid; it can be seen that the mesh is refined around gas-liquid interface. Mass flow inlet boundary conditions are used for the inlets and

pressure outlet boundary condition is used for the outlet. In the first set of the simulations the mass flow rate of the steam is kept constant at $0.00400 \ kg/s$ while the mass flow rate of fuel oil is varied from $0.1329 \ kg/s$ to $0.38 kg/s$; the corresponding values of gas-to-liquid mass flow rate ratios are from 0.01053 to 0.0301 respectively. In the second set of simulations, the mass flow rate of the steam is kept constant at $0.0005 \ kg/s$ while the mass flow rate of the fuel oil is varied from $0.005 \ kg/s$ to $0.0167 \ kg/s$; the corresponding gas-to-liquid mass flow rate ratios are from 0.03 to 0.1 respectively. The Reynold numbers for the flow conditions simulated are between 10,000 and 13,000. They are calculated from the following expression:

$$Re = \frac{\rho_{mix,m}V_r d_m}{\mu}$$

(6.1)

Here $\rho_{mix,M}$ is the average mixture density of the gas and liquid at the mixing point, V_r is the relative velocity between gas and liquid phase, and d_m is the mixing port diameter.

The asphericity value for the VOF-to-DPM transition mechanism is initially set to the value of 0.01. As the flow is developed in the mixing port of the atomizer, it is changed to the value of 2.5 to track the droplets and measure its SMD.
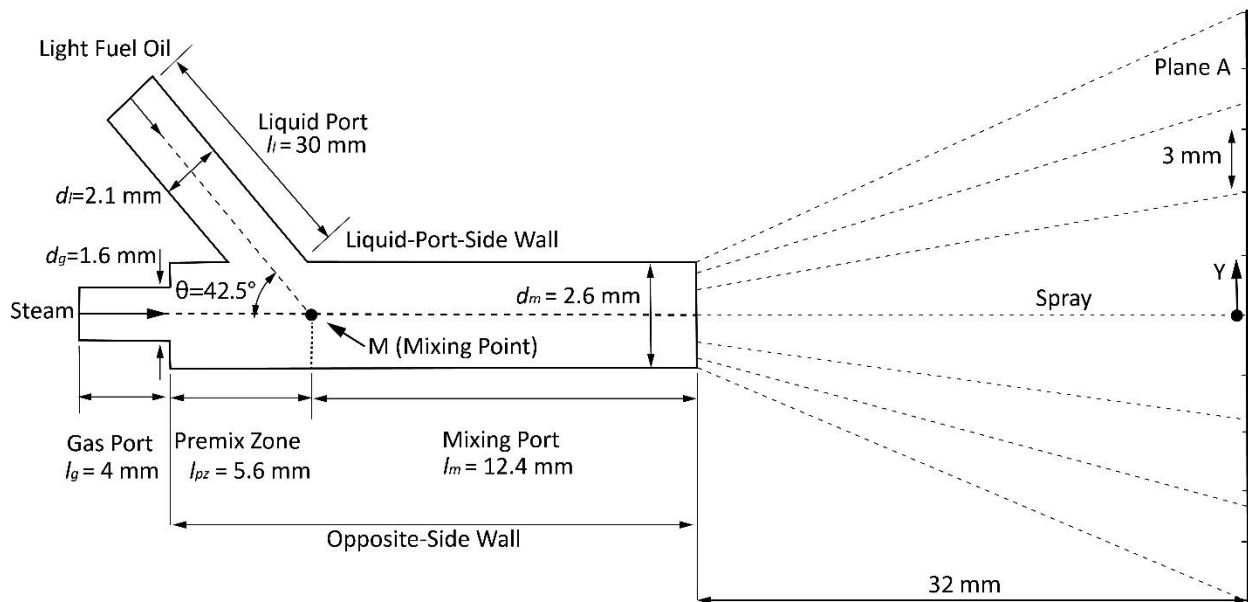
Figure 6.1 Geometry of twin-fluid Y-jet atomizer used in the simulations and schematic explanation of the subsequent spray formation.
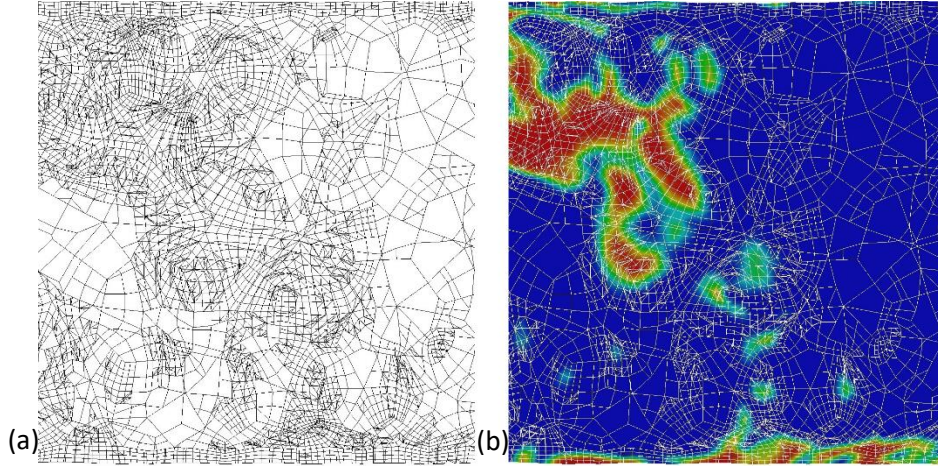
Figure 6.2 (a) Instantaneous grid (b) Instantaneous grid with the superimposed volume fraction of the Light Fuel Oil.

6.3 Grid Independent Study

A grid independence study was conducted to check whether the drop size distribution measured along the Y axis on the plane A change with the mesh. Two different dynamic solution-adaptive mesh refinements were used through PUMA method. Mesh "I" has three levels of dynamic mesh refinement and minimum cell volume of $10^{-16}\ m^3$, while Mesh "II" has three levels of dynamic mesh refinement and minimum cell volume of $10^{-17}\ m^3$. Drop size distribution for the liquid-to-gas momentum rations (φ) 3.2, 7.3 and 9.4 are shown in the Figure 6.3(a), Figure 6.3(b) and Figure 6.3(c) respectively. The drop size distribution for both the meshes is almost the same.

Figure 6.4 shows the contour of the average volume fraction of the light fuel oil within the nozzle over one hundred thousand time steps for the Mesh "I" and Mesh "II" for the liquid-to-gas momentum rations (φ) of 3.2, 7.3 and 9.4. The average volume fraction for both the meshes for the liquid-to-gas momentum ratios of 3.2 (Figure 6.4(a) & Figure 6.4(b)), 7.3 (Figure 6.4(c) & Figure 6.4(d)) and 9.4 (Figure 6.4(e) & Figure6.4(f)) are almost the same.
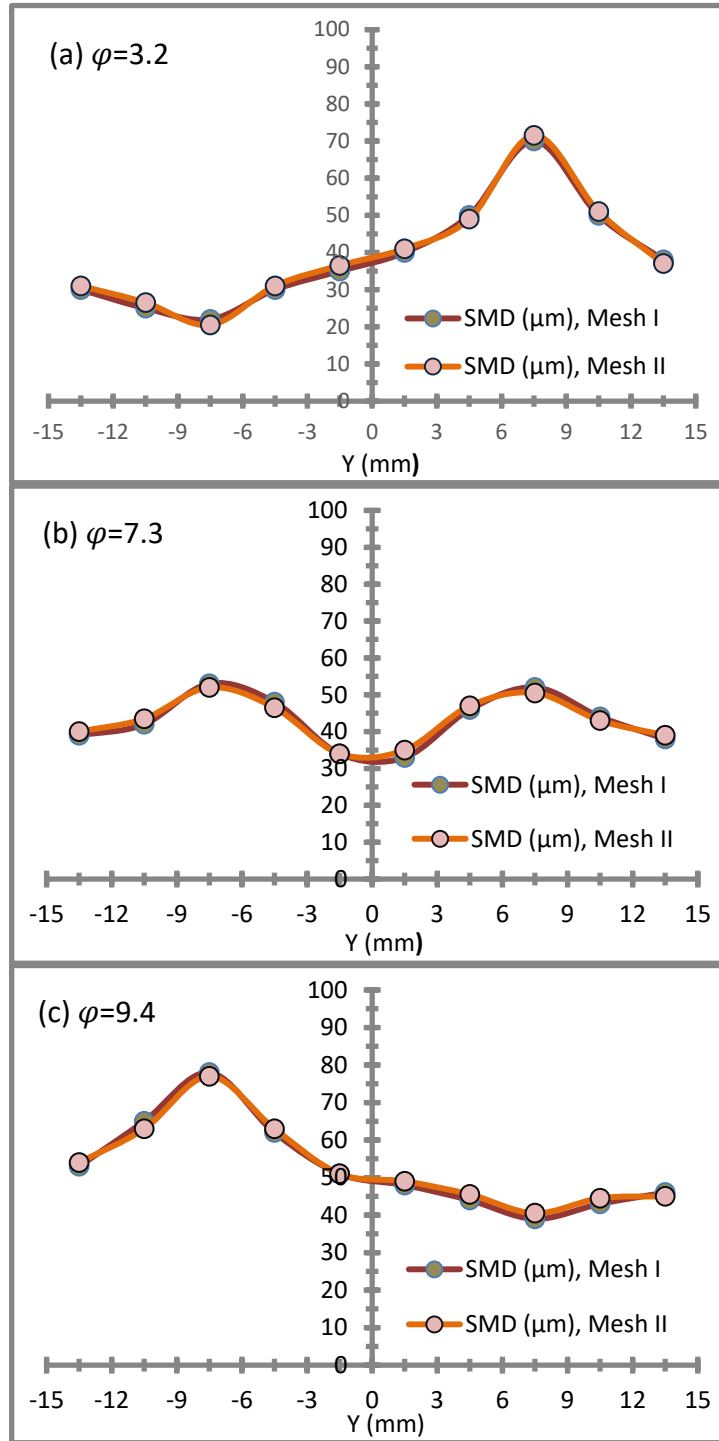
Figure 6.3 SMD drop size distribution for Mesh I and Mesh II for liquid-to-gas momentum ratios of (a) 3.2, (b) 7.3 and (c) 9.4.

Average Volume Fraction of Light Fuel
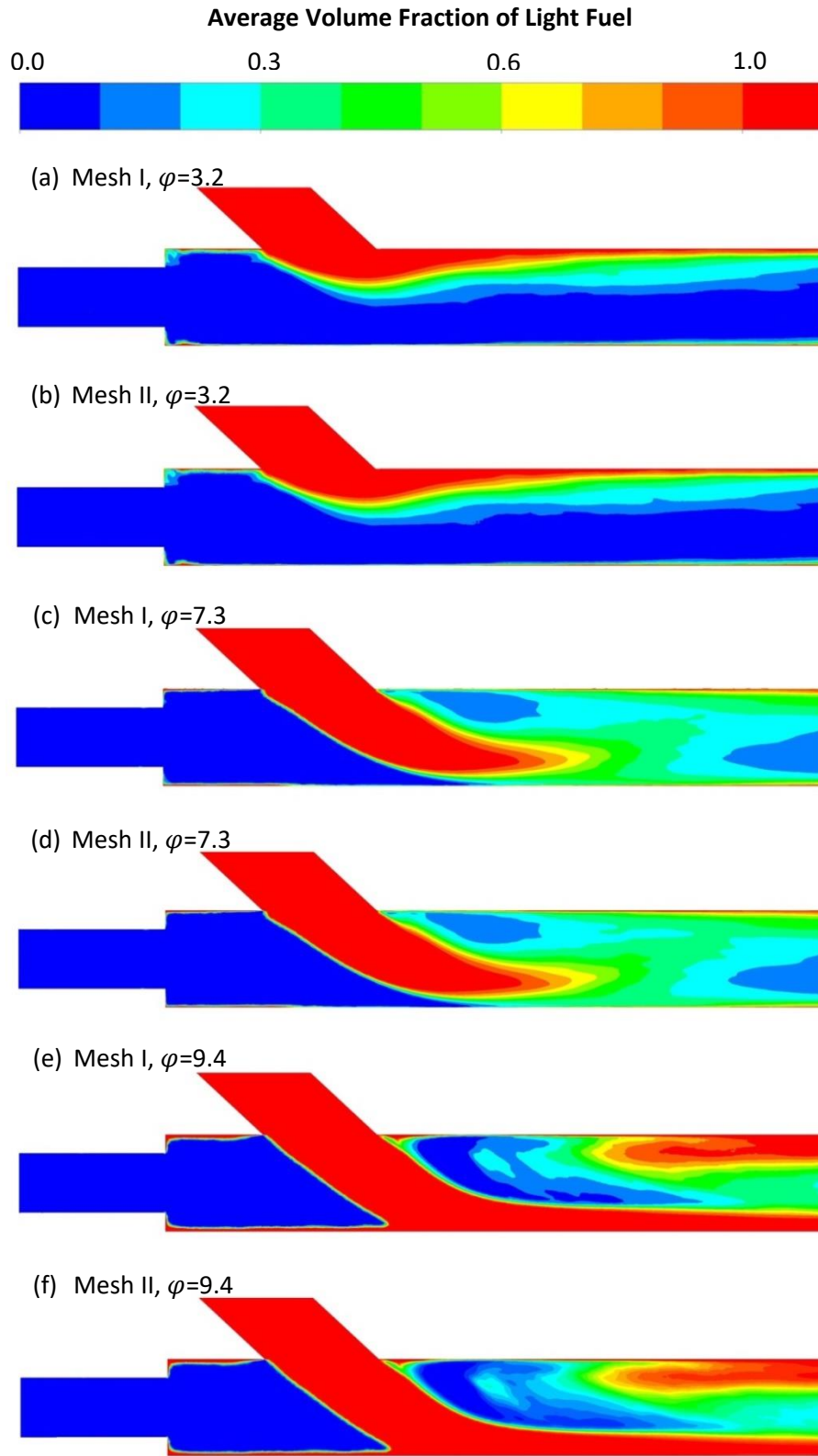
Figure 6.4 Average volume fraction of light fuel oil over one hundred thousand time steps for liquid-to-gas momentum ratios of 3.2 (a) Mesh I and (b) Mesh II, 7.3 (c) Mesh I and (d) Mesh II, and 9.4 (e) Mesh I and (f) Mesh II.

6.4 Asphericity Independent Study

Figure 6.5 shows the contour of the average volume fraction of the light fuel oil within the nozzle over one hundred thousand time steps for asphericity of 0.01 and 2.5 for the liquid-to-gas momentum ratio (φ) of 2.8. The average volume fraction for both the asphericities (Figure 6.5(a) & Figure 6.5(b)) are almost the same.

Average Volume Fraction of Light Fuel

0.0   0.3   0.6   1.0

(a) Asphericity 0.01
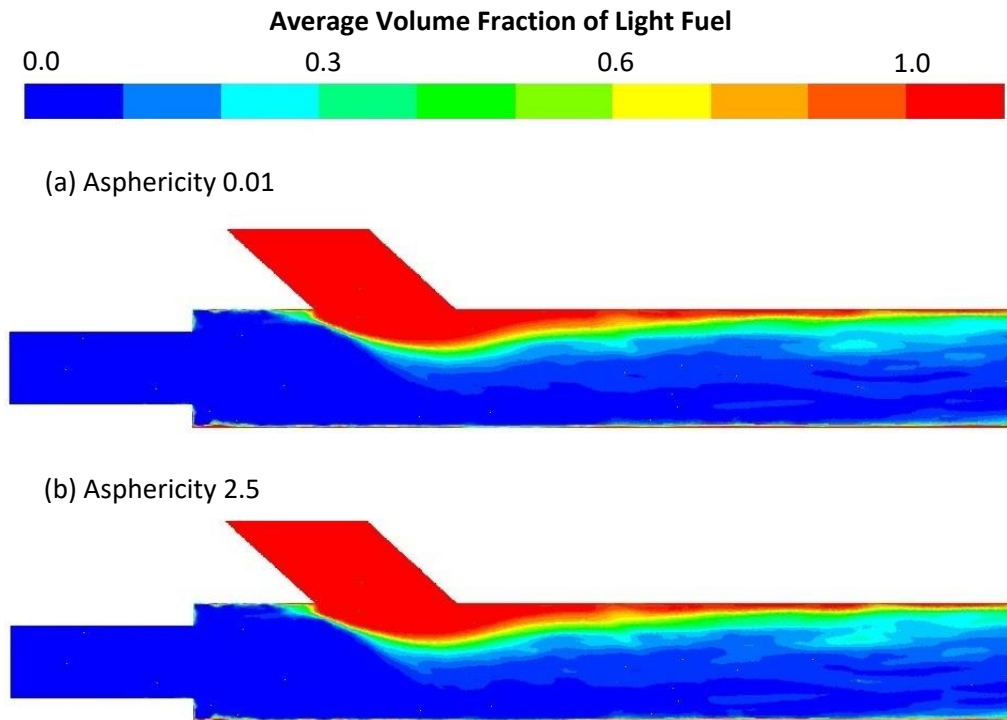
(b) Asphericity 2.5

Figure 6.5 Average volume fraction of light fuel oil over 1000 time steps for asphericity ratios of (a) 0.01, and (b) 2.5 for the liquid-to-gas momentum ratio of 2.8.

6.5 Results & Discussion

Visualization of the simulation results has been carried out to analyze the internal flow behavior within the mixing-port of the twin-fluid Y-jet atomizer. Figure 6.6 show the internal flow patterns within the mixing-port of atomizer for two different steam mass flow rates and various oil mass flow rates. For a reference, a schematic of the mixing port at the same scale is drawn at the top of Figure 6.6. The red colour depicts the volume fraction of fuel oil to be 1 while blue colour depicts the volume fraction of the fuel oil to be zero i.e. the volume fraction of the steam as 1. The instability of the liquid jet emanating from the liquid port into the mixing port is amplified by the impingement of high velocity gas stream;

leading to the creation of smaller liquid ligaments and sheets. This phenomenon could be explained by the shear action of the gas stream and by the wave lengths that grow on the surface of the liquid jet/column, which are affected by surface tension, aerodynamic and viscous forces (Dombrowski & Johns, 1963). The high relative velocity of the gas helps the dispersion of the liquid and delays or minimise the chances of droplet coalescence (Pacifico & Yanagihara, 2014).

At first, it can be realized from the contours in the Figure 6.6 that both $\dot{m}_l$ and $\dot{m}_g$ clearly influence the oil film formation within the mixing port. The amount of oil stream crossing the mixing port increases with a decrease of $\dot{m}_g$ and/or an increase of $\dot{m}_l$, and forms a thicker oil film at the opposite side wall. The internal flow pattern far downstream of the mixing point becomes an annular-mist flow with asymmetrical film thickness along the wall of the mixing-port, as characterized by Mullinger and Chigier (Mullinger & Chigier, 1974), Andreussi et al. (Andreussi, et al., 1994), (Andreussi, et al., 1992), Pacifico and Yanagihara (Pacifico & Yanagihara, 2014) Mlkvik et al. (Mlkvik, et al., 2015) and Nazeer et al. (Nazeer, et al., 2019). The rate of direct drop formation within the mixing port is also strongly dependent on both $\dot{m}_g$ and $\dot{m}_l$. That is, the number of drop increases with an increase in $\dot{m}_l$ and/or $\dot{m}_g$ (Song & Lee, 1996).

On the same figure, the values of the gas-to-liquid mass flow rate ratio ($\dot{m}_g / \dot{m}_l$) and the liquid-to-gas momentum ratio (φ) are also shown. φ is already defined in Eq. 2.2. These parameters are already adopted in the studies (Neya, et al., 1975), (De Michele, et al., 1991), (Andreussi, et al., 1992), (Song & Lee, 1994), (Andreussi, et al., 1994), (Pacifico & Yanagihara, 2014), (Mlkvik, et al., 2015) and (Nazeer, et al., 2019).

From Figure 6.6 one can point out that when the gas flow rates are different while $\dot{m}_g / \dot{m}_l$ is kept constant (see Figures 6.6a and 6.6i), the flow pattern appears to be much different. In fact, when liquid-to-gas momentum ratios are near to each other, for instance (6.6a and 6.6f) and (6.6h and 6.6C) flow development looks very similar. Thus, from the above observations, the liquid-to-gas momentum ratio (φ) seems to be a better dimensionless parameter to explain the internal flow pattern than the gas-to-liquid mass flow rate ratio. Song and Lee (Song & Lee, 1996) also reached to the conclusion that liquid-to-gas momentum ratio is a better parameter to describe the internal flow pattern.

Figure 6.7 helps to explain the variation in gas and liquid flow patterns within the mixing port of Y-jet nozzle based on the liquid-to-gas momentum ratio. When the liquid-to-gas momentum ratio is low (say $\varphi < 7$, Figures 6.6a, 6.6e, 6.6f and 6.6g), most of the liquid forms thick film at liquid-port-side wall of the mixing port. This is because the gas jet momentum dominates and liquid stream cannot penetrate into

61

the mixing-port easily. Due to this, the main stream of the gas tends to be deflected towards the opposite side wall by the liquid film and thus, a large recirculation appears in the premix zone. Hence, a portion of the liquid stream flows in a film shape toward the upstream by recirculating gas. For example the liquid film in the upper left corner of Figures 6.6b, 6.6f, 6.6g and 6.6i clearly indicates the reverse flow of the liquid film by strong recirculation of the gas. As the main gas stream at the exit of the gas port meets the reverse flow, it disintegrates in to small droplets and flows downstream along the core, as it can be seen in Figure 6.8. At the same time, as it can be seen in Figures 6.6a, 6.6e, 6.6f and 6.6g, droplets are also entrained from the main liquid film, flowing downstream.

		A-A'	$\dot{m}_g$ (kg/s)	$\dot{m}_l$ (kg/s)	$\dot{m}_g/\dot{m}_l$	φ
(a)			0.00400	0.13290	0.03010	4.6
(b)			0.00400	0.16613	0.02408	7.3
(c)			0.00400	0.19936	0.02010	8.1
(d)			0.00400	0.38000	0.01053	9.4
(e)			0.00050	0.00500	0.10000	3.2
(f)			0.00050	0.00900	0.05600	5.4

(g)			0.00050	0.01100	0.04545	6.8
(h)			0.00050	0.01300	0.03800	8.3
(i)			0.00050	0.01670	0.03000	10.7
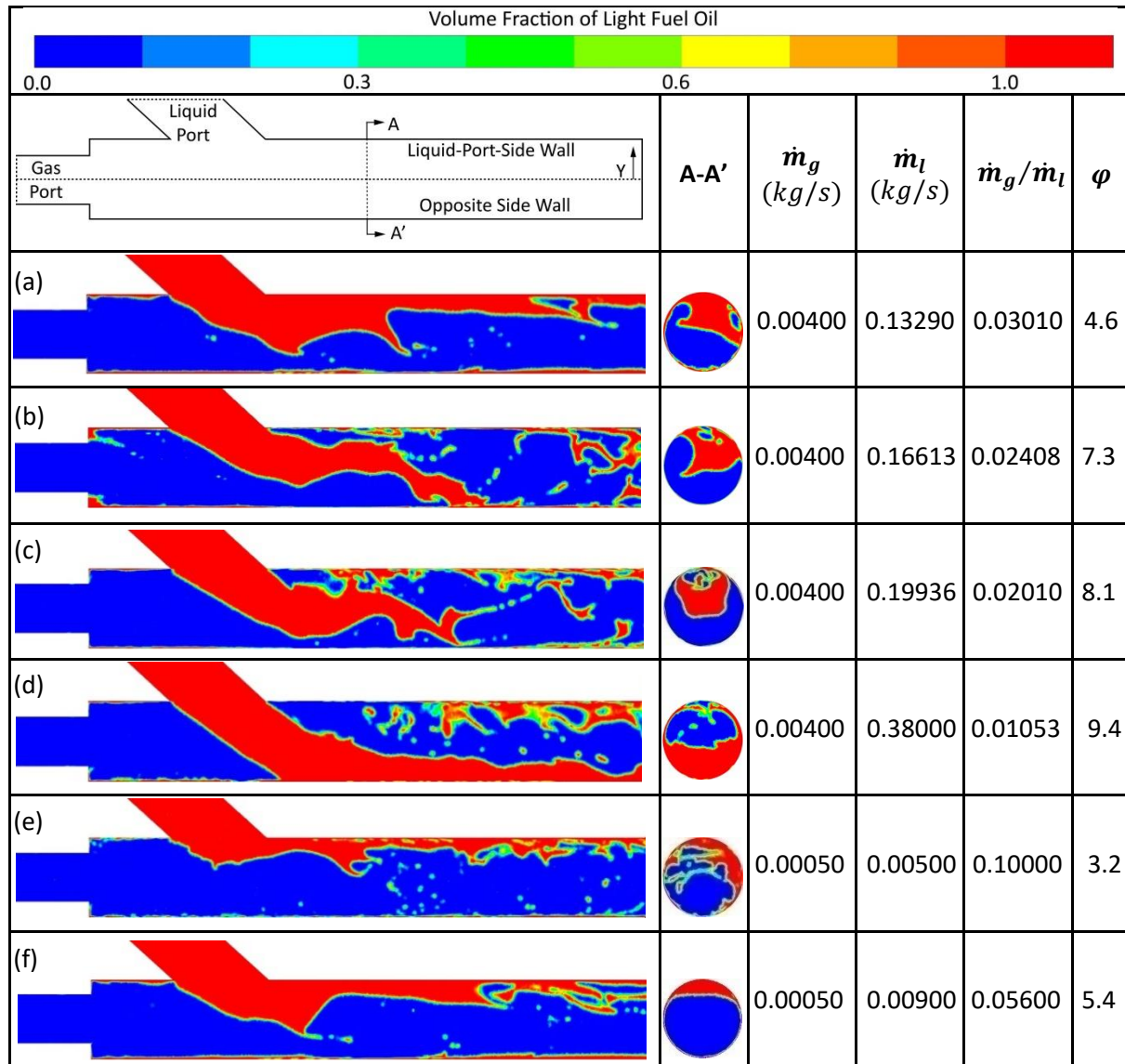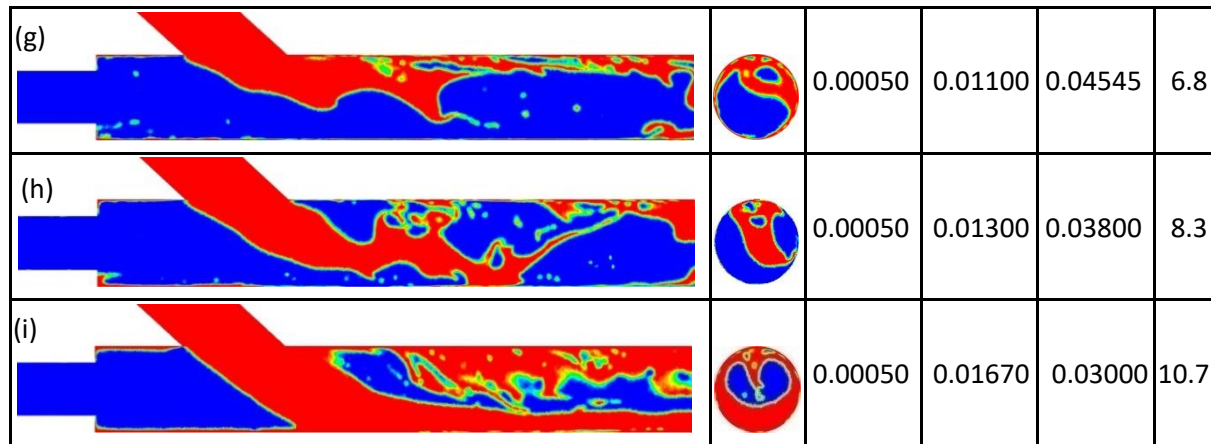
Figure 6.6 Internal flow pattern within the mixing port of internally mixing twin-fluid Y-jet atomizer at the flow time of 0.001 s for the liquid-to-gas momentum ratios of (a) 4.6, (b) 7.3, (c) 8.1, (d) 9.4, (e) 3.2, (f) 5.4, (g) 6.8, (h) 8.3 and (i) 10.7.
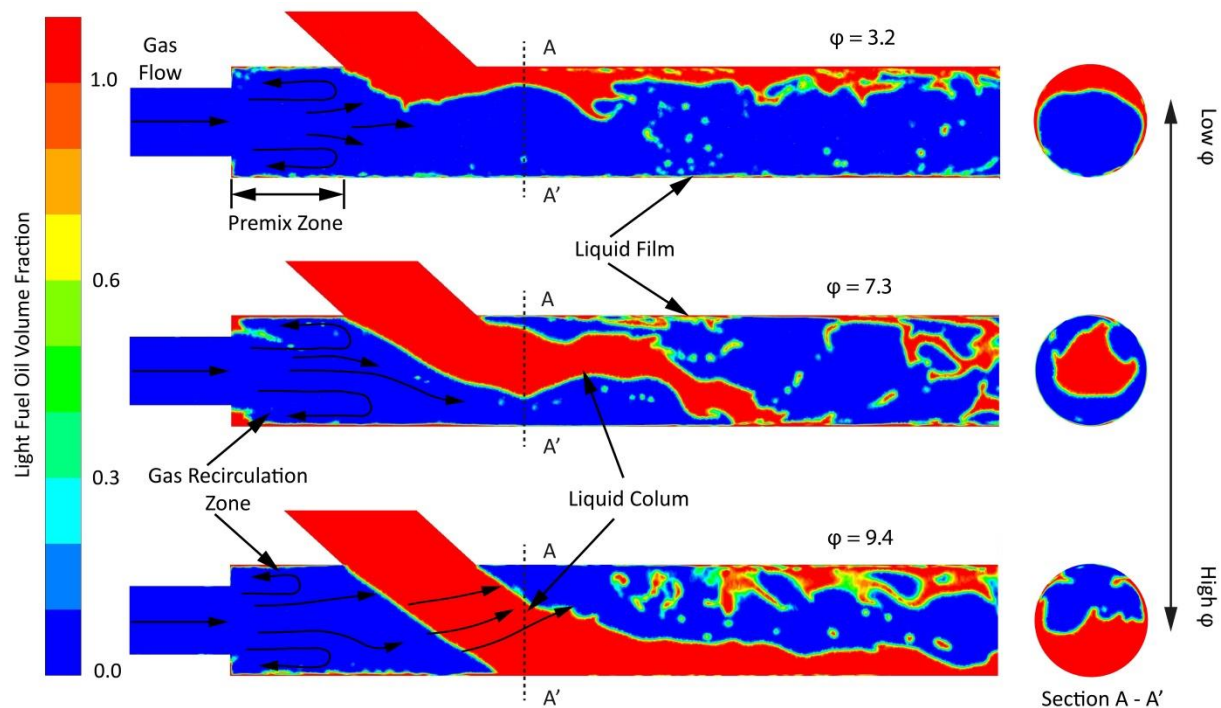
Figure 6.7 illustration of internal flow pattern based on liquid-to-gas momentum ratio.

As the liquid-to-gas momentum ratio increases further ($\varphi > 9$, Figures 6.6d and 6.6i), part of the liquid jet reaches the opposite wall and the liquid film thickness at both sides of the mixing port becomes similar in thickness. If the liquid-to-gas momentum ratio increases further, the liquid jet completely reaches the opposite side wall and the film thickness at the opposite side wall becomes thicker than the liquid-port-side wall, as can be seen in the Figure 6.6d. With this condition, the blockage effect becomes

more prominent because the gas stream has to flow around the liquid jet crossing the mixing point. Due to the high sheer of the gas flow, thin sheets of the liquid are extracted from the liquid jet around the mixing point (liquid-port-side wall Figures 6.6d and 6.6i). These sheets are further broken down into smaller droplets in the downstream flow. The quantity of these liquid sheet formations increases with the deeper penetration of the liquid jet or with greater gas flow rate.
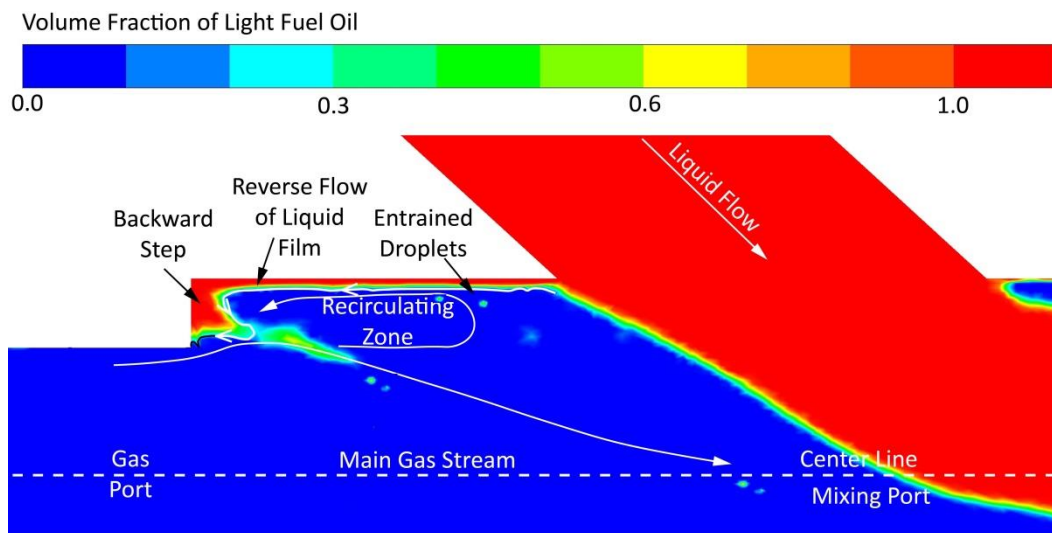
Figure 6.8 illustration of the recirculation in the premix zone of the internally mixing twin-fluid Y-jet atomizer.

Figure 6.10 shows the schematic diagram illustrating the atomization model in an internally mixing twin-fluid Y-jet atomizer. The concept is similar to that of song and Lee (Song & Lee, 1994), Mullinger and Chigier (Mullinger & Chigier, 1974) and Andreussi et al. (Andreussi, et al., 1992), with the main difference that internal atomization mechanism is subdivided into three parts in (Song & Lee, 1996) and divided into two parts in (Morsi & Alexander, 1972) and (Andreussi, et al., 1992) based on flow visualization. The first one is the "recirculation mode," donated by region A in Figure 6.10, which is characterized by the recirculation of a part of the gas stream in the premix zone of the atomizer. With increasing liquid-to-gas momentum ratio, the recirculation of the gas stream expanding from the gas port into mixing port increases, hence the drop formation by this mode increases. The second one is the "direct colliding mode." It is characterized by the impingement of high velocity gas stream on the liquid jet and generation of the droplets around the mixing-point and near the exit of liquid port. The drops generated by this mode also depend on the liquid-to-gas momentum ratio. The next region (region C in

Figure 6.10) is the "entrainment/deposition mode," which exhibits nonuniform circumferential film formation in the mixing-port for the widest range of liquid-to-gas momentum ratio. Drops here are generated due to the shearing action of the high speed gas on the liquid film. At the same time, within this zone, some of the drops generated by the recirculation mode and direct colliding mode coalesce and deposit on the liquid film. Thus, the mixing-port length plays a primary role in this annular flow zone. In other words, the longer the mixing-port, the higher are the chances of coalescence and deposition/entrainment of the drops, since the residence time becomes longer and interfacial area between the gas and the liquid film also increases. The distorted gas stream around the mixing-point is also straightened up along the length of the mixing-port in this region, and the flow direction of the gas stream with the longer mixing port becomes more parallel to the liquid film flow. The atomization by "liquid disintegration mode," denoted by region D in Figure 6.10, is also affected by the mixing-port length due to the relative motion between gas and liquid jet. If the atomizing fluid flows in parallel with the liquid sheet, the classical wavy mechanism dominates. As per this mechanism, liquid surfaces take on some form of instability that grows as waves. The most rapidly growing wave become detached from the leading edge of the liquid surface to form a ligament, that is subsequently fragmented into droplets. Thus size of the droplets is dependent on the diameter of the ligaments from which they are formed. These ligament diameters, in turn, are dependent on the liquid sheet thickness, its viscosity and gas density. On the other hand, if the length of the mixing port is not long enough, the gas stream does not co-aligns the liquid film and retains a normal component against the liquid sheet, the liquid sheet is shattered into droplets by prompt atomization, and drop size becomes less dependent on the sheet thickness. If the prompt atomization mechanism becomes dominant, the breakup length of the liquid film will be shorter and the spray angle will become larger.

Figure 6.9 shows the spray formation process of internally mixing twin-fluid Y-jet atomizer. The magenta colored blobs and ligaments depict the resolved liquid by the VOF method. Once the specified criteria of aspherecity are satisfied, the resolved liquid is turned into discrete droplets, as represented by the spherical particles in Figure 6.9. Figure 6.11 shows the Sauter Mean Diameter (SMD) drop size distribution for various liquid-to-gas momentum ratios measured on the plane A along the Y axis as indicated in Figure 6.1. The droplet size distribution is strongly affected by the internal flow pattern and the initial atomization within the mixing port of the nozzle, as explained earlier. That is, the small droplets at the center are forming from the core flow within the mixing port of the atomizer, whereas the larger droplets at both sides are forming from the annular liquid film present on the walls of the

mixing port. It can be also noticed that as the liquid-to-gas momentum ratio increases, the peak value of the Sauter Mean Diameter in the positive Y axis decreases, indicating that the liquid film thickness at the liquid-port-side wall of the mixing port decreases, due to easier penetration of the liquid column into the gas stream. When the liquid-to-gas momentum ratio is less than 5.4 (Figures 6.11a, 6.11b and 6.11c), the values of SMD in the negative Y axis changes slightly with the increasing liquid-to-gas momentum ratios. This is because the liquid column does not have enough momentum to reach the opposite side wall. However, as the liquid-to-gas momentum ratio increases further than that, the values of SMD in the negative Y axis become sufficiently large and the distribution becomes somewhat symmetrical (Figure 6.11d). If φ increases further, the momentum of the liquid column dominates and hence the values of SMD in the negative Y axis become larger than the values in positive Y axis; the curve again shows asymmetrical shapes. At extremely high values of liquid-to-gas momentum ratio (Figure 6.11h), a sudden decrease in the values of SMD in the positive Y axis is observed. This is due to the shear-induced breakup caused by the increased blockage effect (Figure 6.6i). These distributions agree well with the film thickness variation within the mixing port measured by Andreussi et al. (Andreussi, et al., 1994) and the drop size distribution measured by (Song & Lee, 1996). However, the formation of thin sheets around the mixing point at extremely high liquid-to-gas momentum ratios and the resulting sharp decrease in the values of SMD are not reported in the either of the aforementioned studies.
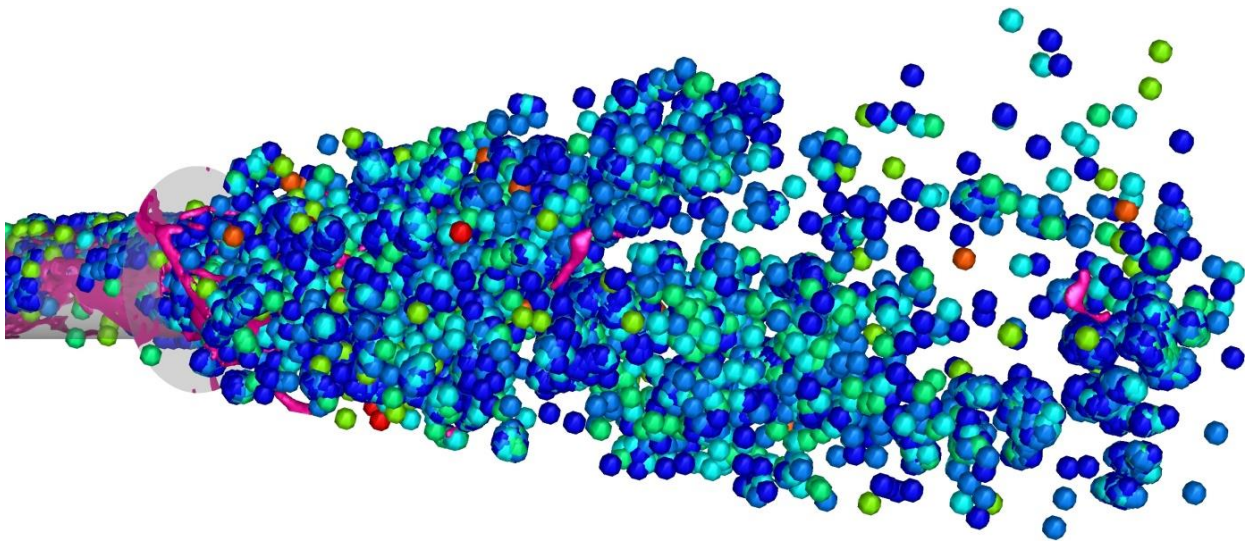
Figure 6.9 Spray formation by internally mixing twin-fluid Y-jet atomizer at the flow time of 0.0006 s for the liquid-to-gas momentum ratio of 7.3. The magenta colored blobs and ligaments represent the liquid resolved by VOF formulations and spherical particle represents the liquid droplets tracked by DPM model.
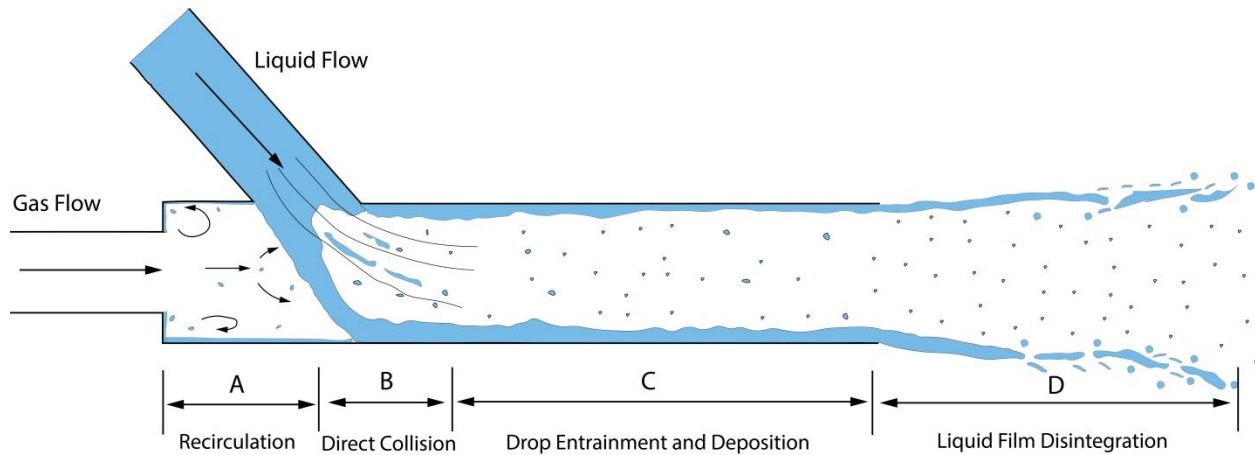
Region	Mode	Main Phenomena
A	Recirculation	• The reverse flow of the liquid film in the premix zone of the atomizer meets the main gas flow at the exit of the gas port, it disintegrates into small droplets.
B	Direct Collision	• Droplets generated by the impingement of the gas steam on the liquid jet
C	Drop entrainment and deposition	• Annular Liquid film is formed and the distorted gas stream is straightened up along the length of the mixing port • Droplets are generated by the shearing action of the gas flow and entrained into the gas core • Some of the droplets coalesce each other and deposit to the liquid film
D	Liquid film disintegration	• Liquid film disintegrates into ligaments first and then subsequently into large droplets outside the atomizer

Figure 6.10 Schematic illustration of the atomization model in the internally-mixing twin-fluid Y-jet atomizer.

Figure 6.12 shows the Sauter Mean Diameter (SMD) drop size distribution for Heavy Fuel Oil (HFO) as working fluid for the liquid-to-gas momentum (φ) ratio of 3.2, 7.3 and 9.6. Sauter Mean Diameter (SMD) drop size distribution for Light Fuel Oil (LFO) are also plotted for the comparison. It can be noticed that SMD distribution produced by Y-jet atomizer shows the same pattern for HFO and LFO as working fluids but it is clearly evident that the droplets generated by Y-Jet atomizer with Heavy Fuel Oil are far coarser than the droplets produced by Y-Jet Atomizer with the Light Fuel Oil. This confirms that Y-Jet atomizers are not suitable to be used with Heavy Fuel Oil. HFO has higher viscosity than the LFO. Viscosity dampens out the instabilities in the liquid jet and delays the atomization, hence Y-jet atomizers exhibits poor performance with HFO as a working fluid.
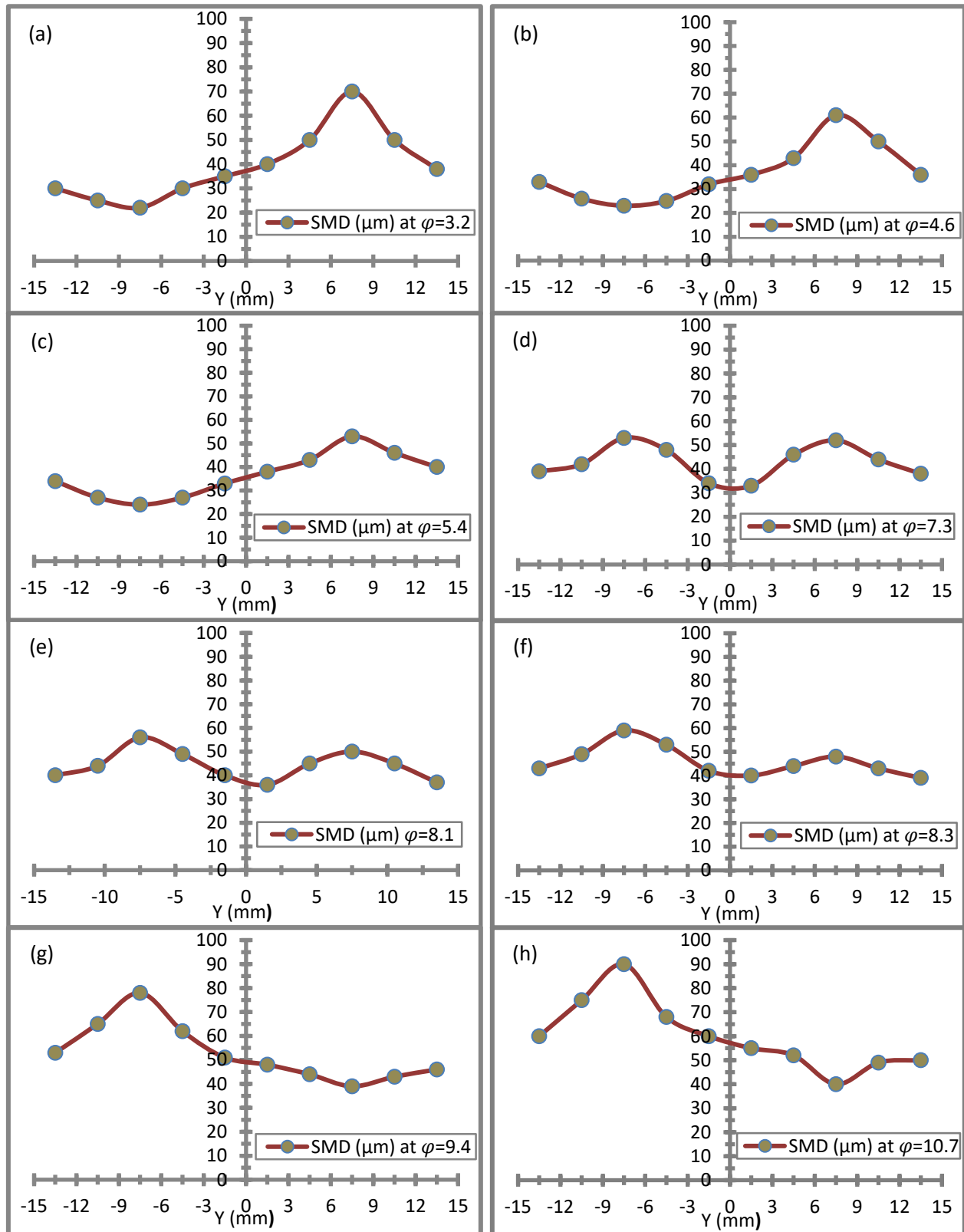
Figure 6.11 Sauter mean diameter drop size distribution for the liquid-to-gas momentum ratios of (a) 3.2, (b) 4.6, (c) 5.4, (d) 7.3, (e) 8.1, (f) 8.3, (g) 9.4 and (h) 10.7.
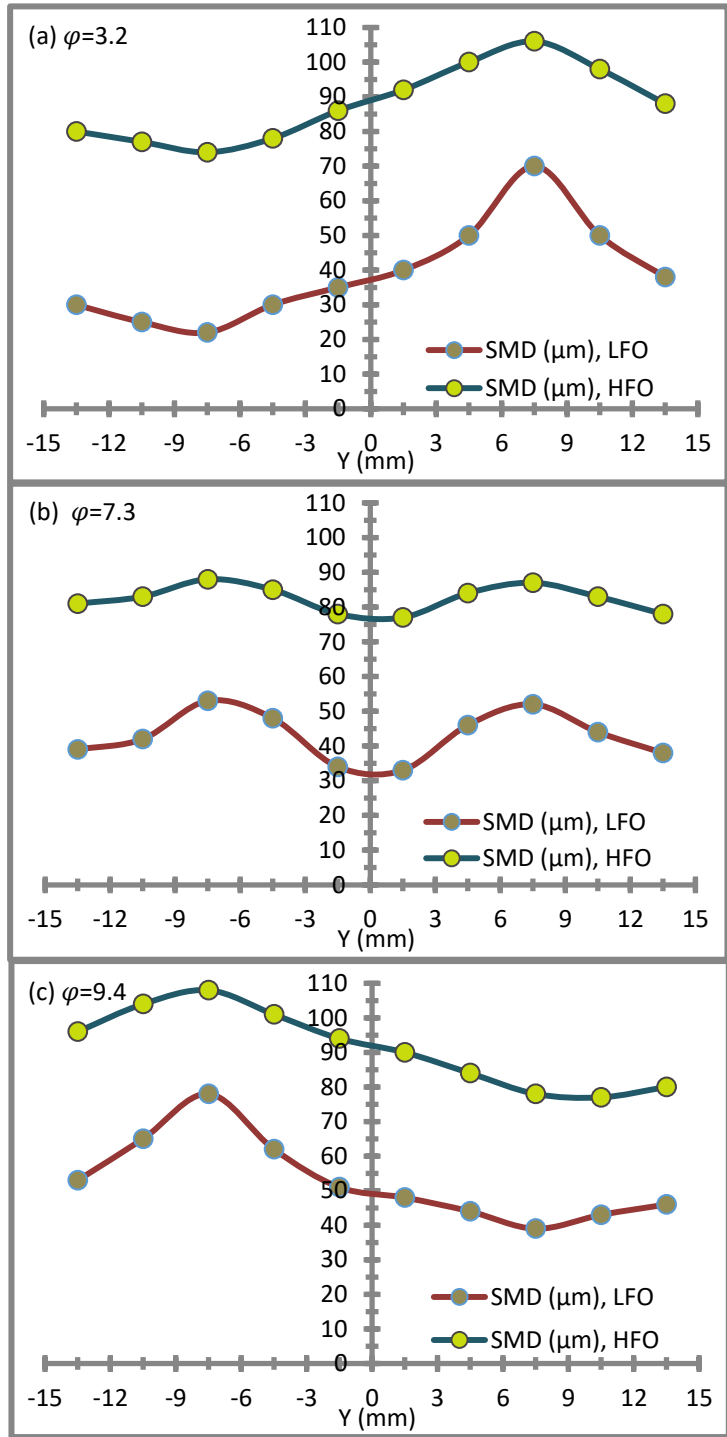
Figure 6.12 Sauter Mean Diameter distribution for light fuel oil and heavy fuel oil for the liquid-to-gas momentum ratios of (a) 3.2, (b) 7.3 and (c) 9.4.

Chapter 7: Conclusion and Future Work

7.1 Conclusion

Internally mixing twin-fluid Y-jet atomizer, which is used in industrial boilers, was under investigation in this thesis. Two detailed studies were conducted. In the first study a detailed parametric analysis to study the effect of operational and geometric parameters on the internal flow characteristics of twin-fluid Y-Jet atomizer has been carried out; seven atomizers with different geometrical parameters have been considered. Moreover, 11 cases for each atomizer with different GLR (gas-to-liquid mass flow rate) ratios have been simulated, giving a total of 77 cases. The results show that gas–liquid multiphase flow is annular flow for the vast majority of GLR ratios. The sudden expansion of gas jet from gas-port into the mixing duct is limited by higher pressure of the liquid jet emanating from the liquid port; this leads to recirculation of the air in the premixed zone of the nozzle, which, in turn, results to reverse film formation in the premixed zone. The numerical results obtained have been compared with empirical correlations of the pressure drop for twin-fluid Y-jet atomizer available in open literature and have been found to agree well with them. Moreover, the results show that the mixing point pressure is strongly dependent on the mixing port to airport diameter ratio, specifically in the rage $0.1 < (GLR) < 0.4$; the mixing port length moderately affects the mixing point pressure while the angle between mixing and liquid ports was found not to have an appreciable effect. The main flow regimes found under the studied operational conditions are annular and wispy annular flow. Different operational and geometric parameters identified in this study will be used by MHPS to optimize the design and operation of its atomizer.

In the second study the investigation on the atomization mechanism and atomization characteristics of MHPS' twin-fluid Y-jet atomizer was conducted under real power plant working conditions and working fluids. Two dimensionless parameters namely, gas-to-liquid mass flow rate ratio and the liquid-to-gas momentum ratio have been investigated; the latter is found to be a more appropriate dimensionless parameter to describe the flow characteristics. The variation in the internal flow pattern, characterized

by the penetration of the liquid column/jet into the gas core and the film flow within the mixing port could be effectively explained by the liquid-to-gas momentum ratio. The results have confirmed that variation in the circumferential liquid film thickness within the mixing port coincides well with the spatial distribution of the droplets outside the atomizer. The SMD droplet size distribution found in this study will be used by MHPS for the combustion studies. Based on the flow visualization, a detailed model of the atomization mechanism in internally mixing twin-fluid Y-jet atomizer is proposed. Finally, it is confirmed that internally mixing twin-fluid Y-jet atomizer is not suitable to be used with heavy fuel oil.

7.2 Future Work

Following are my recommendations based on the results and findings for the future work:

Pressure ratio is considered to be an important parameter to determine the internal flow characteristics of twin-fluid Y-jet atomizer. Both experimental and numerical studies are needed to see the effect of pressure ratio on external flow characteristics and on subsequent atomization.

Twin-fluid Y-jet atomizer operating at chocked conditions at the exit of the gas port is reported to produce the smallest SMD (Sauter Mean Diameter). In case of thermal power plants, chocked conditions need to be avoided because large amount of steam/gas is supplied at high velocities to the combustion chamber. However, in applications such as powder drying and spray painting it can be very important operational parameter. There is a need of detailed study of the atomizer operating under chocked condition to enhance its performance for aforementioned applications.

The phenomenon of Prompt Atomization, which is intrinsic to twin fluid atomizers, and its effect is prominent particularly at high gas-t-liquid mass flow rate ratios, is poorly understood. Both numerical and experimental studies are needed to understand the Prompt Atomization

Other alternative numerical methods that allow the transition between an Eulerian and a Lagrangian framework, such as Eulerian–Lagrangian Spray Atomization (ELSA) model, can be used to model the multiphase flow through twin-fluid Y-jet atomizer. The numerical results could be compared with VOF-to-DPM method and against experimental results in open literature.

The effect of variation of liquid-to-gas momentum ratio on liquid film thickness within in the mixing port and the drop size distribution agrees well the studies available in open literature. However, the formation of thin liquid sheets around the mixing point at extremely high liquid-to-gas momentum

ratios and the resulting sharp decrease in the value of SMD as observed in this thesis is not reported before. Therefore both experimental and numerical studies are needed to determine 3-D distribution of the SMD at extremely high liquid-to-gas momentum ratios.

Appendix A: Results with the Mixture Model

Initially, a study was conducted by utilizing mixture multiphase model and SST k-ω turbulence model to determine the physics of the internal nozzle flow. The contours in the Figure A show the volume fraction of the liquid (water) for the GLR ratios of 0.01, 0.06, 0.1, 0.2 and 0.3 for the nozzle 'D.'
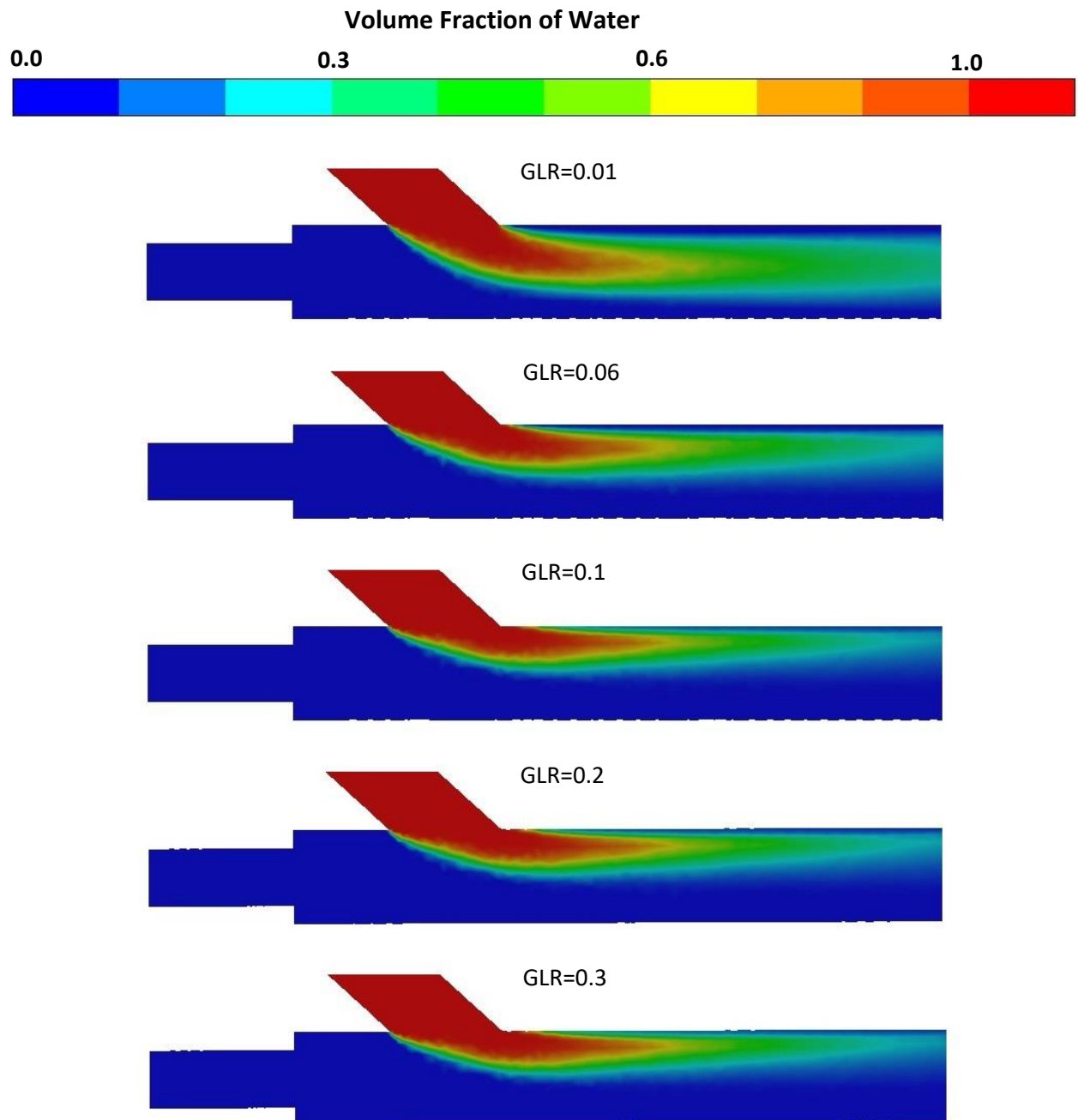
Figure A Contours of volume fraction of water.

Appendix B: Speed of Sound in Gas-Liquid Mixture

Consider a unit infinitesimal mixture of disperse phase (liquid) and continuous phase (gas). The initial densities are denoted by ρ_l and ρ_g and initial pressure in continuous phase by P_g. Surface tension, σ, can be included by denoting the radius of the dispersed phase particle by R. Then the initial pressure in the dispersed phase is $P_l = P_g + 2\sigma/R$.

Now consider an infinitesimal change in pressure P_l to $P_l + \delta P_l$. Any dynamics associated with the resulting fluid motion is ignored. It is assumed that new equilibrium state is achieved. In the absence of any mass exchange between the phases, the new dispersed and continuous phase volumes are respectively

$$(\rho_l \alpha_l) \Big/ \left[\rho_l + \frac{\partial \rho_l}{\partial P_l}\bigg|_s \delta P_l \right] \tag{B.1}$$

$$(\rho_g \alpha_g) \Big/ \left[\rho_g + \frac{\partial \rho_g}{\partial P_g}\bigg|_s \delta P_g \right] \tag{B.2}$$

Adding these together and subtracting from unity, one obtains change in the total volume, δV, and hence sonic velocity c as

$$\frac{1}{c^2} = -\rho \frac{\delta V}{\delta P_g}\bigg|_{\delta P_g \to 0} \tag{B.3}$$

$$\frac{1}{\rho c^2} = \frac{\alpha_l}{\rho_l} \frac{\partial \rho_l}{\partial P_l}\bigg|_s \frac{\delta P_l}{\delta P_g} + \frac{\alpha_g}{\rho_g} \frac{\partial \rho_g}{\partial P_g}\bigg|_s \tag{B.4}$$

If we assume that no dispersed phase particles are created or destroyed, then the ratio $\delta P_l / \delta P_g$ could be determined by evaluating the new dispersed particle size $R + \delta R$ commensurate with the new disperse phase volume and using the relation $\delta P_l = \delta P_g - \frac{2\sigma}{R^2} \delta R$:

$$\frac{\delta P_l}{\delta P_g} = \left[1 \Big/ \left(1 - \frac{2\sigma}{3\rho_l R} \frac{\partial \rho_l}{\partial P_l}\bigg|_s \right) \right] \tag{B.5}$$

Substituting this into the equation B.4 and using, the notations

$$\frac{1}{c_l^2} = \frac{\partial \rho_l}{\partial P_l}\bigg|_s \; ; \qquad \frac{1}{c_g^2} = \frac{\partial \rho_g}{\partial P_g}\bigg|_s \tag{B.6}$$

the result could be expressed as

$$\frac{1}{\rho c^2} = \frac{\alpha_g}{\rho_g c_g^2} + \frac{\alpha_l / \rho_l c_l^2}{[1 - 2\sigma/3\rho_l c_l^2 R]} \tag{B.7}$$

For the sake of simplification and in most of practical circumstances the surface tension effect can be neglected since $\sigma \ll \rho_l c_l^2 R$, then Eq. B.7 could be expressed as

$$\frac{1}{\rho c^2} = \frac{\alpha_g}{\rho_g c_g^2} + \frac{\alpha_l}{\rho_l c_l^2} \tag{B.8}$$

ρc^2 is the effective bulk modulus of the mixture where the effective density $\rho = \alpha_g \rho_g + \alpha_l \rho_l$ is governed by the density of the liquid and the inverse of effective bulk modulus is equal to an average of the inverse bulk moduli of the components ($1/\rho_g c_g^2$ and $1/\rho_l c_l^2$) weighted according to their volume fractions.

Appendix C: Governing Equations

The form of the equations used in this section follows the form of equations used in ANSY Fluent theory guide.

VOF

The compressible Navier-Stokes equations are employed using the finite volume approximation; the Volume of Fluid (VOF) technique with Geometric Reconstruction Scheme is employed in ANSYS Fluent to model the gas-liquid interface. The interface is tracked with the following volume fraction equation (continuity equation). Here α_q is volume fraction in the cell, ρ_q is the density and $\vec{V_q}$ is the velocity vector of qth phase.

$$\frac{d}{dt}(\alpha_q \rho_q) + \nabla.(\alpha_q \rho_q \vec{V_q}) = 0 \qquad (C.1)$$

The volume fraction equation is not solved for the primary phase. The primary phase volume fraction is computed based on following constraint:

$$\sum_{q=1}^{n} \alpha_q = 1 \qquad (C.2)$$

A single set of momentum equation is shared among the phases based on mixture properties.

$$\frac{d}{dt}(\rho \vec{V}) + \nabla.(\rho \vec{V}\vec{V}) = -\nabla P + \nabla.[\mu(\nabla \vec{V} + \nabla \vec{V}^T)] + \rho \vec{g} + \vec{T_\sigma} \qquad (C.3)$$

Where density is defined as: $\rho = \sum \alpha_q \rho_q$, viscosity as: $\mu = \sum \mu_q \alpha_q$, and velocity as: $\vec{V} = \frac{1}{\rho}\sum_{q=1}^{n} \alpha_q \rho_q \vec{V_q}$

$\vec{T_\sigma}$ is the volumetric force source term arising due to the surface tension. It is modelled by continuum surface force model proposed by Brackbill et al. (Brackbill, et al., 1992). This model treats the surface tension as the pressure jump across the interface. The forces at the surface are expressed as volume forces using divergence theorem.

$$T_\sigma = \sum_{pairs,p,q} \sigma_{p,q} \frac{\alpha_p \rho_p k_q \nabla \alpha_q + \alpha_q \rho_q k_p \nabla \alpha_p}{\frac{1}{2}(\rho_p + \rho_q)} \qquad (C.4)$$

The curvature of one surface is negative of other, $k_p = -k_q$ and divergence of the volume fraction is negative of other $\nabla \alpha_p = -\nabla \alpha_q$. This simplifies the equation to:

$$T_\sigma = \sigma_{p,q} \frac{\rho k_p \nabla \alpha_p}{\frac{1}{2}(\rho_p + \rho_q)}$$

(C.5)

where ρ is the volume average density. It is computed as follows:

$$\rho = \sum \alpha_q \rho_q$$

(C.6)

The total energy of the flow is modelled by following equation.

$$\frac{d}{dt}(\rho E) + \nabla.\left(\vec{V}(\rho E + P)\right) = \nabla.\left(K_{eff}\nabla T + \bar{\bar{\tau}} \cdot \vec{V}\right)$$

(C.7)

Here K_{eff} is effective thermal conductivity, $\bar{\bar{\tau}}$ is the viscous stress tensor; the energy E and temperature T are mass averaged variables.

$$E = \frac{\sum_{q=1}^{n} \alpha_q \rho_q E_q}{\sum_{q=1}^{n} \alpha_q \rho_q}$$

(C.8)

E_q is the internal energy of each phase; both phases share the same temperature.

Mixture Model

The mixture model solves the continuity equation, momentum equation and energy equation for the mixture, and the volume fraction equation for the secondary phase, as well as algebraic expression for relative velocities.

The continuity equation for the mixture is

$$\frac{d}{dt}(\rho_{mix}) + \nabla.\left(\rho_{mix}\vec{V}_{mix}\right) = 0$$

(C.9)

Where $\vec{V}_{mix}$ is the mass-averaged velocity:

$$\vec{V}_{mix} = \frac{\sum_{k=1}^{n} \alpha_k \rho_k \vec{V}_k}{\rho_{mix}}$$

(C.10)

and ρ_{mix} is the mixture density:

$$\rho_{mix} = \sum_{k=1}^{n} \alpha_k \rho_k \tag{C.11}$$

α_k is the volume fraction of the phase k.

The momentum equation for the mixture is obtained by summing the individual momentum equation equations for all phases. It is expressed as:

$$\frac{d}{dt}(\rho_{mix}\vec{V}_m) + \nabla.(\rho_{mix}\vec{V}_{mix}\vec{V}_{mix}) = -\nabla P + \nabla.[\mu_{mix}(\nabla\vec{V}_{mix} + \nabla\vec{V}_{mix}^T)] + \rho_{mix}\vec{g}$$
$$+\nabla.\left(\sum_{k=1}^{n} \alpha_k \rho_k \vec{V}_{dr,k} \vec{V}_{dr,k}\right) \tag{C.12}$$

Where n is the number of phases, μ_{mix} is the viscosity of the mixture:

$$\mu_{mix} = \sum_{k=1}^{n} \alpha_k \mu_k \tag{C.13}$$

$\vec{V}_{dr,k}$ is the drift velocity for the secondary phase k:

$$\vec{V}_{dr,k} = \vec{V}_k - \vec{V}_m \tag{C.14}$$

The energy equation for the mixture is expressed as follows:

$$\frac{\partial}{\partial t}\sum_{k=1}^{n}(\alpha_k \rho_k E_k) + \nabla.\sum_{k=1}^{n}\left(\alpha_k \vec{V}_k(\rho_k E_k + P)\right) = \nabla.\left(k_{eff}\nabla T\right) \tag{C.15}$$

where the energy E_k is defined as:

$$E_k = h_k - \frac{P}{\rho_k} + \frac{V_k^2}{2} \tag{C.16}$$

where h_k is the sensible enthalpy of the phase k.

The relative velocity, defined as the velocity of secondary phase (p) relative to primary phase (q), is computed with the following equation:

$$\vec{V}_{pq} = \frac{(\rho_p - \rho_{mix})d_p^2}{18\mu_q f_{drag}}\vec{a} - \frac{\eta_t}{\sigma_t}\left(\frac{\nabla\alpha_p}{\alpha_p} - \frac{\nabla\alpha_q}{\alpha_q}\right) \tag{C.17}$$

Where σ_t is the Prandtl number set to 0.75, η_t is the turbulence diffusivity and $\vec{a}$ is the acceleration of the form:

$$\vec{a} = \vec{g} - (\vec{V}_m.\nabla)\vec{V}_m - \frac{\partial \vec{V}_{mix}}{\partial t} \tag{C.18}$$

f_{drag} is the drag function. It is computed with Schiller and Naumann model:

$$f_{drag} = \begin{cases} 1 + 0.15Re^{0-687} & Re \leq 1000 \\ 0.0183Re & Re > 1000 \end{cases} \tag{C.19}$$

The volume fraction of the secondary phase p is computed from following continuity equation of the phase p:

$$\frac{\partial}{\partial t}(\alpha_p \rho_p) + \nabla.(\alpha_p \rho_p \vec{V}_m) = -\nabla.(\alpha_p \rho_p \vec{V}_{dr,p}) \tag{C.20}$$

Discrete Phase Model (DPM)

The trajectory of the discrete phase is predicted by integrating the force balance on the particle. The force balance equation, which is written in a Lagrangian reference frame, equates the particle inertia with the force acting on the particle. It can be written as:

$$\frac{d\vec{V}_{pr}}{dt} = F_D(\vec{V} - \vec{V}_{pr}) + \frac{\vec{g}(\rho_g - \rho)}{\rho_{pr}} \tag{C.21}$$

Where $F_D(\vec{V} - \vec{V}_{pr}) + \frac{\vec{g}(\rho_{pr} - \rho)}{\rho_{pr}}$ is the drag force per unit particle mass and

$$F_D = \frac{18\mu}{\rho_{pr}d_{pr}^2} \frac{C_D Re_r}{24} \tag{C.22}$$

Here, $\vec{V}$ is the fluid phase velocity, $\vec{V}_{pr}$ is the particle velocity, μ is the molecular viscosity of the fluid, ρ_{pr} is the density and d_{pr} is the diameter of the particle. Re_r is the relative Reynolds number, it is defined as:

$$Re_r = \frac{\rho d_p |\vec{V}_{pr} - \vec{V}|}{\mu} \tag{C.23}$$

C_D is the drag coefficient; according to Morsi and Alexander model (Morsi & Alexander, 1972), it is defined as:

$$C_D = a_1 + \frac{a_2}{Re} + \frac{a_3}{Re^2}$$ (C.24)

Where a_1, a_2 and a_3 are defined as:

$$a_1, a_2, a_3 = \begin{cases} 0, 24, 0 & 0 < Re < 0.1 \\ 3.690, 22.73, 0.0903 & 0.1 < Re < 1 \\ 1.222, 29.1667, -3.8889 & 1 < Re < 10 \\ 0.6167, 46.50, -116.67 & 10 < Re < 100 \\ 0.3644, 98.33, -2778 & 100 < Re < 1000 \\ 0.357, 148.62, -47500 & 1000 < Re < 5000 \\ 0.46, -490.546, 578700 & 5000 < Re < 10000 \\ 0.5191, -1662.5, 5416700 & Re > 10000 \end{cases}$$ (C.25)

The heat balance to relate particle temperature to convective heat transfer at the droplet/particle surface is modeled by following equation:

$$m_{pr} c_{pr} \frac{dT_{pr}}{dt} = hAr_{pr}(T_\infty - T_{pr})$$ (C.26)

where m_{pr} is the mass of the particle, c_{pr} is the heat capacity of the particle, Ar_{rp} is the surface area of the particle, T_∞ is the local temperature of the continuous phase and h is the convective heat transfer coefficient. The convective heat transfer coefficient is evaluated using the correlation of Ranz and Masrshall (Ranz & Marshall, 1952 a) and (Ranz & Marshall, 1952 b) as:

$$\frac{hd_p}{k_\infty} = 2.0 + 0.6Re_r^{1/2}Pr^{1/3}$$ (C.27)

Here k_∞ is the thermal conductivity and $Pr\left(c_p\mu/k_\infty\right)$ is the Prandtl number of the continuous phase.

Wall Modeled Large Eddy Simulations (WMLES)

Gaussian filter is applied to filter out eddies based on length scale Δ (Shur, et al., 2008).

$$\overline{\emptyset}(x,t) = \int_D \emptyset(x',t)G(x,x',\Delta)dx'$$ (C.28)

where G is the filter function that determines the scale of resolved eddies.

$$\Delta= min(max(C_w.ds_w; C_w.h_{max}, h_{wn}); h_{max})$$ (C.29)

h_{max}= maximum edge length, h_{wn}= grid step in wall-normal direction, C_w=0.15, d_w= distance from wall.

After putting the filtered out variables in Navier-Stokes equation and rearranging the terms, it could be expressed as:

$$\frac{(\partial\overline{V}_i)}{\partial t} + \frac{\partial\left(p\overline{V}_i\overline{V}_j\right)}{\partial x_j} = -\frac{\partial\overline{P}}{\partial x_i} + \frac{\partial\left(\overline{\tau}_{ij} + \tau_{ij}^s\right)}{\partial x_j}$$ (C.30)

This equation could be resolved except subgrid-scale stress tensor τ_{ij}^s. It can be expressed by the Boussinesq hypothesis (Hinze, 1975) as:

$$\tau_{ij}^s - \frac{1}{3}\tau_{kk}\delta_{ij} = -2\mu_t\overline{S}_{ij}$$ (C.31)

Where μ_t is the subgrid-scale turbulent viscosity. The isotropic part of the subgrid-scale stresses τ_{kk} is not modeled, but added to the filtered static pressure term. $\overline{S}_{ij}$ is the rate of strain tensor for the resolved scale defined by

$$\overline{S}_{ij} \equiv \frac{1}{2}\left(\frac{\partial\overline{u}_i}{\partial\overline{x}_j} + \frac{\partial\overline{u}_j}{\partial\overline{x}_i}\right)$$ (C.32)

The subgrid scale eddy viscosity is modeled with Smagorinsky SGS model (Smagorinsky, 1963) with van Driest damping (Van Driest, 1956) and Prandtl mixing length model as:

$$\nu_t = min\left[(kds_w)^2, \left(C_{smag}\Delta\right)^2\right][1 - exp[-(y^+/25)^3]]|S - \Omega|$$ (C.33)

$C_{smag} = 0.2$ is the Smagorinsky constant, as established by Shur et al [48], $\Omega=$ is the vorticity, S is the magnitude of the strain tensor, $k = 0.41$ is the Von Karman Constant. Near the wall the minimum

function selects the Prandtl mixing length model whereas away from the wall it switches over to the Smagorinsky model.

$K\omega$ Model

The turbulence kinetic energy K, and the specific dissipation rate ω, are obtained from the following transport equations:

$$\frac{\partial(\rho K)}{\partial t} + \frac{\partial(\rho K u_i)}{\partial x_i} = \frac{\partial}{\partial x_j}\left(\Gamma_K \frac{\partial K}{\partial x_j}\right) + G_k - Y_K \tag{C.34}$$

and

$$\frac{\partial(\rho\omega)}{\partial t} + \frac{\partial(\rho\omega u_i)}{\partial x_i} = \frac{\partial}{\partial x_j}\left(\Gamma_\omega \frac{\partial \omega}{\partial x_j}\right) + G_\omega - Y_\omega \tag{C.35}$$

In these equations, the term G_k represents the generation of turbulence kinetic energy due to mean velocity gradients. G_ω represents the generation of ω. Γ_K and Γ_ω are the effective diffusivity of K and ω respectively. Y_K and Y_ω represents the dissipation of K and ω due to turbulence.

The effective diffusivities of the $K\omega$ model are defined as follows:

$$\Gamma_K = \mu + \frac{\mu_t}{Pr_K} \tag{C.36}$$

$$\Gamma_\omega = \mu + \frac{\mu_t}{Pr_\omega} \tag{C.37}$$

Where Pr_K and Pr_ω are turbulent Prandtl numbers for K and ω respectively. The turbulence viscosity μ_t is computed as:

$$\mu_t = \frac{\rho K}{\omega} \tag{C.38}$$

The production of turbulence kinetic energy (G_k) is modeled with the following equation.

$$G_K = \left(\frac{\rho K}{\omega}\right) S^2 \tag{C.39}$$

Where S is the modulus of the mean rate of strain tensor, it is defined as follows:

$$S \equiv \sqrt{2S_{ij}S_{ij}}$$

(C.40)

The production of ω is given by

$$G_\omega = \rho S^2$$

(C.41)

The dissipation of K is given by

$$Y_K = \rho \beta^* f_{\beta^*} K \omega$$

(C.42)

Where

$$f_{\beta^*} = \begin{cases} 1 & X_K \leq 0 \\ \dfrac{1 + 680 X_K^2}{1 + 400 X_K^2} & X_K > 0 \end{cases}$$

(C.43)

$$X_K \equiv \frac{1}{\omega^3} \frac{\partial K}{\partial x_j} \frac{\partial \omega}{\partial x_j}$$

(C.44)

$$\beta^* = [1 + 1.5 F(M_t)]$$

(C.45)

$F(M_t)$ is the compressibility function, it is defined as

$$F(M_t) = \begin{cases} 0 & M_t \leq 0 \\ M_t^2 - (0.25)^2 & M_t > 0.25 \end{cases}$$

(C.46)

where

$$M_t^2 \equiv \frac{2K}{a^2}$$

(C.47)

And

$$a = \sqrt{\gamma R T}$$

(C.48)

Publications

Journal Publications

"Atomization Mechanism of Internally Mixing Twin-Fluid Y-Jet Atomizer," *Journal of Energy Engineering*, Vol. 147, Issue 1, 2021, **Nazeer, Y. H**.; Ehmann, M.; Sami, M.; and Gavaises, M. https://doi.org/10.1061/(ASCE)EY.1943-7897.0000723

"The Influence of geometrical and operational parameters on internal flow characteristics of Internally Mixing Twin-Fluid Y-Jet Atomizers," *Atomization and Sprays*, Vol. 29, Issue 5, 2019, **Nazeer, Y. H**.; Ehmann, M.; KouKouvinis, P.; and Gavaises, M. DOI: 10.1615/AtomizSpr.2019030944

Conference Publication

"Internal Flow Characteristics of Internally Mixing Twin-Fluid 'Y' Type Atomizer," *14th International Conference on Liquid Atomization and Spray Systems,* 2018, Chicago, USA, **Nazeer, Y. H**.; Ehmann, M.; Agraniotis, M.; KouKouvinis, P.; and Gavaises.

References

Adler, D. & Lyn, W. T., 1969. The evaporation and mixing of a fuel spray in a diesel air swril. *Proceeding of Institute of Mechanical Engineering,* Volume 184.

Alfonsi, G., 2009. Reynolds-Averaged Navier-Stokes Equations for Turbulence Modeling. *Applied Mechanics Reviews,* 62(4), pp. 1-20.

Alfonsi, G., 2011. On Direct Numerical Simulation of Turbulent Flows. *Applied Mechanics Review,* 64(2), pp. 30-63.

Anderson, J. D., 1995. *Computational fluid dynamics: the basics with applications..* New York: McGraw-Hill.

Andrade, A., Skurtys, O. & Osorio, F. A., 2012. Atomizing Spray Systems for Application of EdibleCoatings. *Comprehensive reviews in food science and food safety,* 11(3), pp. 323-337.

Andreussi, P. et al., 1994. *Measurement of Film Thickness within a Y-Jet Atomizer.* s.l., International conference on liquid atomization and spray systems, pp. 632-639.

Andreussi, P., Tognotti, L., Michele, G. D. & Graziadio, M., 1992. Design and Characterization of Twin-Fluid Y-Jet Atomizers. *Atomization and Sprays,* Volume 2, pp. 45-59.

Arcoumanis, C. & Gavaises, M., 1999. Modelling of Pressure-Swirl Atomizers for GDI Engines. *SAE International Journal of Engines,* 108(3).

Arcoumanis, C., Gavaises, M., Abdul-Wahab, E. & V., M., 1999. Modeling of Advanced High-Pressure Fuel Injection Systems for Passenger Car Diesel Engines. *Transaction Journal of Engines,* 108(3).

Arcoumanis, C., Gavaises, M., Argueyrolles, B. & Galzin, F., 1999. Modeling of Pressure-Swirl Atomizers for GDI Engines. *Transactions Journal of Engines, SAE Paper,* 108(3), pp. 516-532.

Argyropoulos, C. D. & Markatos, N. C., 2015. Recent advances on the numerical modelling of turbulent flows. *Applied Mathematical Modelling,* 39(2), pp. 693-732.

Baker, O., 1954. Simulteanous Flow of Oil and Gas. *Oil and Gas Journal,* 52(1), pp. 25-35.

Barreras, F., Lozano, A., Barroso, J. & Lincheta, E., 2006. Experimental characterization of industrial twin-fluid atomizers. *Atomization and Sprays,* Volume 16, pp. 145-147.

Barreras, F., Lozano, A., Ferreira, G. & Lincheta, 2008. *The effect on the inner flow on the performance of a twin-fluid nozzle with an iternal mixing chamber.* Como Lake, European Conference on Liquid Atomization and Spray Systems.

Barreras, F., Lozano, A., Ferreira, G. & Lincheta, E., 2006. *Study of the Internal Flow Condition on the Behavior of Twin-Fluid Nozzle with Internal Mixing Chamber.* Kyoto, International Conference on Liquid Atomization and Spray Systems.

Bidone, G., 1829. *Experiences sur la Forme et sur la Direction des Veines et des Courants d' Eau Lances par Diverses Ouvertures.* Turin: Imprimerie Royale.

Birouk, M. & Lekic, N., 2009. Liquid Jet breakup in quiescent atmosphrere. *Atomization and Sprays,* Volume 19, pp. 501-528.

Boggavarapu, P. & Ravikrishna, R. V., 2013. A Review on Atomization and Sprays of Biofuels for IC Engine Applications. *International Journal of Spray and Combustion Dynamics,* 5(2), pp. 85-121 .

Brackbill, J. U., Kothe, D. B. & Zemach, C., 1992. A continum method for modeling surface tension.. *Journal of Computational Physics,* 100(2), pp. 335-354.

Broukal, J. & Hajek, J., 2011. Validation of an effervescent spray model with secondary atomization and its application to modeling of a large-scale furnace. *Applied Thermal Engineering,* 31(13), pp. 2153-2164.

Bryce, W., Cox, N. & Joyce, W., 1978. *Oil droplet production and size measurement from a twin-fluid atomizer using real fluids.* Tokyo, 3rd International Conference onLiquid Atomization and Sprays, pp. 259-263.

Buckner, H. N., Sojka, P. E. & Lefebvre, A. H., 1990a. Effervescent atomization of coal-water slurries. *ASME publication,* Volume 30, pp. 105-108.

Buckner, H. N., Sojka, P. E. & Lefebvre, A. H., 1990b. *Effervescent atomization of non-Newtonian single phase liquid.* Hartford, Connecticut, Proceedings of the fourth Annual Conference on Atomization and Sprays.

Chehade, Z. et al., 2020. Review and analysis of demonstration projects on power-to-X pathways in the world. *International Journal of Hydrogen EnergyChechade, ,* 44(51), pp. 27637-27655.

Chin, J. S. & Lefebvre, A. H., 1992. *Flow Regimes in the Efervescent Atomization.* San Ramon, 5th annual conference on Liquid Atomization and Spray Systems. .

Chin, J. S. & Lefebvre, A. H., 1993. Flow Patterns in Internal-Mixing Twin-Fluid Atomizers. *Atomization and Sprays,* Volume 3, pp. 463-374.

Clare, H. & Radcliffe, A., 1954. An airblast atomizer for use with viscous fuels. *Journal of Institute of fuel,* 27(165), pp. 510-515.

Crowe, C., 2006. *Multphaseflow handbook.* Newyork: Taylor & Franks.

Dafsari, R. A., Vashahi, F. & Lee, J., 2017. Effect of the swril chamber length on the atomization characteristics of pressure-swirl nozzle.. *Atomization and Sprays,* 27(10), pp. 859-874.

De Michele, G., Graziadio, M., Morelli, F. & Novelli, G., 1991. *Characterization of the spray structure of a large scale H.F.O. Atomizer.* Gaithersburg, Proceedings of ICLASS.

Dombrowski, N., Hanson, D. & Ward, D., 1960. Some Aspects of Liquid Flow Through Fan Spray Nozzles. *Chemical Engineering Science,* Volume 12, pp. 33-50.

Dombrowski, N. & Johns, W., 1963. The aerodynamic instability and disintegration of viscous liquid sheets. *Chemical Engineering Science,* 18(7), pp. 203-214.

Dombrowski, N. & Johns, W. R., 1963. The aerodynamic instability and disintegration of viscous liquid sheets. *Chemical Engineering Science,* 18(3), pp. 203-214.

El-Batsh, H.M., D. M. & Hassan, A., 2012. On the application of mixture model for two-phase flow induced corrosion in a complex pipline configuration. *Applied Mathematical Modeling ,* Volume 36, pp. 5686-5699.

Elkotb, M. M., 1982. Fuel atomization for spray modeling. *Progress in Energy and Combustion Sciences,* Volume 8, pp. 61-91.

Esfarjani, S. A. & Dolatabadi, A. A., 2009. 3D simulation of two-phase flow in an effervescent atomizer for suspension plasma spray. *Surface Coating Technology,* Volume 203, pp. 2074-2280.

European-Comission, 2018. *A Clean Planet for all- A European strategic long-term vision for a prosperous, modern, competitive and climate neutral economy,* Brussels: European Comission.

European-Comission, 2019a. *United in dilivering the Energy Union and Climate Action- Setting the foundations for a successful clean energy transition.,* Brussels: European Comission.

European-Comission, 2019b. *Fourth report on the State of the Energy Union,* Brussels : European Comission .

Ferreria, G., Garcia, A. J., Barreras, F., Lozano, A. & Lincheta, E., 2009. Design and optimization of twin-fluid atomizers with an internal mixing chamber for heavy fuel oils. *Fuel Processing Technology,* Volume 90, pp. 270-278.

Fraser, R. P., Eisenklam, P., Dombrowski, N. & Hasson, D., 1985. Drop Formation from Rapidly Moving Sheets. *Journal of AIChE,* 8(1962), pp. 672-680.

Gadgil, H. P. & Raghunandan, B. N., 2011. Some features of spray breakup in effervescent atomizers. *Experiments in Fluids,* Volume 50, pp. 329-338.

Gavaises, M. & Arcoumanis, C., 2001. Modelling of sprays from high-pressure swirl atomizers. *International Journal of Engine Reserach,* 2(2), pp. 95-117.

Gibson, M. M. & Launder, B. E., 1978. Ground Effects on Pressure Fluctuations in the Atmospheric Boundary Layer. *Journal of Fluid Mechanics,* Volume 86, pp. 491-511.

Gopala, V. R. & Berend, G. M., 2008. Volume of Fluids Methods for Immiscible-Fluids and Free-Surface Flows. *Chemical Engineering Journal,* Volume 141, pp. 204-221.

Gurubaran, R. K., Sujith, R. I. & Chakravarthy, S. R., 2012. Characterization of a Prefilming Airblast Atomizer in a Strong Swirl Flow Field. *Journal of Propulsion and Power,* Volume 24.

Hassell, D. C., Majidi, V. & Holcombe, J. A., 1991. Temperature programmed static secondary ion mass spectrometric study of phosphate chemical modifiers in electrothermal atomizers. *Journal of Analytical Atomic Spectrometry ,* Volume 6, pp. 105-108 .

Hawkes, N., Lawrence, C. & Hewitt, G., 2000. Studies of Wispy-Annular Flow Using Trasient Pressure Gradient and Optical Measurement. *International Journal of Multiphase Flow,* Volume 26, pp. 1565-1582.

Heng, Q. P., Jasuja, A. K. & Lefebvre, A. H., 1996. Influence of air and fuel flows on gas turbine sprays at high pressures. *Symposium on Combustion,* 26(2), pp. 2757-2762.

Hewitt, G. & Roberts, D., 1969. *Studies of two-phase flow patterns by simultaneous X-ray and flash photography.,* Harwell: Atomic Energy Research Establishment.

Hinze, J. O., 1955. Fundamentals of hydrodynamic mechanism of splitting in dispersion processes. *AIChE Journal,* Volume 1, pp. 289-295.

Hinze, J. O., 1975. *Turbulence.* New York: McGraw-Hill Publishing Co..

Hinze, J. O. & Milborn, H., 1950. Atomization of liquid by Rotating cups. *ASME Journal of Applied Mechanics,* 17(2), pp. 145-153.

Hirt, C. W. & Nichlos, B. D., 1981. Volume of fluid (VOF) method for the dynamics of free boundaries. *Journal of Computational Physics,* 39(1), pp. 201-225.

Huang, X., Wang, X. & Liao, G., 2011. *Characterization of an effervescent atomization water mist nozzle and its fire suppression tests.* s.l., Proceedings of Combustion Institute, pp. 2573-2579.

Inamura, T. et al., 2019. Effects of prefilmer edge thickness on spray characteristics in prefilming airblast atomization. *International Journal of Multiphase Flow,* Volume 121.

Inamura, T. et al., 2019. Effects of prefilmer edge thickness on spray characteristics in prefilming airblast atomization. *International Journal of Multiphase Flow,* Volume 121.

Inamura, T. & Nagai, N., 1985. *The relative performance of externally and internally-mixed twin-fluid atomizers.* London, Proceedings of the 3rd International Conference on Liquid Atomization and Sprays.

Jang, X., Siamas, G. A., Jagus, K. & Karayiannis, T., 2010. Physical Modelling and Advanced Simulations of Gas-Liquid two-phase jet flows in atomization and Sprays. *Progress in Energy and Combustion Science,* Volume 36, pp. 131-167.

Jasuja, A. K. & Rosfjord, T. J., 1979. Atomization of crude and residual fuel oils. *ASME Journal of Engineering for Gas Turbines and Power,* 101(2), pp. 250-258.

Jiang, X., Siamas, G. A., Jagus, K. & Karayiannis, T. G., 2010. Physical modelling and advanced simulations of gas-liquid two-phase jet flows in atomization and sprays. *Progress in Energy and Combustion Science,* Volume 36, pp. 131-167.

Kallio, S. & Akademi, A., 1996. *On the mixture model for multiphase flow,* Espoo: VTT Publications.

Kieffer, S. W., 1977. Sound Speed in Liquid-Gas Mixtures: Water-Air and Water-Steam. *Journal of Geophysical Research,* Volume 82, pp. 2895-2904.

Koukouvinis, P., Gavaises, M., Li, J. & Wang, L., 2016. Large Eddy Simulation of Diesel Injector Including Cavitation Effects and Correlation to Erosion Damage. *Fuel,* Volume 175, pp. 26-39.

Koukouvinis, P., Naseri, H. & and Gavaises, M., 2016. Performance of Turbulence Models and Effect of Cavitation Models in Prediction of Incipient Cavitation. *International Journal of Engine Research.*

Krzywoblocki, M. A., 1957. Jets-Review of literature. *Jet Propulsion,* Volume 26, pp. 760-779.

Kufferath, A., Wende, B. & Leuckel, W., 1999. Influence of liquid flow condtions on spray characteristics of internal-mixing twin-fluid atomizers. *International journal of heat and fluid flow,* Volume 20, pp. 513-519.

Kumar, V. et al., 2018. *A hybrid approach for modeling fully resolved liquid film formation by converting lagrangian particles to eulerian VOF structures.* Chicago, International Conference on Liquid Atomization and Sprays Systems.

Lagutkin, S. et al., 2004. Atomization process for metal powder. *Materials Science and Engineering,* 383(1), pp. 1-6.

Lakhehal, D., Meier, M. & Fulgosi, M., 2002. Interface Tracking towards the Direct Simulation of Heat an d Mass Transfer in Multiphase Flows. *International Journal of Heat and Fluid Flow,* Volume 23, pp. 242-257.

Lane, W. R., 1951. Shatter of drops in streams of air. *Industrial and Engineering Chemistry,* Volume 43, pp. 1312-1317.

Lang, R., 1962. Ultrasonic Atomization of Liquids. *Journal of Acoustical Society of America,* 34(1), pp. 6-8.

Launder, B. E., 1989. Second-Moment Closure: Present... and Future?. *International Journal of Heat and Fluid Flow,* 10(4), pp. 282-300.

Launder, B. E., Reece, G. J. & Rodi, W., 1975. Progress in the Development of a Reynolds-Stress Turbulence Closure. *Journal of Fluid Mechanics,* 68(3), pp. 537-566.

Lefebrve, A. H., 1992. Twin-Fluid Atomization: Factors Influencing Mean Drop Size. *Atomization and Sprays,* Volume 2, pp. 101-119.

Lefebvre, 1988b. A novel method of atomization with potential gas turbine application. *Indian defence science journal,* Volume 38, pp. 353-362.

Lefebvre, A. H., 1980. Airblast Atomization. *Progress in Energy and Combustion Sciences,* Volume 6, pp. 223-261.

Lefebvre, A. H., 1980. Airblast Atomization. *Progress in Energy and Combustion Sciences ,* Volume 6, pp. 223-261.

Lefebvre, A. H., 1988. A Novel Method of Atomization with Potential Gas Turbine Application. *Defense Sci. J.,* Volume 38, pp. 353-362.

Lefebvre, A. H. & McDonell, V. G., 2017. *Atomization and Sprays.* 2 ed. New York: CRC Press.

Lefebvre, A. H., Wang, X. F. & Martin, C. A., 1988a. Spray characteristics of aerated-liquid pressure atomizers. *AIAA Journal of Propulsion and Power.,* Volume 4, pp. 293-298.

Lefenvre, A. H., 1992. Energy consideration in twin-fluid atomization. *Journal of Engineering in gas turnine and power,* Volume 114, pp. 89-96.

Levy, Y., Sherbaum, V., Levin, D. & Ovcharenko, V., 2005. *Airblast Swirl Atomizer for Small Je.* Reno, Neveda, ASME Turbo Expo 2005: Power for Land, Sea, and Air.

Li, H., Rutland, C. J., Perez, F. E. H. & Im, G. H., 2020. Large-eddy spray simulation under direct-injection spark-ignition engine-like conditions with an integrated atomization/breakup model. *International Journal of Engine Research.*

Li, et al., 2018. Performance enhancement of a trapped-vortex combustor for gas turbine engines using a novel hybrid-atomizer. *Applied Energy,* Volume 216, pp. 286-295.

Lin, S. P. & Kang, D. J., 1987. Atomization of Liquid Jet. *Physics of Fluids,* Volume 30, pp. 2000-2006.

Lin, S. P. & Reitz, R. D., 1998. Drop and Spray foirmation from a Liquid Jet. *Annual Review of Fluid Mechanics,* Volume 30, pp. 85-105.

Li, S. et al., 2018. EXPERIMENTAL INVESTIGATION ON NEAR-FIELD BREAKUP CHARACTERISTICS OF HYBRID-MIXED TWIN-FLUID ATOMIZER. *Atimization and Sprays,* 28(10), pp. 601-914.

Li, W., Qian, L., Song, S. & Zhong, X., 2019. Numerical Study on the Influence of Shaping Air Holes on Atomization Performance in Pneumatic Atomizers. *Coatings,* 9(7).

Li, Z. et al., 2012. Mixing and atomization characteristics in an internal-mixing twin-fluid atomizer. *Fuel,* Volume 97, pp. 306-314.

Loebker, D. & Empie, H. J., 1997. *High mass flowrate effervescent spraying of high viscosity Newtonian liquid.* Ottawa, 10th Annual Conference on Liquid Atomization and Spray Systems, p. 253–257.

Loth, E., 2009. *Computational Fluid Dynamics of Bubbles, Drops and Particles.* Cambridge: Cambridge University Press.

Mahdi, F. & Christian, B., 2017. *Synthetic Methanol and Dimethyl Ether Production based on Hybrid PV-Wind Power Plants.* Dusseldorf, 11th International Renewable Energy Storage Conference .

Maski, D. & Durairaj, D., 2010. Effects of electrode voltage, liquid flow rate, and liquid properties on spray chargeability of an air-assisted electrostatic-induction spray.. *Journal of Electrostatics,* 68(2), pp. 152-158.

McWilliam, D. & Duggins, R., 1969. *Speed of Sound in Bubbly Liquids.* s.l., Proceedings of the Institution of Mechanical Engineering.

Menter, F. R., 1994. Two-Equation Eddy-Viscosity Turbulence Models for Engineering Applications. *AIAA Journal,* 32(8), p. 1598–1605.

Menter, F. R. & Egorov, Y., 2010. Scale-Adaptive Simulation Method for Unsteady Flow Predicitions Part1: Theory and Model Description. *Journal of Flow Turbulence and Combustion,* pp. 113-138.

Menter, F. R. et al., 2011. *Scale-Resolving Simulations Techniques in Industrial CFD.* Hawaii, American Institute of Aeronautics and Astronautics.

Michhele, D. G., Graziadio, M., Morelli & Novelli, G., 1991. *Characterization of the Spray Structure of a Large Scale H.F.O. Atomizer.* Gaithersburg, Iternational Conference on Liquid Atomization Systems and Sprays.

Mitroglou, N. & Gavaises, M., 2011. *Cavitation Inside Real-Size Fully Transparent Fuel Injector Nozzles and Its Effect on Near-Nozzle Spray Formation.* Bergamo, DIPSI Workshop on Droplet Impact Phenomena and Spray Investigations.

Mlkvik, M. et al., 2015. Twin-Fluid atomization of viscous liquids: The Effect of atomizer construction on breakup process, spray stability and droplet size. *International Journal of Multiphase,* Volume 77, pp. 19-32.

Morsi, S. A. & Alexander, A. J., 1972. An investigation of Particle Trajectories in Two-Phase Flow Systems. *Journal of Fluid Mechanics,* 55(2), pp. 193-208.

Mujumdar, A. S., Huang, L. X. & Chen, X. D., 2010. An overview of the recent advances in spray-drying.. *Dairy Sci. Technolgy,* Volume 90, pp. 211-224.

Mullinger, P. & Chigier, N., 1974. The Design and Performance of Internal Mixing Multijet Twin Fluid Atomizers. *Journal of the institute fuel,* Volume 47, pp. 251-261.

Naseri, H. et al., 2018. Turbulence and Cavitation Suppression by Quaternary Ammonium Salt Additives. *Nature Scientific Reports 8, Article number: 7636.*

Nazeer, Y., Ehmann, M., Koukouvinis, F. & Gavaises, M. I. 2., 2018. *Internal Flow Characteristics of Twin-Fluid 'Y' Type Internally Mixing Atomizer.* Chicago, International Conference on Liquid Atomization and Sprays Systems.

Nazeer, Y. H., Ehmann, M., Koukouvinis, P. & Gavaises, M., 2019. The Influence of Geometrical and Operational Parameters on Internal Flow Characteristics of Internally Mixing Twin-Fluid Y-Jet Atomizers. *Atomizations & Sprays,* 59(5), pp. 403-428.

Neya, K., Sato, S. & Hatopri, K., 1975. Study of y-jet Twin Flid Atomizer. *Ship Reserach Institute ,* 12(1), pp. 1-19.

Nguyen, D. & Rhodes, M. J., 1998. Producing Fine Drops of Water by Twin-Fluid Atomization. *Powder Technology,* Volume 99, pp. 285-292.

Nikitin, F. et al., 2000. An approach to wall modeling in large-eddy simulations. *Physics of Fluids,* 12(7), pp. 1629-1632.

Nykteri, G. et al., 2020. A Σ-Υ two-fluid model with dynamic local topology detection: Application to high-speed droplet impact. *Journal of Computational Physics,* Volume 408.

Nykteri, G. et al., 2020. A Σ-Υ two-fluid model with dynamic local topology detection: Application to high-speed droplet impact. *Journal of Computational Physics,* Volume 408.

Okabe, T. et al., 2019. TIME-DEPENDENT BREAKUP LENGTH OF LIQUID SHEET IN PREFILMING TYPE OF AIRBLAST ATOMIZER. *Atomization & Sprays,* 29(1), pp. 289-303.

Okabe, T. et al., 2019. Time-dependent breakup length of liquid sheet in prefilming type of airblast atomizer. *Atomization & Sprays,* 29(1), pp. 289-303.

Oshinnowo, T. & Charles, M. E., 1974. Vertical Two-Phase Flow; Part1, Flow Pattern Correlations. *Journal of Chemical Engineering,* Volume 52, pp. 25-35.

Oshinowo, T. C. M. E., 1974. Vertical Two-Phase Flow; Part 1, Flow Pattern Correlations. *The Canadian Journal of Chemical Engineering,* 52(1), pp. 25-35.

Pacifico, A. L. & Yanagihara, J. I., 2014. The influence of geometrical and operational parametrs on Y-jet atomizers performance. *Journal of Brazilian Society of Mechanical Science and Engineering,* Volume 36, pp. 13-32.

Piomelli, U. & Balaras, E., 2002. Wall-layer Models for Large-Eddy Simulations. *Annual Review of Fluid Mechanics ,* Volume 34, pp. 349-374.

Plateau, J., 1945. *Satique experimentale et theorique des liquides soumis aux seules forces moleculaires.* New York : Dover Publications .

Prasad, K. S. L., 1982. *Characterization of Air Blast Atomizers.* madison wisconsin, International Conference on Liquid Atomization and Spray Systems.

Rachner, M., Becker, J., Hassa, C. & Doerr, T., 2001. Modelling of the atomization of a plain liquid fuel jet in crossflow at gas turbine conditions. *Aerospace Science and Technology,* 6(7), pp. 495-506.

Radclife, A., 1955. Proc. Inst. Mech. Eng., 169, pp. 93-106, 1955.The performance of a Type of Swirl Atomizer. *Proceedings of the Institution of Mechanical Engineers,* Volume 169, pp. 93-106.

Ranz, W. E. & Marshall, W. R., 1952 a. Evaporation from drops, Part 1. *Chemical Engineering Progress,* 48(3), pp. 141-146.

Ranz, W. E. & Marshall, W. R., 1952 b. Evaporation from Drops Part 1 and Part 2. *Chemical Engineering Progress,* 48(4), pp. 173-180.

Rayleigh, L., 1878. On the instability of jets. *Proceedings of the London Mathematical Society,* Volume 10, pp. 4-13.

Rink, K. K. & Lefebvre, A. H., 1986. *Influence of Fuel Drop Size and Combustor Operating Conditions on Pollutant Emissions.* s.l., SAE Technical Paper.

Rizk, N. K. & Lefebvre, A. H., 1953. The Influence of Liquid Film Thickness on Airblast Atomization. *ASME Journal of Engineering for gas turbines and power,* Volume 102, pp. 706 - 710.

Roesler, T. C. & Lefebvre, A. H., 1989. Studies on aerated-liquid atomization. *International journal of turbojet engines,* Volume 6, pp. 221-230.

Roudini, M. & Wozniak, G., 2018. Experimental Investigation of Spray Characteristics of Pre-filming Air-blast Atomizers. *Journal of Applied Fluid Mechanics,* 11(6), pp. 1455 - 1469.

Roudini, M. & Wozniak, G., 2018. Experimental Investigation of Spray Characteristics of Pre-Filming Air-blast Atomizers. *Journal of Applied Fluid Mechanics,* 11(6), pp. 1455-1469.

Saleh, A., Amini, G. & Dolatabadi, A., 2018. PENETRATION OF AERATED SUSPENSION SPRAY IN A GASEOUS CROSSFLOW. *Atomization and Sprays,* 28(2), pp. 91-110.

Sami, M., Schuetze, P., Hutcheson, P. & Aguado, P., 2019. *Best Practices in the numerical modelling of liquid atomization processes.* Tempe, Arizona, ILASS-Americas 30th Annual Conference on Liquid Atomization and Spray System.

Savart, F., 1833. Memoire sur le choc d'une veine liquide lancee sur un plan circulaire. *Annales de chimie et de physique,* Volume 53, pp. 337-386.

Schtze, J. et al., 2018. *A multimodel hybrid approach for the numerical simulation of fluid phase dispersion process.* Chicago, International Conference on Liquid Atomization and Sprays Systems.

Shih, T. H. et al., 1995. A New Eddy-Viscosity Model for HighReynolds Number Turbulent Flows - Model Development and Validation. *Computer Fluids,* 24(3), pp. 227-238.

Shur, M. L., Spalart, P. R., Strelets, M. K. & Travin, A. K., 2008. A hybrid RANS-LES approach with delayed-DES and wall-modelled LES capabilities. *International Journal of Heat and Fluid Flow,* Volume 29, pp. 1638-1649.

Shur, M., Strelets, P., Spalart, M. & Travin, A., 1999. Detached-eddy simulation of an airfoil at high angle of attack. *Engineering Turbulence Modeling and Measurements,* Volume 4, pp. 669-678.

Sirignano, W. A. & Mehring, C., 2000. Review of theory of distortion and disintegration of liquid sheets. *Progress in Energy and Combustion,* Volume 26, pp. 609-655.

Smagorinsky, J., 1963. General Circulation Experiments with the Primitive Equations. *Monthly Weather Review,* Volume 91, pp. 99-165.

Song, S. H. & Lee, S. Y., 1996. Study of Atomization Mechanism of Gas/Liquid Mixtures Flowing Through Y-Jet Atomizers. *Atomization and Sprays,* Volume 6, pp. 193-209.

Song, S. & Lee, S., 1994. *An Examination of Spraying Performance of Y-Jet Atomizers- Effect of Mixing Port Length.* Rouen, International Conference on Liquid Atomization and Spray Systems.

Sovani, S. D., Sojka, P. E. & Lefebvre, A. H., 2001. Effervescent Atomization. *Progress in Energy and Combustion Sciences,* Volume 27, pp. 483-521.

Sovani, S., Sojka, P. & Lefebvre, A., 2001. Effervescent Atomization. *Progress in Energy and Combustion Sciences,* 27(4), pp. 483-521.

Spalart, P. & Allmaras, S., 1992. *A one-equation turbulence model for aerodynamic flows,* Reno, Neveda: American Institute of Aeronautics and Astronautics.

Spalart, P. et al., 2006. A new version of detached-eddy simulation, resistant to ambugous grid densities. *Theoretical and Computational Fluid Dynamics ,* 20(3), pp. 181-195.

Spalart, P., Jou, W., Strelets, M. & Allmaras, S., 1997. *Comments on the Feasibility of LES for Wings, and on a hybrid RANS/LES approach.* Louisiana , First AFOSR International Conference on DNS/LES .

Spedding, P. L. & Nguyen, V. T., 1980. Regime Maps for Air-Water Two Phase Flow. *Chemical Engineering Science,* 35(1980), pp. 779-793.

Stefanitsis, D. et al., 2019b. Numerical investigation of the aerodynamic breakup of droplets in tandem. *International Journal of Multiphase Flow,* Volume 113, pp. 289-303.

Stefanitsis, D., Strotos, G., Nikolopoulos, N. & Gavaises, M., 2019a. Numerical investigation of the aerodynamic breakup of a parallel moving droplet cluster. *International Journal of Multiphase Flow,* Volume 121.

Strotos, G. et al., 2011. Non-dimensionalisation parameters for predicting the cooling effectiveness of droplets impinging on moderate temperature solid surfaces. *International Journal of Thermal Sciences,* Volume 50, pp. 698-711.

Strotos, G., Malgarinos, I., Nikolopoulos, N. & Gavaises, M., 2016a. Aerodynamic breakup of an n-decane droplet in a high temperature gas environment. *FUEL,* Volume 185, pp. 370-380.

Strotos, G., Malgarinos, I., Nikolopoulos, N. & Gavaises, M., 2016b. Predicting droplet deformation and breakup for moderate Weber numbers. *International Journal of Multiphase Flow,* Volume 85, pp. 96-109.

Strotos, G. et al., 2018. Determination of the aerodynamic droplet breakup boundaries based on a total force approach. *International Journal of Heat and Fluid Flow,* Volume 69, pp. 164-173.

Tanasawa, Y., Miyasaka, Y. & Umehara, M., 1978. *Effect of Shape of Rotating Disks and Cups on Liquids Atomization.* Tokyo, 1st International Conference on Liquid Atomization and Spray Systems, pp. 165-172.

Tanner, F. X., Feigl, K., Karrio, O. & Windhab, E. J., 2016. Modeling and Simulation o fair-assist atomizers with applications to food spray.. *Applied Mathematical Modeling ,* Volume 40, pp. 6121-6133.

Tapia, Z. & Chavez, A., 2002. *Internal flow in Y-Jet atomizer- numerical study.* Zaragoza, ILASS-Europe .

Tonini, S., Gavaises, M. & Theodorakakos, A., 2008. Modelling of high-presure dense diesel sprays with adaptive local grid refinement. *International journal of Heat and Fluid Flows,* Volume 29, pp. 427-448.

Tryggvason, G., 1997. *Computational Investigation of Atomization,* s.l.: Report Number A915353.

Tyler, F., 1933. Instability of Liquid Jets. *Philosophical Magzine,* Volume 16, pp. 504-518.

Vallet, A., Burluka, A. A. & Borghi, R., 2001. Development of a Eulerian model for the 1168 "atomization" of a liquid jet. *Atomization and Sprays,* 11(6).

Van Driest, E. R., 1956. On Turbulent flow near a wall. *Journal of Aeronautical Sciences,* Volume 23, pp. 1007-1011.

Wade, R. A. et al., 1999. Effervescent atomization at injection pressures in the MPa range.. *Atomization Sprays,* Volume 9, pp. 651-667.

Wang, X. F., Chin, J. S. & Lefebvre, A. H., 1989. Influence of the gas injector geometry on atomization performance of aerated-liquid nozzles. *International journal of turbojet engines,* Volume 6, pp. 271-280.

Warnatz, J., Mass, U. & Dibble, R. W., 2001. *Combustion: Physical and Chemical fundamentals, Modeling and Simulation, Experiments.* 3rd. ed. Berlin: Springer-verlag.

Weber, C., 1931. Disintegration of liquid Jets. *Zeitschrift fur Angewandte Mathematik und Mechanik,* Volume 11, pp. 136-159.

Wen, W. & Piomelli, U., 2016. Reynolds-averaged and wall-modelled large-eddy simulations of impinging jets with embedded azimuthal vortices. *European Journal of Mechanics-B/Fluids,* Volume 55, pp. 348-359.

Wigg, L., 1959. *The effect of scales on fine sprays produced by large airblast atomiizer ,* Pyestock: National gas turbine stablishment.

Wigg, L. D., 1964. An airblast atomizer for use with viscous fuels. *Journal of the Institute of Fuel,* 27(164), pp. 500-505.

Willauer, H. D., Mushrush, G. W. & Williams, F. W., 2006. Critical evalution of rotary atomizer. *Petroleum Science Technology,* Volume 24, pp. 1215-1232.

Wood, R., 1954. *Unpublished work at Thorton Shell Research Center.* s.l.:s.n.

Yoon, S. S. & Heister, S. D., 2003. Categorizing linear theories for atomizing round jets. *Atomization and Sprays,* Volume 13, pp. 499-516.

Zhou, X., Li, T. & Lai, Z., 2019 b. Similarity of split-injected fuel sprays for different size diesel engines. *International Journal of Engine Research.*

Zhou, X., li, T., Wei, Y. & Wang, N., 2019 a. Scaling liquid penetration in evaporating sprays for different size diesel engines. *International Journal of Engine Research.*

Zhou, Y. et al., 2010. Experimental investigation and model improvement on the atomization performance of single hole Y-jet nozzle with high liquid flowrate. *Powder Technology,* Volume 199, p. 248–255.